An Experimental Investigation of a Table-Top, Laser-Driven Extreme Ultraviolet Laser

by

James G. Goodberlet

B.S. Physics
Bates College, 1985

S.M. Electrical Engineering
Massachusetts Institute of Technology, 1990

SUBMITTED TO THE DEPARTMENT OF ELECTRICAL ENGINEERING AND COMPUTER SCIENCE
IN PARTIAL FULFILLMENT OF THE REQUIREMENTS FOR THE DEGREE OF

DOCTOR OF PHILOSOPHY IN ELECTRICAL ENGINEERING
AT THE
MASSACHUSETTS INSTITUTE OF TECHNOLOGY

FEBRUARY 1996

Signature of Author:.....
Department of Electrical Engineering and Computer Science
January 19, 1996

Certified by:.....
Peter L. Hagelstein
Associate Professor of Electrical Engineering
Thesis Supervisor

Accepted by:.....
Frederic R. Morgenthaler
Professor of Electrical Engineering
Chairman, Departmental Committee on Graduate Students

An Experimental Investigation of a Table-top, Laser-Driven Extreme Ultraviolet Laser

by

James G. Goodberlet

Submitted to the Department of Electrical Engineering and Computer Science
on January 19, 1996 in Partial Fulfillment of the Requirements for the
Degree of Doctor of Philosophy in Electrical Engineering

ABSTRACT

Extensive experiments have been carried out to demonstrate extreme ultraviolet amplification by stimulated emission at wavelengths below 40 nm in a laser-produced plasma. Although a gain-length product larger than 4 was expected, amplification has not been observed in the laser-produced plasmas. Several recombination lasing schemes, H-like, He-like, Li-like, and Na-like, and several collisional lasing schemes, Ne-like and Ni-like have been investigated. The pump-laser pulse lengths were varied from 20 ps to 200 ps and the pulse energy was varied from 800 mJ to 3 J in the experiments.

Details of the pump-laser system and the extreme ultraviolet spectrometers are given. Frequency and angle-averaged, amplified spontaneous emission is simulated numerically for a long slender rod. A constant-dose gain measurement technique is presented, and the minimum detectable gain for the apparatus is estimated. Results from ionization spectra show that 210 ps pulses more effectively ionize the laser-produced plasmas from slab targets. Spectra in the vicinity of the lasing line for several lasants are shown. Preliminary transverse-and-longitudinal pumping experiments have been conducted. In one of these experiments, a plasma conduit is created with a novel target geometry.

Thesis Supervisor: Peter L. Hagelstein
Title: Associate Professor of Electrical Engineering

Acknowledgements

Many contributed to this work. I thank Dr. P. Hagelstein, Professor L. Smullin and members of the x-ray laser group at MIT for valuable assistance. I am very grateful for the help of Santanu Basu, Sumanth Kaushik and Tim Savas. We had an enjoyable time in the lab. I thank Dr. J. Twichell and the ACC committee at Lincoln Laboratories for providing funding during the final years of this research project. I thank my thesis committee members, Professors S. Ezekiel and H. Smith, for agreeing to read this manuscript on short notice. Special thanks also goes to Professor H. Smith for providing financial and personal assistance during the last year of this work.

I certainly could not have completed this work without the support, guidance, patience, and concern of friends and family. I am looking forward to the next bike trip with "the guys" from Bates College, Pete, Steve, Ken, Paul and whoever else can come along. Many thanks go to Cara for all her help. Maybe now, we can finally see a movie. Well Dad, it's a long way from milking cows. Thanks Mom and Dad. Thank you all.

Contents

List of Tables

Chapter 1

Introduction

1.1 Research Objective

The ultimate goal of this research has been to demonstrate experimentally a table-top extreme ultraviolet (EUV) laser with a gain length product greater than 5 at a wavelength below 40 nm. Such a device might be useful for preliminary lithographic experiments, for material surface spectroscopy, or for further research in developing a compact sub 4 nm coherent source. The primary goal of this research has not been achieved. Recent experiments have not shown evidence of EUV amplification in several lasant plasmas, which were excited with the MIT table-top pump-laser system.

When experiments began with the MIT table-top EUV system in 1989, the research effort was novel in two respects. These experiments were the first attempts to demonstrate small scale EUV lasing with collisional lasants. Also, the experiments were the first to use multiple subnanosecond pump-laser pulses to excite the EUV laser. Small signal gain values of $\alpha \sim 10$ cm^{-1} were predicted for Ni-like lasants.

Initial experimental results with the MIT system showed evidence of amplification, $\alpha \sim 2.8$ cm^{-1}, in Ni-like Nb [1], and amplification, $\alpha \sim 3.7$ cm^{-1} in H-like B [2]. These initial results have motivated the research described in this thesis. Based on these positive results, we decided to devote our resources to demonstrating higher gain and gain-length products, rather than determining the discrepancy between predicted and the observed gain values. Numerous subsequent experiments have not reproduced the results of our earlier work, and recent experiments described in this thesis have indicated that one of the earlier results [2] is in error.

This thesis describes a complete set of experiments, from a redesign of the pump-laser system to a search for gain in several EUV lasants, which were carried out during the past two years.

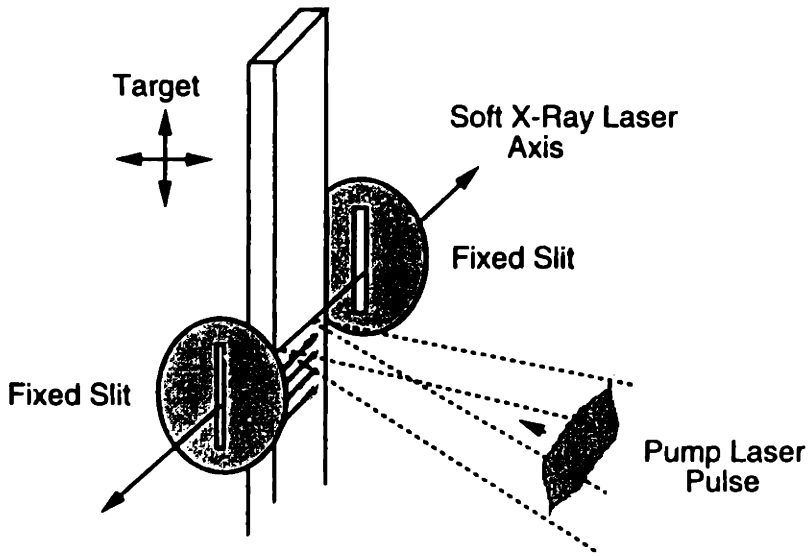

Figure ...: Laser-driven soft x-ray laser. Soft x-ray lasers are typically driven with a high power pump-laser, which is focused to a long thin line on the lasant target. The resulting line of plasma defines the soft x-ray laser axis. Slits are used to observe the gain region within the expanding plasma. The soft x-ray laser and detectors are housed in a vacuum chamber.

In these recent experiments, we have not detected a gain-length product larger than 1.6. Some possible explanations for the absence of EUV amplification are outlined in chapter 8. It is hoped that the information and results gathered here will assist in directing a future successful short wavelength laser experiment with the MIT table-top extreme ultraviolet system.

1.2 Synopsis of X-Ray Laser Research

The terms "x-ray laser" or "soft x-ray laser" have been applied to any device which exhibits amplified spontaneous emission below 50 nm. To date, the shortest wavelength x-ray laser operates at 3.6 nm [3]. Recently, a low power, high gain laser has been demonstrated at 46.9 nm [4]. By one definition, the x-ray spectral region is defined as wavelengths below 2 nm, the soft x-ray region is defined as wavelengths from 2 to 30 nm, and the extreme ultraviolet (EUV) spectral region is the range from 30 nm to 100 nm [5]. Many of the amplification experiments reported here have been in the EUV regime, while many diagnostic measurements have been made in the soft x-ray spectral region. These two terms and acronyms will be used frequently throughout this dissertation.

All demonstration of soft x-ray amplification to date have been in highly ionized plasmas contained in vacuum. Typically, a thin, long plasma (about 100 μm × 1-4 cm) is created and ionized by focusing a high energy, > 1 kJ, high power, > 1 TW, drive-laser beam onto a solid or thin film soft x-ray laser target in vacuum as shown in figure 1.1. The vacuum is necessary to allow the high power densities of the drive-laser beam, > 10^{12} W cm^{-2}, and to allow propagation of the soft x-ray laser beam without absorption. For highly ionized atoms, the lasing transition wavelengths are shifted into the soft x-ray regime. Under proper excitation conditions, a population inversion forms within the plasma, which results in soft x-ray amplification by stimulated emission.

Soft x-ray laser research is a multi-disciplinary field. On the theoretical side, an understanding of atomic physics, hydrodynamics, laser-plasma physics and laser physics is required. Sophisticated computer programs, such as LASNEX and XRASER [6] which have been used for the successful soft x-ray laser experiments at Lawrence Livermore National Laboratories, have been developed by theorists to simulate plasma creation, heating, expansion and ionization. These programs predict the presence and duration of soft x-ray gain, and also model propagation of amplified emission through the plasma. Even with considerable computational effort, theoretical accuracy has been difficult to achieve for some experiments as depicted in figure 1.2 [7]. Agreement between theory and experiment has improved markedly in the past few years with further refinement of the models and more experimental data to guide the theory.

On the experimental side, familiarity with high power drive-lasers, high power beam optics and beam propagation, high vacuum operation and EUV or soft x-ray spectrometers and detectors is required. Usually, soft x-ray experiments proceed slowly because of the low firing rate of the high power drive-lasers. For the first soft x-ray laser demonstration [8], the drive laser could be fired only at several shots per day. For the table-top experiments reported here, the drive-laser could be fired every thirty seconds. Because of its multifaceted nature, soft x-ray laser research is best conducted as a team effort.

Practical applications of soft x-ray lasers, which are driven by high power lasers, are presently limited, because of the system's low firing rate. These large systems typically have shot repetition rates varying from minutes to hours. Recently, there have been several novel approaches for creating an inversion with low power, table-top systems. Significant amplification has been demonstrated with these systems at wavelengths from 30 nm to 50 nm, and some table top

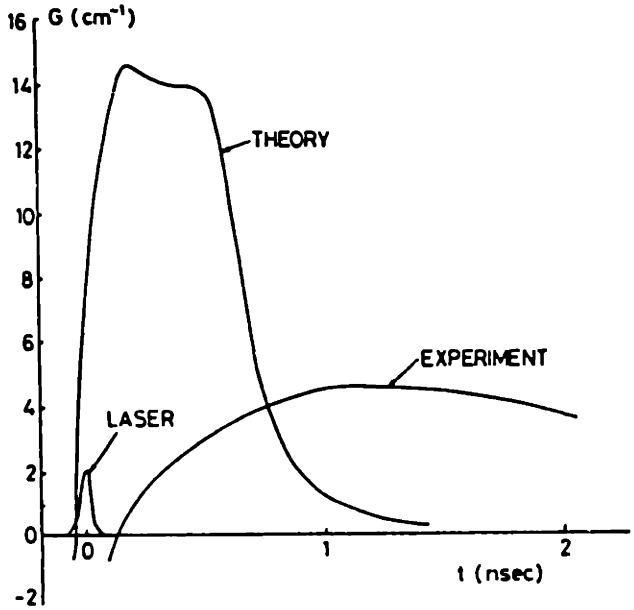

Figure 1.2: Early theoretical and experimental results. An experimental result and theoretical prediction for a recombination soft x-ray laser experiment shows poor agreement. Subsequent improvements in theory, and additional experimental results have significantly increased the agreement between theory and experiment. From reference [7]

systems can be operated at rates up to 10 Hz.

In addition to a high repetition rate, an efficient, high gain table-top system is necessary for EUV or soft x-ray applications. These applications might include probing of high density plasmas [9], analyzing material surfaces by electron spectroscopy for chemical analysis (ESCA) [10], or achromatic lithography [11]. The most attractive applications of soft x-ray lasers are imaging of live biological specimens or x-ray lithography. These two applications require wavelengths below 4 nm, and therefore are not feasible for present table-top soft x-ray lasers. Perhaps further experimentation with existing table-top soft x-ray lasers, will provide clues for developing a compact sub 4 nm source, which will be a valuable source for lithography and biological microscopy.

1.3 Overview of Thesis

This thesis is primarily a compilation of experiments with the MIT table-top EUV system. These experiments were conducted during several years time with the ultimate goal of demonstrating a high gain EUV amplifier. When useful, analytic models will be described and presented.

The experiments carried out have been extensive. The drive-laser system has been upgraded, operated in several configurations and operated at its maximum output capability. The EUV and soft x-ray spectrometers have been upgraded, and considerable care has been taken in performing spectrometer calibrations and gain measurements. Several lasants for several different lasing schemes have been investigated. The most recent experiments have shown no evidence of EUV amplification in our laser-driven plasmas.

In chapter 2, soft x-ray laser experimental research is summarized. Results from experiments, which have been conducted at laboratories around the world, are tabulated. The emergence and brief history of table-top soft x-ray laser research is traced. Research in this area began in the mid 80's, and has resulted in several efficient table-top soft x-ray laser systems. Successful table-top schemes will be described, which will provide a comparison for the MIT table-top EUV system.

Basics of EUV laser theory will be presented in chapter 3. Fundamentals of plasma heating by absorption of the pump-laser will be described and used to estimate the electron temperature, T_e. A simple three-level model will be used to estimate soft x-ray gain for recombination and collisional lasing schemes. Soft x-ray refraction and opacity, effects which reduce gain, will be described and their values estimated. Finally, effects of a population inversion on spectral data, recorded from each spectrometer, will be described.

A detailed description of the MIT table-top EUV system will be given in chapter 4. To improve the performance of the pump-laser, the method of chirped pulse amplification (CPA) [12] has been used. Details of this upgrade are presented. Assembly of and modifications to the two EUV spectrometers, the time-integrating flat-field spectrometer (TIFFS) and the streaked or imaging concave grating spectrometer (S/ICGS), will be described. Calibration procedures for the two spectrometers will be presented. The ICGS can also be used to align the plasma axis and to align multiple pump-laser beams on the EUV lasant target. These alignment procedures will be described. Chapter 4 provides system operating details, which will assist future research efforts.

A new gain measurement technique has been developed during this study. This technique will be described in chapter 5. All gain measurements, with the MIT table-top system, have been made by recording lasing transition intensity on film for several different plasma lengths. For early results [1,2], line intensity for each plasma length was recorded on separate photos.

Gain was estimated from the data after film saturation corrections were made, and with the assumption that film response was identical for each photo. For the new measurement technique, the imaging concave grating spectrometer is used to record intensities for all plasma lengths on a single photo. Additionally, the film is exposed with constant dose so that film saturation corrections are unnecessary. This new gain measurement technique is best suited for low gain systems, and can readily detect gain-length products as low as 1.6.

In chapter 6, results from several laser-driven plasma experiments are presented. A series of plasma heating experiments have been conducted for several different operating configurations. The experiments have been designed to determine the best operating configuration of the pump-laser for subsequent gain studies. It has been found that transverse pumping of the lasant target with multiple, high energy long pulses is best suited for our studies. From observations of plasma emission, the time-integrated spectra appears hotter when 210 ps pulses are used to create the plasma, rather than 23 ps pulses. In other experiments [13], gain in recombination soft x-ray lasers has been increased by mounting a steel blade near the plasma. Effects of the steel blade on plasma formation have been studied in several "blade" experiments. The blade has been found to confine and cool the plasma. When properly designed, the blade creates a plasma conduit, which is ideal for end-pumped plasmas. Results from end-pumping experiments, with such a blade, are also presented in chapter 6.

Results from gain studies are presented in chapter 7. For most of these experiments, the pump-laser has been configured to give the hottest plasma. Several "best candidate" lasants have been tested for several recombination and collisional lasing schemes. Spectroscopic data from ionization and gain measurements is presented. For all recombination lasing schemes tried, the lasing transition has been identified. The lasing transition has been possibly identified for only two collisional lasing schemes. There has been no indication of a gain-length product greater than 1.6 for any of the recombination or collisional lasants surveyed in this study.

A summary is given in chapter 8, along with suggestions for future experiments with the MIT table-top EUV system. With the exception of two recent results [14,15], the pump-laser used in this study is at least a factor of 10 lower in power, or a factor of three lower in energy, than drive-lasers used for successful soft x-ray amplification demonstrations at other laboratories. It is unlikely that high gain will be demonstrated with the current system, unless a novel pumping scheme is devised. One novel scheme might be an electric discharge assisted, laser-pumped

plasma. Without a novel pumping arrangement, it is recommended that the output energy of the pump-laser be increased four fold, or a second high energy picosecond pulse laser be added before further experiments are pursued.

1.4 Contributions

Contributions from this research are listed below.

- Upgrade of the pump-laser system to deliver short pulses, 23 ps, or long pulses, 210 ps. Presented at the 1994 Lasers and Electro-Optics Society Annual Meeting.
- Upgrade of both EUV spectrometers. Presented at the 1995 Conference on Soft X-Ray Lasers and Applications sponsored by the International Society for Optical Engineering.
- Survey of recombination and collisional EUV lasants. Reported in this document.
- Investigation of long and short pulse pumped plasmas. Presented at the 1995 Conference on Soft X-Ray Lasers and Applications sponsored by the International Society for Optical Engineering.
- Preliminary investigation of longitudinally pumped plasmas using novel target designs. Presented at the 1994 International Conference on Lasers sponsored by the Society for Optical and Quantum Electronics.
- Development of a reliable, in-house data processing system. Presented at the 1995 Conference on Soft X-Ray Lasers and Applications sponsored by the International Society for Optical Engineering.
- Analysis of angle-averaged gain measurements. Reported in this document.
- Spectroscopic identification of the Li-like Mg 5g-4f and Na-like Ca 5g-4f candidate lasing lines.
- Design and assembly of an SHG and electric field autocorrelator to determine pump-laser pulse lengths.
- A constant-dose gain measurement method for low gain EUV lasers. Paper in progress.

Chapter 2

Review of Soft X-Ray Laser Experiments

2.1 Introduction

Two soft x-ray lasing schemes were proposed in the 1960's and 70's by Soviet scientists [16,17]. These schemes have come to be known as *recombination* and *collisional* lasing schemes. Nearly all soft x-ray laser research has concerned these two schemes. Before reviewing the soft x-ray laser experiments, the basic concepts of recombination and collisional lasing in hot plasmas will be presented.

Soft x-ray laser research has taken a somewhat circuitous path. In one of the first soft x-ray laser demonstrations, a gain-length product of 4.5 was reported for a recombining H-like C laser-produced plasma [18]. A pre-pulse was used in this experiment to preform the plasma and increase energy coupling to the plasma. Interestingly, the pump-laser pulse energy used in this experiment was about 8 J.

In the 1980's, most soft x-ray laser experiments were conducted at government facilities, where high-power, high-energy pump-lasers were available. Typically, these high-power drive-lasers produced optical pulses with energies between 100 and 6000 J. These high-power lasers were ideal for producing the hot dense soft x-ray laser plasmas. Numerous demonstrations of soft x-ray amplifiers resulted. Details and results from many of these experiments will be summarized and tabulated in this chapter.

Although early soft x-ray laser experiments have benefited from the large laser facilities, ultimately the move of research to these facilities has proved to be costly to the soft x-ray laser community. The large facilities are expensive to maintain with multimillion dollar annual

budgets. Some of these resources may have funded several university programs. Because of the large laser-drivers, the demonstrated soft x-ray amplifiers have very low firing rates. Typical cooling periods for the drive-lasers range from many minutes to hours. These soft x-ray lasers are impractical short wavelength sources.

In the 1990's there have been several efforts, at the university level, to develop compact, or table-top, soft x-ray lasers. This, however, is where the field began in the late 70's. Some of these table-top systems are scaled versions of the large, high power systems, whereas others are highly innovative approaches. Several successful table-top systems will be described in this chapter.

2.2 Recombination and Collisional Lasing Schemes

2.2.1 Short Wavelength Lasing in Hot Plasmas

Most demonstrations of soft x-ray or EUV gain, for both recombination and collisional lasing schemes, have been carried out in long, thin highly ionized plasmas. High degrees of atomic ionization give larger energy differences between the lasing transitions. For example, the 3d-2p transition in hydrogen (H) is a recombination lasing transition. For H, the transition energy, ΔE, is 1.89 eV, which can be converted to wavelength, λ, with the following relation

$$\lambda = \frac{1239.85}{\Delta E} \tag{2.1}$$

where ΔE is in electron volts and the units of λ are nanometers. The corresponding wavelength for H is 656 nm. For H-like C, carbon with five electrons removed, the corresponding 3d-2p transition wavelength is 18.2 nm. The ionization potential of H-like C is 490 eV, an energy achieved in hot plasmas.

Normally, the hot plasmas are created in long, thin columns as shown in figure 2.1. For most experiments, the plasma is created by a high energy laser pulse which is tightly focused to a line on the lasant target, as was shown in figure 1.1. The focused power on the target is typically 10^{12} – 10^{14} W cm^2, and target lengths vary from 0.5 cm to 3 cm in length. The high energy drive-laser pulse ablates mass from the target and delivers energy to the plasma through resonance absorption and inverse Bremsstrahlung absorption [19]. Plasma temperatures typically range from a few hundred eV, for long wavelength amplifiers, to over 1 keV for short wavelength schemes [20]. As the plasma heats, the lasant atoms are ionized to their desired

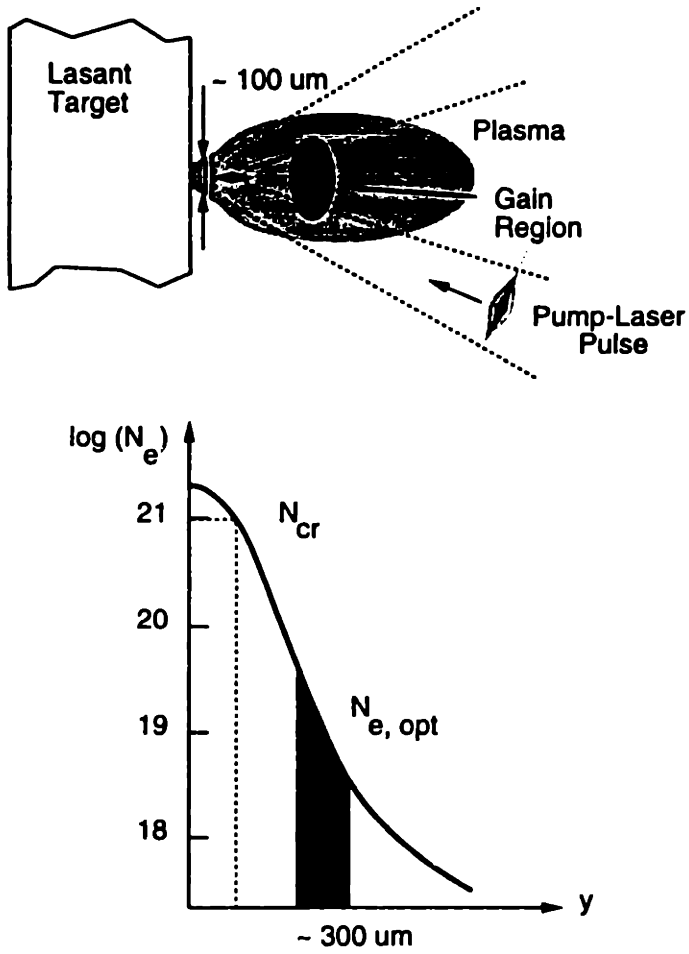

Figure 2.1: Plasma column. All demonstrations of soft x-ray or EUV amplification have been in long thin hot plasmas. Only a small region of the plasma, about 100 μm in diameter, has conditions appropriate for an inversion for a short time, about 1 ns. The plasma expands into the vacuum and cools. A suggested electron density profile is sketched.

stage. Once the proper ionization stage is reached, lasing action may occur.

The length of the plasma defines the length of the gain region. Lengthening the plasma will increase the gain-length product, provided an inversion can be maintained uniformly along the plasma column. The transverse dimension of the plasma is kept small, < 200 μm, in order to achieve high pump-laser power densities, and to minimize reabsorption of the lower laser level resonance emission, noted in figure 2.2. Reabsorption of the lower level emission repopulates the lower laser level, which reduces the inversion density. Consequently, long hot thin plasmas are a precondition to recombination or collisional lasing at soft x-ray wavelengths.

For both recombination and collisional lasing schemes, uniformity in electron density is required along the plasma column. Inhomogeneities in electron density can create regions of

absorption along the EUV laser axis. The amplified beam would then be absorbed as it propagates down the plasma column. Inhomogeneities can also lead to beam refraction, a subject which will be discussed in chapter 3.

The particular lasing scheme, recombination or collisional, is determined by the lasant chosen and the ionization stage achieved. Both schemes may occur for one lasant element at different ionization stages. As an example, Na-like Ca may exhibit recombination lasing on the 5g-4f transition at 40.4 nm, and Ne-like Ca may exhibit collisional lasing on the 3p-3s transition at 38.3 nm. However, the ionization potentials for Na-like Ca and Ne-like Ca are 211 eV and 374 eV, respectively [21].

2.2.2 Recombination Lasing

For recombination lasing, the lasing atom is initially prepared in a fully stripped, closed shell electronic configuration. Possible recombination schemes include H-like atoms (completely stripped), Li-like atoms (1s shell full) and Na-like atoms (1s2s2p shells full). Energy levels for the H-like C scheme are illustrated in figure 2.2. For this scheme, the lasing transition is 3d-2p and the ground state is 1s. As the plasma expands and rapidly cools, electron capture into outer levels occurs, as shown by the broad arrow in the diagram. Rapid cooling causes electrons to cascade to lower levels, which can result in a population inversion between the 3d-2p levels. High gains are predicted when the plasma cools to less than $\frac{1}{10}$th of the ionization potential [22,23].

Cooling of the hot plasma can be enhanced in several ways. Typically, a small initial plasma volume is expanded into vacuum [22,23]. Another approach is to use strong magnetic fields to increase radiative cooling of hot electrons [24,25,26]. Plasma expansion against a cold metal heat sink also enhances cooling and recombination rates [13,27]. Increasing the recombination rate results in a higher inversion density.

A population inversion for short wavelength recombination lasers is predicted to occur between the two levels just above the ground state. This is because the ground state resonance transition, 2p-1s, has a high transition rate. Therefore, the lower laser level will deplete rapidly. For other recombination sequences, the lasing levels shift up. For Li-like atoms, the ground state is 2p and the lasing transition is 4f-3d.

There are several characteristics of recombination lasing which differ from collisional lasing. Recombination lasing is a transient lasing process. As the ions cool, and capture one electron,

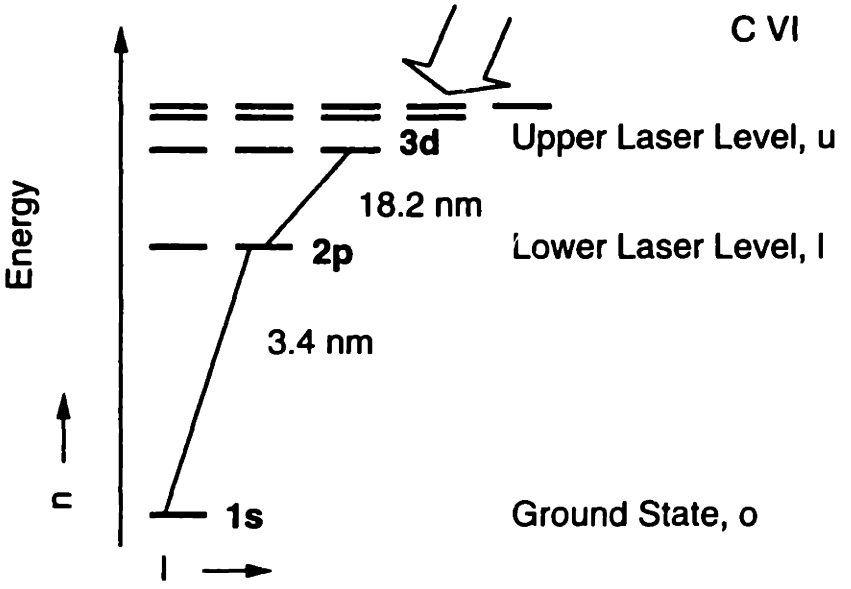

Figure 2.2: Recombination lasing. Energy levels for H-like C are depicted. For recombination lasing, electrons are captured into outer levels, and cascade to lower levels as the plasma rapidly cools. A population inversion can occur for the 3d-2p transition as the electrons cascade downward. The lower laser level is rapidly dumped to the ground sate, 1s. Reabsorption of the 2p-1s resonance emission must be minimized to prevent repopulation of the 2p level, which will reduce the inversion density.

the ionization stage is reduced and the ion is no longer available for gain. Recombination lasing is usually demonstrated with low atomic number, Z, elements, Z < 30, and the lasing wavelengths scale rapidly with Z. For the H-like sequence, the lasing wavelength and ionization potential scale as Z^{-2} and Z^2, respectively. The scaling increases with ion sequence. For the Li-like and Na-like sequences, the wavelength and ionization potential scale roughly as $Z^{-2.5}$, $Z^{2.3}$ (Li-like) and $Z^{-3.5}$, $Z^{3.8}$ (Na-like) [28,21] in terms of the atomic number only.

For recombination schemes, substantial emission from the lasing transition is always observed, even in the absence of gain, provided the atom has been adequately ionized. The "gain line" is observed in recombination schemes because the lasing transition is a principal decay route for the cascading electrons. The emission spectra for low Z recombination lasants is less complicated than that for mid Z elements, and the spectral lines are easily identified. Experimental observation of the gain line indicates that the proper ionization stage has been achieved, but does not alone determine the existence of an inversion.

2.2.3 Collisional Lasing

For collisional lasing schemes, the lasant atom is also stripped to a closed shell configuration. Typically, mid to high Z elements are used for Ne-like and Ni-like ion sequences. A simplified energy level diagram for Ne-like Ca is shown in figure 2.3. In collisional lasing, the upper laser level, shown as 3p for the Ne-like diagram, is populated by collisional excitation of electrons from the ground state, $2p^6$, as indicated by the broad arrow in the diagram. Since the excitation is a monopole transition, the upper laser level, 3p, cannot radiatively decay to the ground state, but may decay to the nearby 3s level, which in turn depletes rapidly to the ground state. For the Ni-like ion sequence, the lasing transition is 4d-4p. An adequate density of electrons, N_e, with sufficient temperature, T_e, is required in the plasma in order to sufficiently populate the upper laser level. For Ne-like Ca, N_e and T_e on the order of 5×10^{18} cm^{-3} and 150 eV are required for a population inversion on the 3p-3s transition. The values for N_e and T_e required for collisional lasing will be discussed in chapter 3.

Unlike recombination schemes, collisional lasing can be continuous provided that the appropriate electron temperature and density can be maintained in the plasma. Electrons can be continuously pumped to the upper laser level through collisional excitation. In practice, these amplifiers have only been demonstrated in pulsed mode because it is not yet possible to sustain

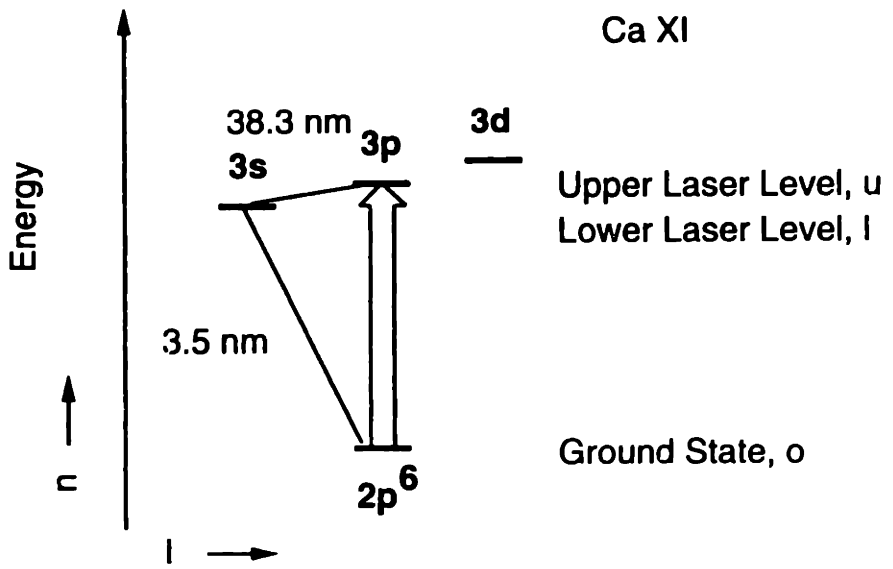

Figure 2.3: Collisional lasing. A simplified energy level diagram for Ne-like Ca is shown. For this lasing scheme, electrons are collisionally excited from the ground state, $2p^6$, to the upper laser level, 3p. With the correct electron density and temperature in the plasma, a population inversion occurs between the 3p and 3s lasing levels.

the high drive-laser power and energy densities required for excitation of the plasma.

Lasing wavelength and excitation energy scale less favorably, with respect to atomic number only, for collisional schemes. For the Ne-like sequences, wavelength and excitation energy scale very crudely as $Z^{-1.6}$ and $Z^{2.7}$ [21,29]. For Ni-like lasants, wavelength and excitation energy scale roughly as $Z^{-2.5}$ and $Z^{3.3}$ [30,1]. These scaling laws are empirical. Compared to the recombination lasing schemes, the collisional lasers require more pumping power as the lasing wavelength is lowered.

In collisional lasing schemes, the gain line is not easily observed unless the transition has an appreciable inversion. The lasing transition in collisional schemes is not a principal decay route, and the weighted oscillator strength, $g_u f_{ul}$, is generally weaker than that for recombination schemes: $g_u f_{ul} \approx 0.16$ for Ne-like 3p-3s and $g_u f_{ul} \approx 4.17$ for H-like 3d-2p transitions [31,32]. Also, the emission spectra of the mid and high Z lasants, which are used for Ne-like and Ni-like schemes, are complicated and have a large electron continuum background. These factors make laser line identification difficult for collisional lasing schemes.

Table 2.1: Recombination Gain Demonstrations

Year	α [cm^{-1}]	λ [nm]	l_p x w_p [cm x cm]	E [J]	τ [ns]	Scheme	Ref.
1976	10	13.0	.02 x .020	13	0.20	He-like Al	13
1981	6.0	18.2	.15 x .003	11	0.25	H-like C	33
1983	4.0	18.2	1.0 x .030	750	75	H-like C	25
1985	6.5	18.2	1.0 x .030	300	75	H-like C	26
1987	4.1	18.2	.7 x .003	25	0.07	H-like C	7
	2.5	10.6	1.0 x .010	200	3	Li-like Al	34
1989	< 0	10.6	2.0 x .030	1500	0.10	Li-like Al	35
	8.0	18.2	.3 x .010	25	3	H-like C	27
1990	1.9	10.4	1.0 x .010	120	0.30	Na-like Cu	36
	4.4	8.1	.5 x .002	375	0.07	H-like C	37
	2.0	11.1	2.0 x .010	46	0.90	Na-like Cu	38
1992	2.3	6.9	1.6 x .010	58	0.45	Na-like Cu	39
1993	3.7	15.5	.7 x .010	30	0.50	Li-like Al	40
1994	5.9	5.4	.6 x .005	32	0.020	H-like Na	41
	5.9	8.1	.6 x .005	32	0.020	H-like F	41

2.3 Demonstrations of Soft X-ray Amplification

There have been many demonstrations of soft x-ray and EUV amplification in laser-produced plasmas since the 80's. The majority of these experiments have been carried out with high power, high energy drive-lasers. Most of these results are listed in table 2.1 for recombination lasants, and table 2.2 for collisional lasants. Several experimental values are listed on the tables: small signal gain, α, lasing wavelength, λ_x, plasma length and width, $l_p \times w_p$, pump-laser energy, E, and pump-laser pulse length, τ. In some experiments, multiple pulses or pump-laser beams have been used. The energy value listed is total optical energy incident on the lasant target.

The early recombination gain measurements were done with low pumping energy and small plasmas [13,33]. In these experiments, the presence of an inversion was determined by line ratio measurements, and soft x-ray gain was not measured directly. These gain estimates are more susceptible to error, since spectrometer and detector wavelength responses must be known precisely, and since the ion density must also be determined accurately.

There have been only two recombination soft x-ray laser experiments which have demonstrated a gain-length product, αL, greater than 6 [27,42]. It is presently unclear why recombination lasers cannot be driven into saturation, $\alpha L > 12$. One possible explanation is that plasma instability destroys the uniformity of the lasing region [59]. The recent demonstration using ultrashort pump-laser pulses appears to be the most likely prospect for exceeding the current gain-length limit [42].

The experimental parameters vary considerably for the recombination gain demonstrations as shown in table 2.1. For these experiments, the pumping energies vary from tens of joules to kilojoules. The pump-laser pulse duration varies from picoseconds to many nanoseconds. These wide variations are not recorded for the collisional schemes of table 2.2. The collisional gain measurements have been performed at higher pumping energies and longer pump-laser pulse lengths. The increased energy and pulse length are attributed to the high electron temperature and density required for collisionally induced inversions. Most collisional gain demonstrations require hundreds of joules to kilojoules of pump-laser energy.

For the collisional lasing schemes, both the Ne-like and Ni-like ion sequences have performed well. Saturated amplification has been observed with Ne-like soft x-ray lasers at several laboratories [51,52]. For the recombination schemes, only the H-like sequence has performed well, and has been investigated at several labs. Heavier ions for other recombination sequences may cool too slowly, so that large inversion densities cannot be achieved with other sequences.

The recombination and collisional lasing demonstrations are summarized in the graphs of figure 2.4 and figure 2.5. The recombination data are plotted as squares and the collisional data is plotted as rectangles. In figure 2.4, the reported gain, α, has been divided by the pump-laser peak intensity, I_p, used in the experiment. This ratio represents a figure of merit for the lasing scheme: a larger ratio is desirable. For example, a ratio of $\alpha I_p = 1$ cm TW^{-1} implies that 10^{13} W cm^{-2} is required for a gain of 10 cm^{-1}. If the pump-laser pulse duration is 100 ps, and the pump-laser beam is focused to a 100μm x 1 cm line, then roughly 10 J of pump-laser energy would be required to achieve 10^{13} W cm^{-2}. A similar figure of merit is plotted in figure 2.5, in which the reported gain has been normalized to the pump-laser fluence, F_p.

The graphs of figures 2.4 and 2.5 show that the normalized gain values vary within a factor of 100 for a wavelength variation by a factor of 10. This result is somewhat surprising considering the large variations in experimental conditions for the recombination gain measurements. For

Table 2.2: Collisional Gain Demonstrations

Year	α [cm^{-1}]	λ [nm]	l_p x w_p [cm x cm]	E [J]	τ [ns]	Scheme	Ref.
1985	4.0	20.6	2.0 x .010	800	0.50	Ne-like Se	8
1987	5.0	15.5	2.0 x .010	1600	0.50	Ne-like Y	20
	4.1	13.1	1.7 x .010	4500	0.50	Ne-like Mo	20
	2.0	22.1	1.6 x .020	380	2.0	Ne-like Cu	43
	4.1	23.2	1.6 x .020	380	2.0	Ne-like Ge	43
	1.1	7.1	3.5 x .020	4900	1.0	Ni-like Eu	44
1988	1.2	5.0	1.7 x .013	3100	1.0	Ni-like Yb	30
1990	4.2	23.2	1.2 x .005	150	2.0	Ne-like Ge	45
	4.3	9.9	1.2 x .013	3900	0.50	Ne-like Ag	46
	2.3	4.5	2.0 x .012	5500	0.50	Ni-like Ta	47
	2.6	4.3	3.0 x .012	5500	0.50	Ni-like W	47
1992	2.9	23.2	.6 x .013	140	1.0	Ne-like Ge	48
	3.0	15.5	1.2 x .010	940	0.65	Ne-like Y	49
	1.9	17.4	3.4 x .012	4080	0.50	Ne-like Rb	50
1993	5.3	15.5	3.8 x .010	2850	0.50	Ne-like Y	51
1994	4.9	21.2	2.0 x .015	450	0.60	Ne-like Zn	52
1995	4.1	19.6	3.2 x .010	640	0.10	Ne-like Ge	53
	>3	18.2	3.2 x .010	960	0.10	Ne-like Se	53
	>3	12.0	2.5 x .010	500	0.40	Ni-like Sn	54
	4.2	21.2	2.0 x .015	390	0.60	Ne-like Zn	55
	>3	19.6	4.0 x .010	250	1.0	Ne-like Ge	56
	3.1	8.0	2.5 x .010	250	1.0	Ni-like Nd	56
	2.6	7.3	2.5 x .010	250	1.0	Ni-like Sm	56
	2.8	6.9	2.5 x .010	250	1.0	Ni-like Gd	56
	4.0	6.7	2.5 x .010	250	1.0	Ni-like Tb	56
	1.7	46.9	2.7 x .015	450	0.45	Ne-like Ar	57
	>2	10.0	2.7 x .015	450	0.45	Ni-like Xe	57
	3.7	19.6	2.5 x .015	450	0.45	Ne-like Ge	58
	4.3	20.4	2.5 x .015	450	0.45	Ne-like Ga	58
	4.5	21.1	2.5 x .015	450	0.45	Ne-like Zn	58
	4.3	22.1	2.5 x .015	450	0.45	Ne-like Cu	58
	4.3	23.1	2.5 x .015	450	0.45	Ne-like Ni	58
	4.1	25.5	2.5 x .015	450	0.45	Ne-like Fe	58
	4.3	26.9	2.5 x .015	450	0.45	Ne-like Mn	58
	3.9	28.5	2.5 x .015	450	0.45	Ne-like Cr	58
	4.4	30.4	2.5 x .015	450	0.45	Ne-like V	58
	3.0	32.6	2.5 x .015	450	0.45	Ne-like Ti	58
	3.8	35.2	2.5 x .015	450	0.45	Ne-like Sc	58
	3.8	38.3	2.5 x .015	450	0.45	Ne-like Ca	58
	3.4	42.1	2.5 x .015	450	0.45	Ne-like K	58
	2.5	52.9	2.5 x .015	450	0.45	Ne-like Cl	58

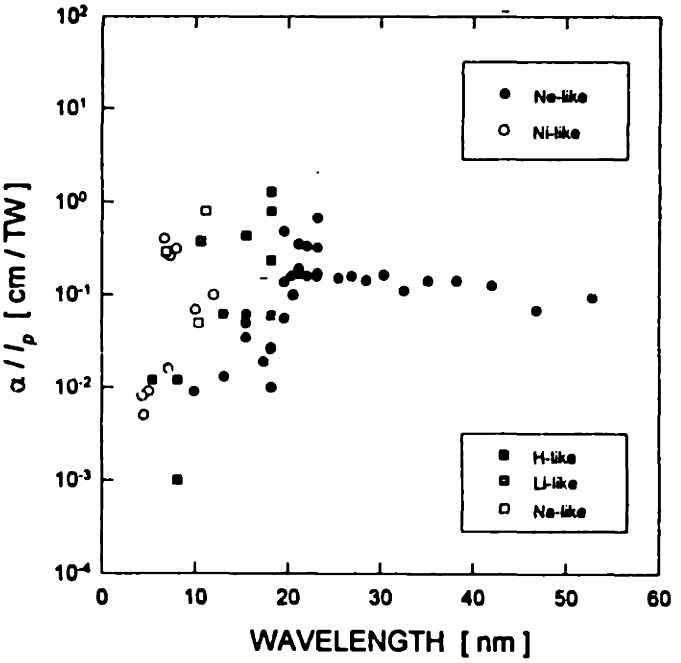

Figure 2.4: Intensity figure of merit. The reported gain values of tables 2.1 and 2.2 have been normalized to the peak pump-laser intensity incident on the lasing plasma.

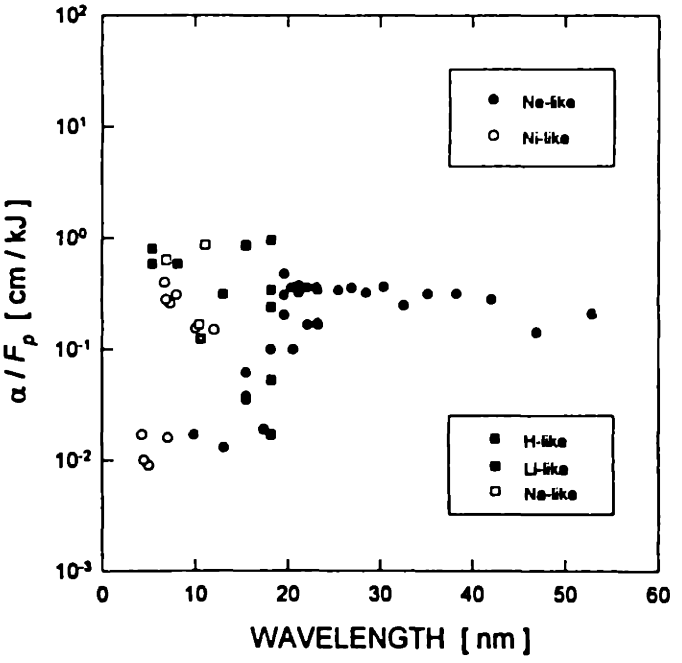

Figure 2.5: Fluence figure of merit. The gain values of tables 2.1 and 2.2 have been normalized to the pump-laser fluence incident on the lasing plasma.

reported table-top gain measurements, the normalized gain values vary significantly more than shown in figures 2.4 and 2.5.

2.4 Development of Table-Top Extreme Ultraviolet Lasers

Development of compact soft x-ray and EUV lasers began in the late 1980's. Several table-top EUV lasing schemes were proposed during this time, and the most successful of these schemes will be described in this section.

In the late 1980's, there were two efforts to "scale down" the large soft x-ray systems [27,60]. It was proposed that shorter pump-laser pulse lengths, multiple pulses, and a narrower line focus would result in peak power densities similar to the large systems, but with pump-laser pulse energies of about 10 J. Further, by using higher ionization sequences with lower Z atoms within the sequence, required plasma temperatures would be lowered. The MIT table-top system was the first attempt at a "scaled down" collisionally pumped EUV laser system.

To understand how plasma temperature is reduced as ion sequence is increased, consider the H-like and Li-like recombination sequences. For H-like ions, the lasing transition is 3d-2p, and for Li-like it is 4f-3d. For a comparable lasing wavelength from each scheme, an approximate relationship between the lasant atomic numbers, Z, can be written as

$$Z_H^2 C_H \approx (Z_{Li} - 2)^2 C_{Li} \tag{2.2}$$

where $C_H, C_{Li} = (n_l^{-2} - n_u^{-2})$ are lasing transition constants for the ion sequences. Equation 2.2 can be solved for Z_{Li}.

$$Z_{Li} \approx 2 + Z_H \sqrt{\frac{C_H}{C_{Li}}} \tag{2.3}$$

Thus, lasing at about 18 nm can be achieved with H-like C (18.2 nm) [28] or Li-like Mg (18.7 nm) [61]. However, the ionization potential is reduced 25 %, by changing to Li-like Mg: 490 eV for H-like C compared to 367 eV for Li-like Mg [28].

Other innovative proposals for table-top lasers in the late 1980's and early 1990's, have recently resulted in high gain demonstrations at EUV wavelengths. These novel systems have been titled Auger pumped, capillary discharge pumped, optical-field-induced ionized and transiently pumped table-top lasers. Each of these amplifiers have achieved near saturated gain.

In Auger pumped EUV lasers, the lasant atom is photo-ionized and undergoes Auger decay. Auger decay can occur to several final states, and for the Auger pumped laser the decay to the

upper laser level is more rapid than decay to the lower laser level. Consequently, an inversion builds up and stimulated amplification occurs. Because of the low ionization stages required for this scheme, pump-laser power is significantly reduced. UV Auger pumped lasers were proposed and demonstrated by two groups [62,63]. One of these experiments resulted in saturated amplification, $\alpha L \sim 12$, at 109 nm [63].

One of the more innovative proposals for soft x-ray laser schemes has recently resulted in a demonstration of near saturated gain at 46.9 nm [64,65]. In this scheme, a short pulse of high current is discharged through a capillary tube, which contains the lasant medium. The lasant may be gas, contained in the tube, or solid, coated on the tube's inner wall. The high current, $\sim$ 40 kA, is used to heat and compress the plasma so that the desired ionization stage and ion density is obtained. The short pulse, $\sim$ 20 ns, is necessary to limit the amount of mass ablated from the capillary walls. With long pulses, the plasma density increases and only low electron temperatures can be achieved. The capillary discharge scheme differs from all other soft x-ray lasing schemes in that a high power pump-laser is not used. Instead, a large capacitor is used to generate the high current discharge. The apparatus for the capillary discharge is shown in figure 2.6. Since a pump-laser system is not used, the capillary discharge method is the most efficient EUV lasing system. This method has been used with both recombination [67] and collisional [65] lasants. Near saturated gain has only been demonstrated with collisional lasing for the capillary discharge system.

Another innovative soft x-ray lasing system utilizes optical-field-induced ionization (OFI) to excite the plasma [68]. In this scheme, an ultrashort drive-laser pulse is used to achieve peak pumping intensities greater than 10^{15} W cm^{-2}. At such high intensities, the electric field distorts the atomic potential so strongly that the bound electrons can rapidly tunnel out of the potential well. The ultrashort pump-laser pulse and rapid ionization associated with OFI allow the creation of an inversion at very low ion temperatures. A low ion temperature is desirable, since it reduces the Doppler broadened lasing transition linewidth, an effect which increases gain. Both collisionally and recombination pumped OFI EUV lasers have recently been demonstrated [69,70].

Figure 2.7 shows the predicted pump-laser intensities required for an ionization rate of 10^{12} s^{-1} as a function of the ionization potential [68]. Candidate H-like and Li-like recombination lasants, and lasing wavelengths, are shown in the figure. The first demonstration of

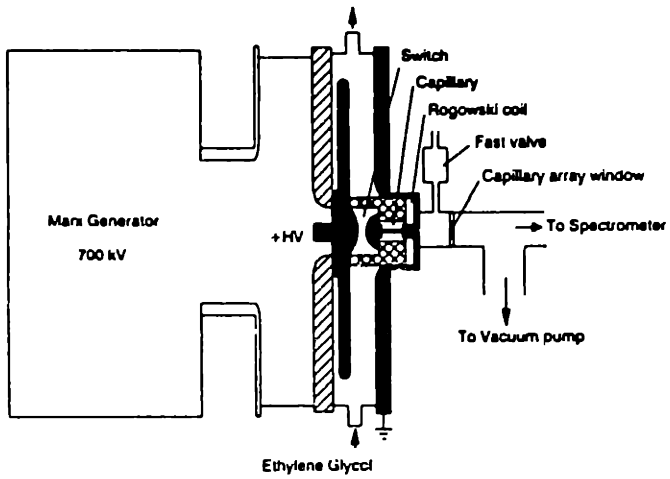

Figure 2.6: Capillary discharge system. An interesting alternative EUV lasing system is the capillary discharge pumped laser. The plasma is excited with a 40 kA, 20 ns current discharge through the capillary. This system recently achieved near saturated gain at 46.9 nm. From reference [66].

OFI lasing used lithium as the lasant [70]. The figure also shows the resulting electron energy, termed quiver energy, after ionization.

Near saturated amplification has been demonstrated with a collisionally pumped OFI EUV laser at 41.8 nm in Pd-like Xe [69]. For this experiment, the peak pumping intensity was 3×10^{16} W cm^{-2}, the pump-laser pulse length was 40 fs and the pulse energy was only 70 mJ. Because of the low energy the pump-laser could be operated at 10 Hz. Although the wavelength was long, this experiment represented a significant advancement for table-top soft x-ray lasers.

Another table-top system which recently yielded a high gain-length product, $\alpha L \sim 9.5$, is a transiently pumped EUV laser [71]. This scheme is most similar to the table-top scheme used at MIT, and is somewhat similar to the OFI schemes. In a transiently pumped EUV laser, a short pulse, 1 ps, is used to rapidly excite a pre-ionized plasma. The rapid excitation populates the upper laser level before a significant population can accumulate in the lower laser level. A long pulse, 1 ns, is used to preform and pre-ionize the plasma. After a short delay, about 2 ns, the short pulse further excites the plasma. A transiently pumped EUV laser was demonstrated with collisionally pumped Ne-like Ti at 32.6 nm [71]. For this experiment, the long pulse energy was

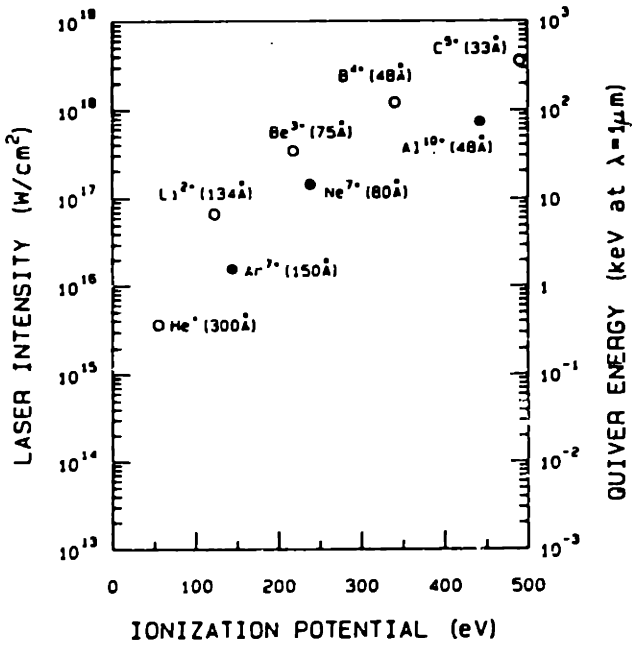

Figure 2.7: OFI pump-laser intensities. Pump-laser intensities required for an ionization rate of 10^{12} s^{-1} at different ionization potentials is shown. The electron energy after ionization is shown on the right axis. From reference [68].

about 5 J and the short pulse energy was about 3 J. Peak pump-laser intensity in the plasma was 2×10^{15} W cm^{-2}.

Sample data from the transiently pumped, Ne-like Ti experiment is shown in figure 2.8. The figure shows the intensity of the lasing line for three plasma lengths. Highly nonlinear growth of the line intensity is observed with increasing plasma length. An analysis of the data determines the small signal gain coefficient to be about $\alpha \approx 19$ cm^{-1}. It is interesting to note that the small signal gain, pump-laser intensity, and pump-laser pulse energy were all predicted, to within a factor of two, in the original proposal by Zherikhin, et. al. [17]

Performances of several table-top EUV amplifiers are summarized in table 2.3 and figures 2.9 and 2.10. These graphs are to be compared with those of figures 2.4 and 2.5. Experimental details are listed in table 2.3. To date, the "scaled down" recombination table-top lasers have received the most attention. Unless the problems, which limit generation of high gain-length products, are identified and solved, table-top recombination lasing may fall from favor as a viable EUV lasing method. The capillary discharge scheme is compact and considered a table-top system, despite its apparently large energy requirement, about 1 kJ. This energy is electrical and cannot be compared directly with the other optical pulse energies.

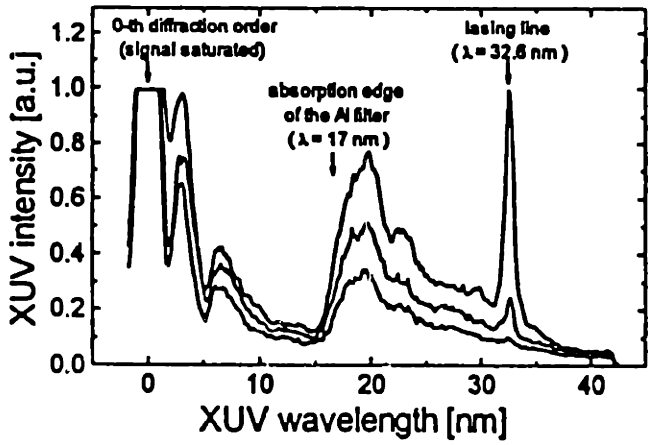

Figure 2.8: Transiently pumped Ne-like Ti EUV laser. The spectral data clearly shows nonlinear growth of the lasing line at 32.6 nm as the plasma length is increased. The three spectral traces correspond to plasma lengths of 2, 3 and 5 mm, from bottom to top. Note the poor resolution of the spectrometer. From reference [71].

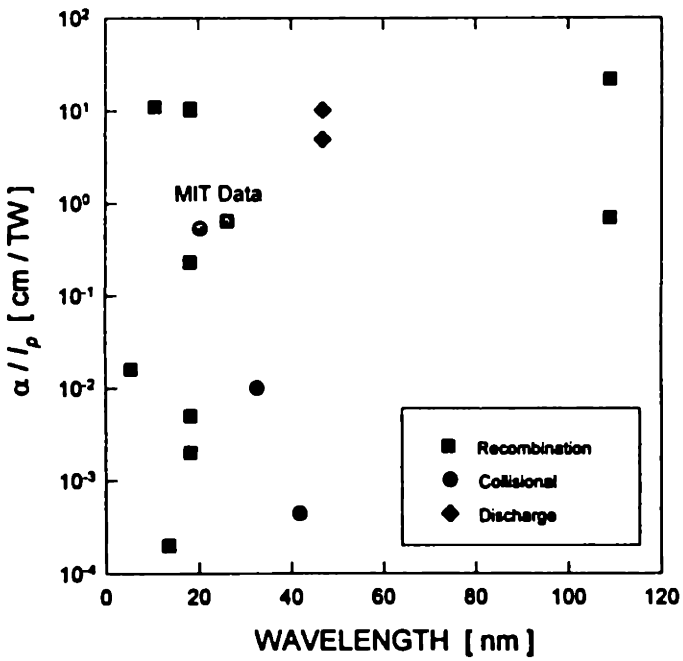

Figure 2.9: Intensity figure of merit. Table-top EUV gain values given in table 2.3 have been normalized to the peak pumping intensity in the plasma.

Table 2.3: Table-top EUV Gain Demonstrations

Year	α [cm^{-1}]	λ [nm]	l_p x w_p [cm x cm]	E [J]	τ [ns]	Scheme	Ref.
Auger							
1986	0.8	109	9 x .005	55	1	Xe III	62
1987	4.4	109	9 x .020	4	0.30	Xe III	63
Recombination / Collisional							
1981	18.0	18.2	.18 x .004	10	0.18	H-like C	18
1990	4.5	18.2	.4 x .010	6	3	H-like C	72
	8.0	5.4	.4 x .003	15	0.020	H-like Na	73
1992	4.1	18.2	.5 x .001	5	0.012	H-like C	74
1993	2.7	20.4	.8 x .002	2	0.060	Ni-like Nb	1
1994	7.1	18.2	.6 x .005	4	2	H-like C	14
1995	3.7	26.2	.8 x .004	1	0.060	H-like B	2
	12.5	18.2	.5 x .002	12	0.002	H-like C	42
	4.0	10.6	1.2 x .004	2	0.10	Li-like Al	15
Transient							
1995	19.0	32.6	.5 x .003	8	0.001	Ne-like Ti	71
Discharge							
1994	0.6	46.9	12 x .020	900	40	Ne-like Ar	4
1995	0.7	46.9	20 x .020	900	40	Ne-like Ar	65
Optical-Field-Ionization							
1993	20.0	13.5	.2 x .001	50 mJ	500 fs	H-like Li	70
1995	13.3	41.8	.8 x .010	70 mJ	40 fs	Pd-like Xe	69

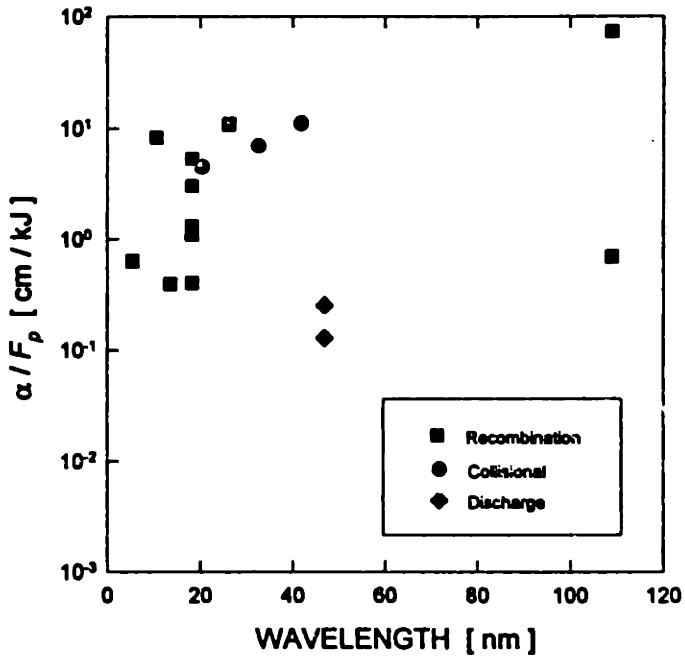

Figure 2.10: Fluence figure of merit. Table-top gain values of table 2.3 have been normalized to the excitation energy fluence in the plasma.

In the graphs of figures 2.9 and 2.10, the various table-top schemes have not been clearly distinguished. The two points at 109 nm are from the Auger pumped experiments. The capillary discharge data has been distinguished, as have the two MIT results, which are shown in gray.

It is interesting to compare the table-top results, figures 2.9 and 2.10, with the large system results, figures 2.4 and 2.5. There is a significantly larger variation in the $\frac{\alpha}{I_p}$ ratio for table-top lasers. This variation, over 10^5, is due to the recent use of ultrashort pump-laser pulses for table-top systems. The best table-top systems have an $\frac{\alpha}{I_p}$ ratio an order of magnitude larger than the high energy soft x-ray laser systems. In terms of pump-laser energy, the $\frac{\alpha}{F}$ ratio for the table-top systems is also about a factor of 10 larger than for the high energy systems. The $\frac{\alpha}{F}$ ratio varies by about 10^2 for both the table-top and large laser systems.

These graphs do not show dramatic improvements in the $\frac{\alpha}{I_p}$ and $\frac{\alpha}{F}$ ratios, and should not. This can be understood by considering the lasant plasma. For lasing action to occur, in a given plasma, the ion or electron density and electron temperature must reach certain values. These values are weakly dependent on pump-laser systems and pumping methods. Table 2.3 shows a large reduction in total pump-laser energy, up to two orders of magnitude, which is not reflected in the graphs. Other advantages of the table-top systems are increased firing rates, and greatly

reduced system costs, which are not reflected in the graphs or tables.

2.5 Conclusion

Soft x-ray lasing has predominantly been explored in *recombination* and *collisional* lasing schemes. In a recombination soft x-ray laser, an inversion occurs as fully stripped ions rapidly recombine with free electrons. In collisional lasers, an inversion is created by collisional excitation from the ground state to the upper laser level in a prepared ion. These two schemes were proposed in the 1960's and 70's, and were initially investigated with large high energy drive-lasers, which were used to create the soft x-ray lasing plasmas. Since the late 1980's, there has been growing interest in developing compact table-top soft x-ray lasers. Saturated, or near saturated amplification has been demonstrated with the high energy systems, and with recent novel table-top systems, such as Auger pumped, capillary discharge pumped, optical-field-induced ionized, and transiently pumped systems. Gain-length products larger than 4.5 have not been demonstrated with the short pulse, scaled down table-top systems, such as the one at MIT. Pump-laser energy required for the table-top systems is typically less than 10 J, which is up to two orders of magnitude less than the high energy systems. Recent results with novel table-top EUV lasing schemes, such as transiently pumped and optical-field-ionized lasing, indicate the feasibility of compact, high repetition rate, extreme ultraviolet lasers. Further development may result in sources suitable for soft x-ray applications.

Chapter 3

Analysis of Extreme Ultraviolet Amplification

3.1 Introduction

3.1.1 Topics Discussed

Several aspects of extreme ultraviolet amplification are analyzed in this chapter. The topics addressed in this chapter have been chosen because of their relevance to the experimental studies. Topics discussed include plasma heating, positive and negative absorption, beam refraction, and properties of amplified spontaneous emission. Particular attention will be devoted to properties of amplified spontaneous emission from a long thin plasma, because of its importance in interpreting experimental results.

3.1.2 Limits of the Analyses

A thorough analysis of soft x-ray laser theory in laser-produced plasmas requires sophisticated numerical simulations and is beyond the scope of this thesis. Such simulations reflect the complexity of the problem. For example, a reasonable simulation would incorporate hydrodynamics, which determines the plasma density profiles during expansion after illumination by the drive-laser pulse, plasma heating, which determines the peak electron temperature as a function of time, ionization balance, which determines the abundance of lasant ions, level excitation and de-excitation rates, which determine the level populations and presence of an inversion, and finally soft x-ray propagation in the plasma. Many of these components are interdependent. The plasma density profile determines the amount of pump-laser absorption [19] which affects the peak electron temperature. Both the electron temperature and local electron density determine the ionization balance, and the excitation and de-excitation rates. Additionally, the processes

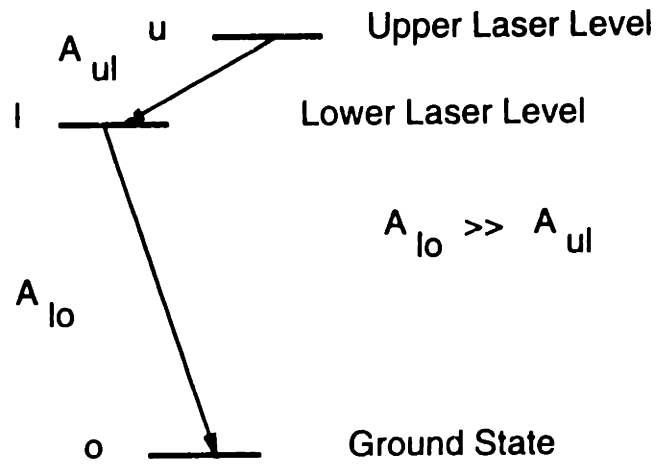

Figure 3.1: Three-level model. A simple three-level model is used to estimate EUV gain. Lasing is expected to occur between the upper u and lower l lasing levels. The lower lasing level radiatively decays to the ground state.

are transient, since the pump-laser pulse durations are typically less than one nanosecond, and short wavelength emission from the plasma typically terminates in a few nanoseconds.

Several assumptions will be made in the following analyses. These assumptions will be stated for each model. For most of the topics discussed, it is assumed that conditions in the laser-produced plasma are appropriate for EUV gain. Indeed, this has been the premise which motivated the experimental studies. The gain region in the plasma is assumed to be homogeneous and straight. It is also assumed that the gain-length product in the plasma is substantially below the saturation value of about 16. With these assumptions, the models of positive and negative absorption in a long narrow rod are developed.

The analyses of absorption and gain will be based upon a simple three-level atomic model, which has been developed elsewhere [60,5, page 99]. The levels are pictured in figure 3.1. Stimulated emission is expected to occur between the upper lasing level, designated with the subscript u, and the lower laser level, l. The ground state o is the lower state for radiative transitions from the lower laser level. Although the three-level model makes several approximations, this approach has been used to provide rough estimates of EUV gain [60,5].

3.2 Plasma Heating

When the high-power pump-laser illuminates the target surface, lasant material is ablated from the target, and heated. The result is a small expanding plasma near the target surface. A density profile is established in the plasma, and pump-laser absorption continues to heat the plasma until the termination of the pump-laser pulse, which is in 20 ps to 200 ps for our system.

Most absorption occurs near the plasma's critical surface. The critical surface is the location at which the pump-laser propagation constant, $k_u = \omega_u\sqrt{\mu\epsilon\omega_u}$, becomes imaginary. $\epsilon(\omega_u)$ in the plasma is given by the relation [75]

$$\epsilon(\omega_u) = 1 - \frac{\omega_p^2}{\omega_u^2} \tag{3.1}$$

where ω_u is the pump-laser frequency and ω_p is the plasma frequency: $\omega_p^2 = 4\pi N_e r_0 c^2$. N_e is the electron density, r_0 is the classical electron radius 2.8×10^{-13} cm [5, page 23]. Equating ω_u to ω_p gives the electron density at the critical surface, N_{cr}. For our system, the wavelength of the pump-laser is 1.053 μm, which gives $N_{cr} = 1.0 \times 10^{21}$ cm^{-3}.

This value of electron density is substantially higher than the value for the region at which gain is expected. Gain is expected where $N_e \sim 10^{19}$ cm^{-3} [5, page 37]. At higher densities, the collisional de-excitation rate from the upper to lower laser level increases and destroys the population inversion. The optimum value for electron density in the gain region will be estimated in the following section. Consequently, the heat at the critical surface must be transported to the region of gain for collisionally excited EUV lasers.

At the critical surface, the absorbed intensity must be dissipated by the electrons. The balance of absorption and heat transport at the critical surface is characterized by [19, page 2]

$$I_{abs} = f\sqrt{T_e/m_e}N_{cr}T_e \tag{3.2}$$

where f is a "flux limiting" factor, $f < 1$. T_e is the electron temperature in eV. In general, the value of f depends upon the pump-laser pulse length and intensity, a dependence which is not well understood. The absorbed intensity is a fraction of the incident pump-laser intensity, $I_{abs} = \eta I_{inc}$, where $\eta \approx 0.2 - 0.4$ for slab targets [76].

For a given pump-laser intensity, equation 3.2 can be used to estimate the electron temperature in the plasma. For our experiment, the maximum intensity delivered to a 4 mm length of plasma is about 1.8×10^{13} W cm^{-2}. Using $f \approx 0.1$ [77], gives an electron temperature of

about 290 eV, or 150 eV for an 8 mm plasma. Although a crude estimate, experimental results suggest that the estimated temperature is within a factor of two of the observed temperature.

Since the electron distribution is Maxwellian, the high energy tail of the distribution will ionize atoms with ionization potentials above the estimated electron temperatures by a factor of two or three. Possible lasing schemes are selected based upon the ionization potential of the lasant ion, and the excitation energy from the ground state to the upper laser level. Lasants with excitation energies less than two to three times the estimated electron temperature have been selected for the experimental studies.

3.3 Positive and Negative Absorption

In this and the following section, small signal gain values will be crudely estimated for the recombination and collisional lasing schemes. The analyses closely follow those of Elton [5]. However, in Elton's work, the equations have been condensed to scaling relations, in wavelength or atomic number, which are valid only for restricted cases. For example, Elton's scaling relations for gain in recombination lasers is based on the H-like ion sequence and is not valid for Li-like or Na-like estimates. Also, his analysis of Ne-like gain is based on local empirical scaling relations within the Ne-like sequence. In this section, essential equations have been gathered in generalized form, which facilitates their application to different wavelengths and ion sequences.

3.3.1 The Absorption Coefficient

When radiation propagates through a medium, which has two atomic levels with an energy separation corresponding to the radiation wavelength, the change in intensity for a small propagation length dz is given by [5, pages 19-28]

$$dI/dz = [N_u \sigma_{stim} - N_l \sigma_{abs}]I \tag{3.3}$$

where N_u is the density of electrons in the upper level, N_l is the density of electrons in the lower level, σ_{stim} is the stimulated emission cross section, and σ_{abs} is the absorption cross section. Equation 3.3, which is valid in the small signal regime, can be integrated and rewritten as

$$I(z) = I_0 \exp[\alpha z] \tag{3.4}$$

where

$$\alpha = N_u \sigma_{stim}(1 - \frac{N_l g_u}{N_u g_l}) \tag{3.5}$$

is the absorption coefficient, and g_u, g_l are the statistical weights of the upper and lower levels. The quantity in parentheses in 3.5 is referred to as the inversion fraction, F [5, page 22]. When the population is inverted, $N_u g_l > N_l g_u$, then the medium exhibits negative absorption, or gain, $\alpha > 0$. If the population is not inverted, the incident intensity will be absorbed as it propagates through the medium.

The stimulated emission cross section σ_{stim} can be expressed in terms of the spontaneous emission rate A_{ul} and transition linewidth $\Delta\lambda$. Also, A_{ul} may be related to the absorption oscillator strength f_{lu} [5, page 23].

$$A_{ul} = 8\pi^2 r_0 c \frac{g_l}{g_u} \frac{f_{lu}}{\lambda^2} \tag{3.6}$$

λ is the wavelength of the upper to lower level radiation. The resulting expression for the stimulated emission cross section of a Doppler broadened line is [5, page 27]

$$\sigma_{stim} = \pi r_0 \lambda \frac{g_l}{g_u} f_{lu} \sqrt{\frac{Mc^2}{2\pi T_i}} \Gamma(\lambda) \tag{3.7}$$

where $\Gamma(\lambda)$ is a normalized lineshape function, which is Gaussian for the Doppler broadened transitions. At line center, $\Gamma(\lambda) = 0.94$. M and T_i are the ion mass and ion temperature. For the plasmas produced in our experiments, the ion temperature is expected to be about $\frac{1}{10}$th the electron temperature.

Equation 3.7 can be used to obtain a numerical value for σ_{stim}, which can be used in equation 3.5 to estimate the small-signal gain coefficient. To obtain a value for α, the values N_u and F must be estimated. Note that $F \sim \frac{N_l}{N_u}$. Therefore, the population of the upper, and population ratio of the lasing levels must be found. These values are determined with an approach which depends upon the lasing scheme, collisional or recombination.

3.3.2 Estimating the Optimum Electron Density

Lasing action occurs in the plasma at an optimum electron density, $N_{e,opt}$. It will be shown that N_u and $\frac{N_l}{N_u}$ strongly depend upon N_e. The optimum electron density corresponds to a density at which the collisional de-excitation of the upper laser level approaches the radiative decay of the lower laser level [5, page 36]. The optimum electron density, in units of cm^{-3}, is found from the relation [5, page 36,106]

$$N_{e,opt} = c_1 \frac{5.7 \times 10^{26}}{< g_{ul} >} \frac{A_{lo}}{A_{ul}} \frac{\sqrt{T_e/\Delta E_{ul}}}{\lambda^{3.5}} \tag{3.8}$$

where $< g_{ul} >$ is a Gaunt factor, and λ is expressed in Angstroms. Equation 3.8 may be used for both collisoinal and recombination schemes to estimate $N_{e,opt}$, although the Gaunt factor differs for each scheme: $< g_{ul} > \approx 0.2$ for recombination schemes and $< g_{ul} > \approx 1.5$ for collisional schemes [5, pages 37, 106]. The constant c_1 is an adjustable parameter to match analytic results [5] with experimental results, and may vary with lasing schemes. For the H-like recombination and Ne-like collisional schemes discussed in this chapter, $c_1 \approx 0.1$.

Approximations of N_u, $\frac{N_l}{N_u}$ and α will be described for each lasing scheme in the following subsections. For collisional lasing, the upper-lasing-level population and upper-to-lower level ration can be estimated more easily than can be done for recombination lasing. Estimates will be derived first for collisional lasing schemes, and then for recombination schemes.

3.3.3 Estimating N_u and $\frac{N_l}{N_u}$ for Collisional Amplifiers

Once the optimum electron density is determined, the upper level population may be estimated for collisionally pumped schemes. In collisionally pumped schemes, the upper level is populated primarily by collisional excitation from the ground state. The upper level population can be written [5, page 27]

$$N_u = N_o \frac{P_{ou}}{D_u} \tag{3.9}$$

where P_{ou} is the pumping rate from the ground state, and D_u is the decay rate out of the upper state. This decay rate may be composed of spontaneous decay and collisional de-excitation. The pumping rate is related to the electron density and collisional excitation rate coefficient, C_{ou}.

$$P_{ou} = N_e C_{ou} \tag{3.10}$$

The excitation rate coefficient is given by [5, page 101]

$$C_{ou} = 1.6 \times 10^{-5} \frac{f_{ou} < g_{ou} >}{\Delta E_{ou} \sqrt{T_e}} \exp[-\frac{\Delta E_{ou}}{T_e}] \tag{3.11}$$

which applies to excitation from a lower to higher energy level. An expression similar to equation 3.10, weighted by a Boltzmann factor, is used with 3.11 to obtain equation 3.8. The ground state population is related to the local electron density

$$N_o = \kappa \frac{N_e}{Z_i} \tag{3.12}$$

where κ represents the fractional abundance of lasant ions in the plasma, and Z_i is the number of ionized electrons for the lasant ion species. For the Ne-like and Ni-like lasants considered in

this study, D_u is expected to be dominated by collisional excitation to nearby $\Delta n = 0, \Delta l = 1$ levels [60,5, page 108]. So,

$$D_u = N_e C_{ui} \tag{3.13}$$

where C_{ui} is the excitation rate coefficient, calculated from 3.11, from the upper to nearby energy level, designated with the subscript i.

The expressions 3.9, 3.10, 3.11, 3.12, and 3.13 can be combined to give

$$N_u \approx \kappa \frac{1}{2} \frac{N_{e,opt}}{Z_i} \frac{\Delta E_{iu}}{\Delta E_{uo}} \frac{f_{ou} < g_{ou} >}{f_{ui} < g_{ui} >} \exp[-(\Delta E_{uo} - \Delta E_{iu})/T_e] \tag{3.14}$$

The factor of $\frac{1}{2}$ appears in this equation because the excitation rate coefficient for monopole transitions, $\Delta n = 1, \Delta l = 0$ is found to be one-half the value for dipole transitions $\Delta n = 1, \Delta l = 1$ [5, page 105]. It should be noted that the upper level population in 3.14 shows a strong temperature sensitivity. Recall also that $N_{e,opt} \sim \sqrt{T_e}$ from equation 3.8. Further, the value of κ, the ion abundance fraction depends upon temperature; at very low temperatures the ion may not be produced. Equation 3.14 gives an estimate of the upper level population.

The ratio $\frac{N_l}{N_u}$ can be determined from a steady state solution to the lower lasing level rate equation. In steady state, this yields [5, page 56]

$$\frac{N_l}{N_u} = \frac{N_e C_{ul} + A_{ul} + \varepsilon N_e C_{ol}}{N_e C_{lu} + \xi A_{lo}} \tag{3.15}$$

where $\varepsilon = \frac{N_o}{N_u}$ and $\xi \leq 1$ is an escape factor for lower level radiation. Lower level radiation can be reabsorbed by the atoms, which effectively reduces the lower level radiative decay rate, A_{lo}. This effect can be minimized by reducing the width of the line focused pump-laser beam, which creates a narrower plasma. Equation 3.15 can be evaluated using expressions 3.6, 3.8, 3.9 and 3.11. When $\frac{N_l}{N_u}$ is estimated, the inversion fraction F can be determined. The results for N_u from 3.14, σ_{stim} from 3.7, and $\frac{N_l}{N_u}$ from 3.15 can then be used to estimate the small signal gain α for the collisional lasing scheme.

3.3.4 Estimating α for Collisional Amplifiers

Using the expressions of the last section, along with relevant tabulated atomic data [5,21,32], gain coefficients for neon-like calcium will be estimated. Ne-like Ca has been chosen as the best collisional lasing candidate, and has been shown to lase with much higher pumping energies [58]. The necessary electron temperature for ionization and collisional excitation of Ne-like Ca

should be attainable with our pump-laser, an assumption based upon our preceding temperature estimate.

For Ne-like Ca, the 2p-3p excitation energy is about 370 eV, and the ionization potential of Na-like Ca is 211 eV and [21]. Lasing is expected to occur at 38.3 nm between the 3p-3s, J=0-1 transition [78]. Assuming an ion temperature of 30 eV and an electron temperature of 150 eV, the stimulated emission cross section is calculated from 3.7 to be $\sigma_{stim} \approx 7.6 \times 10^{-15}$ cm^2, and the upper state population is determined from 3.14 to be $N_u \approx 3.2 \times 10^{15}$ cm^{-3}. Using the value $N_e = 2.7 \times 10^{18}$ cm^{-3} calculated from 3.8, and the rate coefficients calculated from 3.11, the inversion fraction is found to be $F \approx 0.9$. These values result in a small signal gain of $\alpha \approx 22$ cm^{-1} for Ne-like Ca. If a temperature of 100 eV is assumed, the gain drops to $\alpha \approx 5.9$ cm^{-1} for Ne-like Ca. This reduction reflects the temperature sensitivity of the collisional scheme, and the coarseness of the gain estimate.

3.3.5 Estimating N_u and $\frac{N_l}{N_u}$ for Recombination Amplifiers

For recombination lasing, the analysis follows the same procedure as above, although the system is more complicated. Recalling the discussion of chapter 2, recombination lasing is a transient lasing scheme. Gain appears after initially hot and stripped ions are allowed to cool. During the cooling process, electrons are captured by the ion and cascade down to the upper lasing level. Thus, recombination is the pumping mechanism for the upper laser level.

The pumping rate for the nth level in a recombining ion is given by [5, page 148]

$$P_{rec} = 16\pi^2 n^6 \alpha_f a_0^5 c \frac{N_e^2}{\Omega^6} \left(\frac{\chi}{T_e}\right)^2 \exp\left[\frac{\chi}{(n+1)^2 T_e}\right] \tag{3.16}$$

where α_f is the fine structure constant, a_0 is the Bohr radius in cm, Ω is the effective nuclear charge seen by the recombining electron, and χ is the ionization potential of the lasant species. This expression shows a strong temperature sensitivity, which is opposite that of equation 3.14. For recombination lasing, low temperatures are preferred during the lasing stage, while temperatures must initially be high to generate the lasant ion.

Expression 3.16 can be used in 3.9 to estimate N_u, once the depletion rate, D_u, is known. For recombination lasing, radiative decay from the upper lasing level to the ground state is the dominant decay mode. Since lasing occurs at low temperatures, the collisional rates are

negligible, see equation 3.11. Hence,

$$N_u \approx \kappa \frac{N_e}{Z_i} \frac{P_{rec}}{A_{uo}} \tag{3.17}$$

where 3.12 has been used.

The ratio $\frac{N_l}{N_u}$ now needs to be estimated for the recombination scheme. For this ratio, again we can consider radiative transitions to be the dominant populating mechanisms of the lower laser levels. This assumption is reasonable because of the low temperatures involved. Taking a steady state solution to the population rate equation for the lower laser level

$$\frac{d}{dt} N_l = N_u A_{ul} - N_l \xi A_{lo} \sim 0 \tag{3.18}$$

gives

$$\frac{N_l}{N_u} \approx \frac{A_{ul}}{\xi A_{lo}} \tag{3.19}$$

This equation along with 3.17 and 3.7 can then be used to estimate gain for the recombination lasing schemes.

3.3.6 Estimating α for Recombination Amplifiers

For H-like B, the ionization potential is 340 eV, and lasing is expected on the 3d-2p transition at 26.2 nm. The stimulated emission cross section, estimated from 3.7, is calculated to be $\sigma_{stim} \approx 4.6 \times 10^{-15}$ cm^2. From 3.8, $N_{e,opt} \approx 8.9 \times 10^{18}$ cm^{-3}, for which $c_1 = 0.1$ has been used. Using this value of electron density and a cooling temperature of $\frac{1}{10}$th the ionization potential, equation 3.16 gives a pumping rate of 1.0×10^8 s^{-1} into the upper level. The decay rate from the upper level is 3.5×10^{10} s^{-1}. Assuming a lasant ion fractional abundance of $\kappa \sim 0.3$, which is reasonable for our expected peak temperatures, the upper level population is estimated to be $N_u \approx 1.7 \times 10^{15}$ cm^{-3}. Using an escape factor value, $\xi = 0.5$, the inversion fraction is found from 3.19 to be $F = 0.58$. The values found for σ_{stim}, N_u and F give a small signal gain coefficient of $\alpha \approx 4.5$ cm^{-1} for H-like boron. A similar calculation for H-like carbon results in $\alpha \approx 10$ cm^{-1}.

It should be stressed that the calculated gain value for H-like boron is a rough approximation. The resulting value is very sensitive to both electron temperature and electron density. The dependence on density is cubic, from equations 3.16 and 3.17. Although a rough calculation, the value found for carbon is in rough agreement with experimentally reported values listed in tables 2.1 and 2.3 of chapter 2.

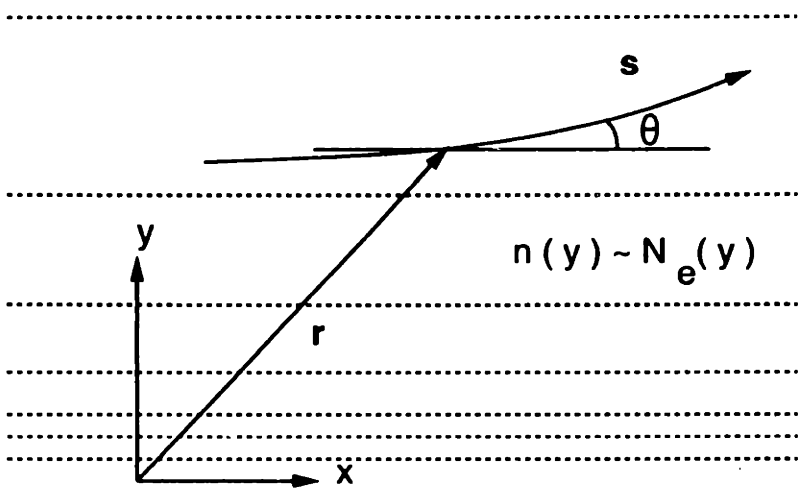

Figure 3.2: Soft x-ray laser beam refraction. Since the soft x-ray beam propagates in a medium with a spatially varying index, beam refraction will occur as shown. The deviation of the rays will be determined by the density gradient and lasing wavelength.

3.4 Beam Refraction

Before discussing the properties of amplified spontaneous emission, the issue of beam refraction [79] needs to be addressed. Since soft x-ray lasing is expected to occur in a plasma with substantial density gradients, the soft x-ray beam may refract as it propagates along the plasma column. Such refraction may cause the beam to deviate out of the gain region, which effectively reduces the gain-length product.

Refraction of a ray which propagates in the direction **s** in a medium with spatially varying refractive index $n(\mathbf{r})$, figure 3.2, is given by the following expression [80].

$$\frac{d}{ds}(n\frac{d\mathbf{r}}{ds}) = \nabla n \tag{3.20}$$

This equation follows from the eikonal equation of geometrical optics. In a low density plasma, where $n \approx 1$ and the ray propagates in a direction transverse to the density gradient, 3.20 can be simplified to

$$d\theta \approx \mid \nabla n \mid dz \tag{3.21}$$

where $d\theta$ is the angular deviation after traveling the incremental distance dz. For short wavelengths and low density, the variation in refractive index can be found from 3.1.

$$n \approx 1 - \frac{r_0}{2\pi}\lambda^2 N_e(y) \tag{3.22}$$

To simplify, the variation in electron density is taken to be in only the y-direction. Using 3.22 in 3.21 gives the angular deviation of the ray in terms of the electron density profile.

$$d\theta \approx \frac{r_0}{2\pi}\lambda^2\frac{dN_e}{dy}dz \tag{3.23}$$

With large gradients and long wavelengths, beam refraction may reduce the gain-length product.

Equation 3.23 may be solved numerically for a given density profile and lasing wavelength λ. After the first pump-laser pulse, the density profile may be taken as exponential [53,77] while a gentler profile is expected after the second laser pulse [77]. The density profile may be approximated locally as exponential in the gain region, and different values of the gradient chosen to determine when beam refraction becomes appreciable.

Several values of density gradient were chosen to numerically solve 3.23. It was found that for a wavelength of 26.2 nm and a gradient of 1.4×10^{22} cm^{-4}, the beam would refract out of the plasma after propagating 8 mm. This density gradient corresponds to a gain region 10 μm wide at the optimum electron density calculated for H-like B in section 3.4. For Ne-like Ca, the critical density gradient is 6.3×10^{21} cm^{-4}. At steeper gradients, narrower gain regions, or higher optimum densities, beam refraction will reduce the effective length of the plasma column.

Paths of three rays have been calculated for the H-like B amplifier at the critical density gradient, and are shown in figure 3.3. The rays originate at the end of the plasma column, and travel in regions of different electron density. Different regions of the plasma lead to slightly different angular deviations of the trajectories. Note that the difference in angular deviation can lead to an apparent convergence or divergence of the output beam. At the critical value of the electron density gradient, the rays refract out of the plasma column after about 8 mm, which in our experiments is the total length of the plasma.

3.5 Properties of Amplified Spontaneous Emission

In this section, the behavior of a spectral line which exhibits gain will be analyzed. Both nonlinear intensity growth as a function of plasma length, and output beam formation will be described. For these models, effects of beam refraction, discussed in the last section, and plasma inhomogeneities have been ignored.

The plasma column is assumed to be a uniform rod of length L, as shown in figure 3.4. The gain region, $\alpha > 0$ cm^{-1}, has radius R_g and is surrounded by a sheath, thickness T,

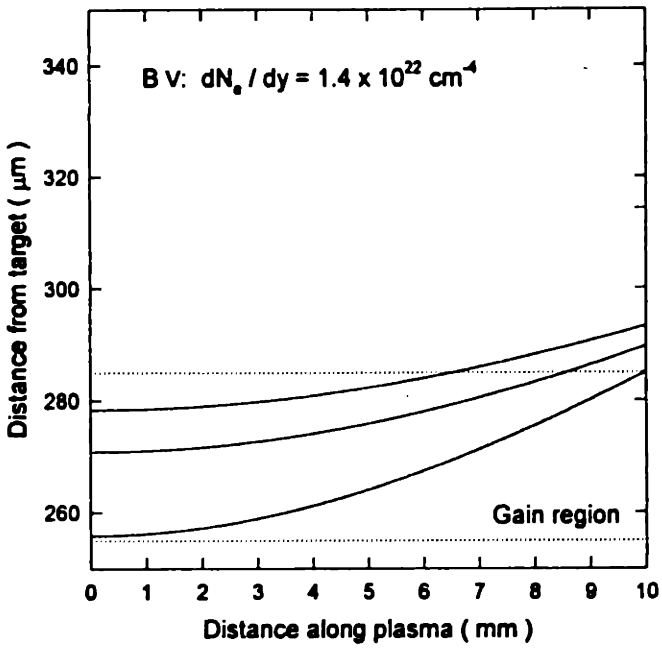

Figure 3.3: Extreme ultraviolet beam refraction. Because of the density gradient in the laser-produced plasma, the EUV rays, shown as solid lines, may refract out of the gain region, shown as the area between the dotted lines.

of plasma which is optically thin, $\alpha L << 1$, at the lasing wavelength. On one end, a slit of width W_s is placed a distance D_s from the plasma, and an aperture, radius R_a, is near a large area grating, radius $R_d > R_a$ which spatially integrates and spectrally resolves the plasma emission. This arrangement represents the streaked or imaging concave grating spectrometer (S/ICGS), which is used in our set-up to monitor line intensity as a function of plasma length. On the other end, a slit is placed near the plasma and a glancing incidence toroidal grating is used to spectrally resolve and spatially integrate, in one dimension only, plasma emission. This arrangement represents the time integrating flat-field spectrometer (TIFFS), which is also used in our experiments. Simulations of line intensity, in the presence of amplified spontaneous emission, for each spectrometer are carried out in the next two subsections.

3.5.1 Nonlinear Intensity Growth

Equation 3.4 suggests that line intensity will grow exponentially in the presence of gain, $\alpha > 0\ \mathrm{cm}^{-1}$. Since the gain is restricted to a finite bandwidth and emission is usually collected over a range of solid angles, such exponential growth may not be observed. The effect of finite bandwidth on gain has been analyzed by G. Linford, et. al. [81] and line intensity is predicted to grow

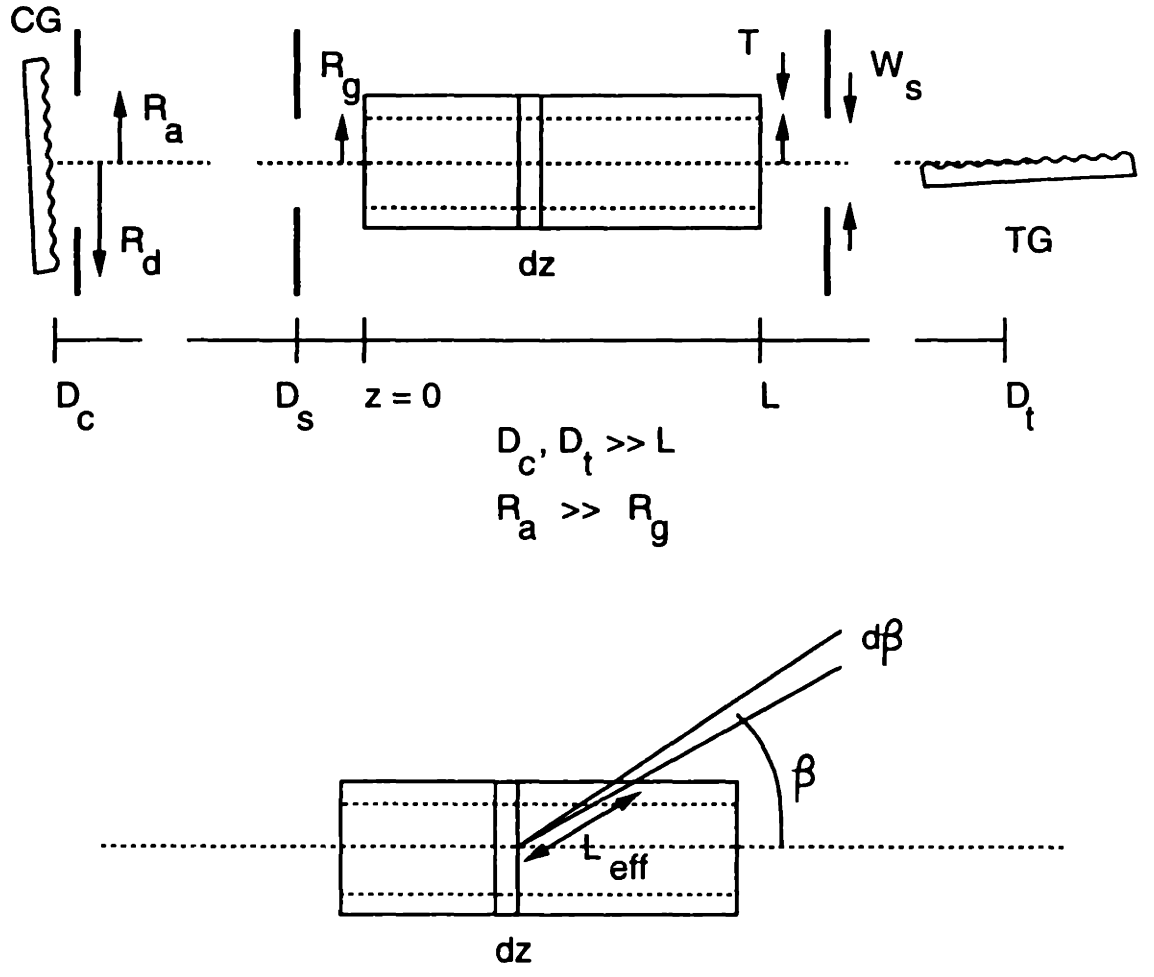

Figure 3.4: EUV amplifier and spectrometers. The illustrated arrangement is used to model line emission in the presence of gain. Notations used are length of gain region, L, radius of gain region, R_g, thickness of adjacent optically thin region, T, width of slit, W_s, distance to the slit, D_s, distance to concave grating, D_c, distance to toroidal grating, D_t, concave grating, CG, toroidal grating, TG, and radius of concave grating aperture, R_a.

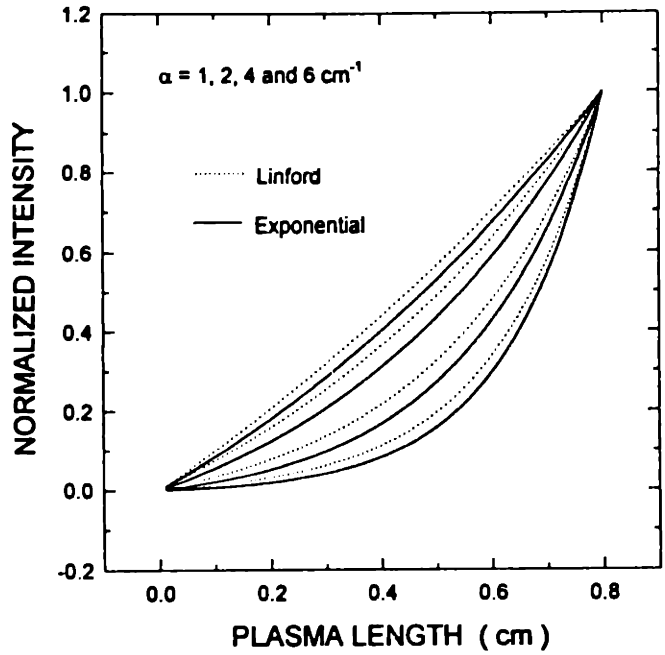

Figure 3.5: Comparison of Linford's formula with exponential intensity growth. An integration over frequency of the intensity growth equation results in a lower apparent gain value.

approximately according to the following expression.

$$I(L) = I_0 \frac{[\exp(\alpha L) - 1]^{\frac{3}{2}}}{[\alpha L \exp(\alpha L)]^{\frac{1}{2}}} \tag{3.24}$$

To obtain this expression, the equation of intensity growth 3.3 has been integrated over length and frequency [81,5, page 21]. Line growth according to equation 3.24 is compared with exponential growth, equation 3.4, in figure 3.5 where the peak intensities for each case have been normalized. The integration over frequency shows an observed gain which appears smaller than the exponential gain. Expression 3.24 is used to estimate gain for all nonlinear intensity growth measurements.

Equation 3.24 does not include the effects of off-axis emission which is usually gathered by a large area detector used in EUV amplifier experiments. The effects of off-axis emission has been analyzed numerically in two papers of a series on amplified spontaneous emission [82,83], although the effect of finite gain bandwidth was not included in this analysis. Off-axis emission is expected to result in a further apparent reduction of gain. An integration of the intensity growth equation 3.3 over length, frequency and solid angle is carried out in this section and the results are found to be in qualitative agreement with Allen and Peters' results [82,83], and in quantitative agreement with Linford's equation in the limit of small solid angle. The integration

can only be performed numerically.

To including the effects of gain bandwidth and off-axis emission, we modify the intensity growth equation as follows.

$$dP = J_s g(\nu)[\exp(\alpha g(\nu) z_{eff}) + \frac{2R_g T + T^2}{R_g^2}]\frac{d\Omega}{4\pi} d\nu dz \tag{3.25}$$

This expression represents the power contribution from a differential element, of length dz, of the plasma, see figure 3.4. The additional term inside the brackets represents emission from the adjacent optically thin sheath. The gain bandwidth profile $g(\nu)$ is taken to be Gaussian for the Doppler broadened lasing line. z_{eff} represents the effective length of gain material which emission travels through before reaching the detector. This length will vary from z, on axis, to a reduced value off-axis.

In typical EUV experiments, the aspect ratio of the gain region is large and the plasma is far from the spectrometers. This allows several small-angle approximations to be made. The differential solid angle can be written as $d\Omega \approx 2\pi\beta d\beta$, and the effective length can be expressed as $z_{eff} \approx R_g/\beta$ for $\beta > R_g/z$, see figure 3.4. Integration of 3.25 over length, angles and frequency gives the desired output power as a function of plasma length.

To incorporate the effects of the slit and aperture, the following method has been used. First, the radius of the aperture and its distance from the plasma determines the limit of integration over angles. Equation 3.25 is integrated and an output beam profile is determined at each plasma length. The output intensity profile is then approximated as a Gaussian. Then, an overlap integral of the Gaussian intensity profile with the slit and aperture is performed to determine the detected power at each plasma length.

The program ASE1 has been written to solve 3.25 for our system. The program has been tested in no-gain and small-aperture limits. With no gain, the observed intensity grows linearly. With small apertures, the intensity grows according to the Linford formula 3.24 as would be expected by only detecting on-axis emission. Typical values from our set-up which have been used in the program are, $L = 0.8$ cm, $R_g = 50\,\mu$m, $T = 10\,\mu$m, $W_s = 50\,\mu$m, $D_s = 1.5$ cm, $R_a = 0.9$ cm and $R_d = 1.6$ cm. Results from ASE1 for several small signal gain values are compared with the Linford results in figure 3.6. Because of off-axis emission, the apparent gain is further reduced.

Including the effects of frequency and angle integration is essential in interpreting results of gain measurements. If considerable off-axis emission is collected, small gain-length values may

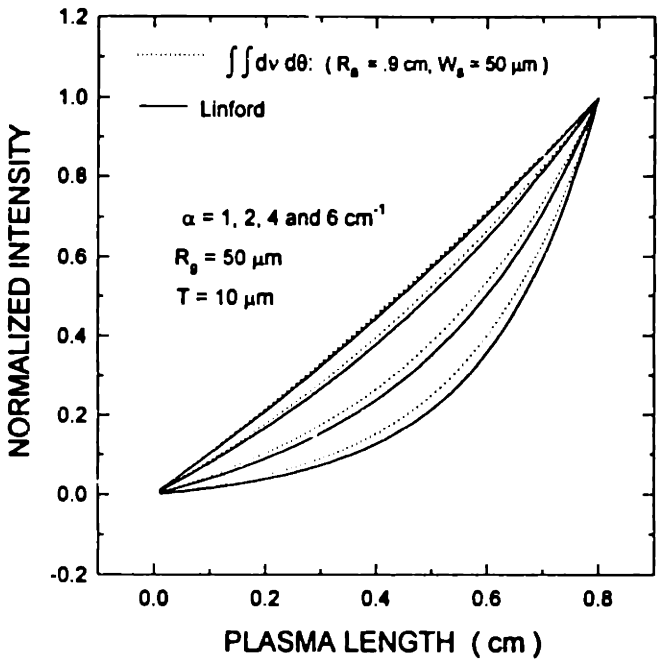

Figure 3.6: Frequency and angle integrated intensity growth compared to the Linford formula. The frequency and angle integrated results, dotted lines, show a smaller apparent gain than the Linford expression, solid lines.

not be detectable. If gain is detected, its actual value may be as much as twice the measured value. Care must be taken in detection assembly and data analysis. These issues will be discussed further in chapter 5.

3.5.2 Beam Formation

When gain occurs in the plasma column, an output beam will begin to form. The divergence of the beam will depend on the geometry of the gain region, and the value of the small signal gain. For very low gain, the beam divergence will approach 4π steradians, and for very high gain, the divergence will approach the geometric value set by the gain region, $\frac{2R_g}{L}$. Observation of beam formation indicates the presence of amplified spontaneous emission.

In the experimental set-up, beam formation can be detected with the time integrating flat-field spectrometer. This spectrometer spatially integrates line emission from the plasma in one dimension only. The resulting image of spontaneous emission is a long thin line. When ASE occurs, the image will become a localized spot as the gain increases, while nearby spontaneous emission lines will remain long and thin.

The output beam profile has been determined from equation 3.25 and the program ASE1.

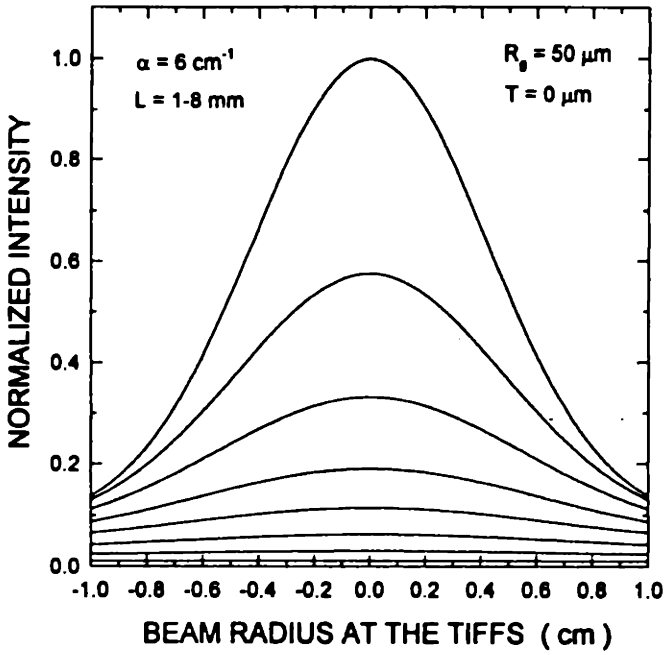

Figure 3.7: EUV beam formation. For a long rod which exhibits gain, a beam will form with increasing gain-length product. The resulting beam will appear as localized emission at the time integrating flat-field spectrometer (TIFFS) image plane.

At each plasma length z, 3.25 is integrated over frequency and angle. The amount of power in the differential angle $d\beta$ is mapped to the image plane for each angle β. Contributions from the entire plasma column are summed to obtain the resulting beam profile. Because the gain region is assumed to be a uniform rod, and because small angle approximations have been made, the resulting beam profile is flat-topped. This profile has been approximated by a Gaussian with a constant offset.

Beam formation for an 8 mm long plasma and a gain of $\alpha = 6\ \mathrm{cm}^{-1}$ is shown in figure 3.7. Intensity profiles are calculated for plasma lengths of 1 through 8 mm, in 1 mm increments. The intensity profiles are calculated at the image plane of the TIFFS, which is 2 cm wide. For the high gain-length product used, a localized spot would be readily observed.

In figure 3.8, intensity profiles at the TIFFS image plane are calculated for several gain values. Emission from the adjacent sheath has been included in this simulation, $T > 0$. The results show that beam formation is clearly evident for gain-length products over 1.6.

Finally, in figure 3.9 the beam divergence is plotted as a function of gain-length product for a plasma length of 8 mm. This result is qualitatively similar to the result of Allen and Peters [83], although the two results differ as $\alpha L \rightarrow 0$. In figure 3.9, the beam divergence diverges

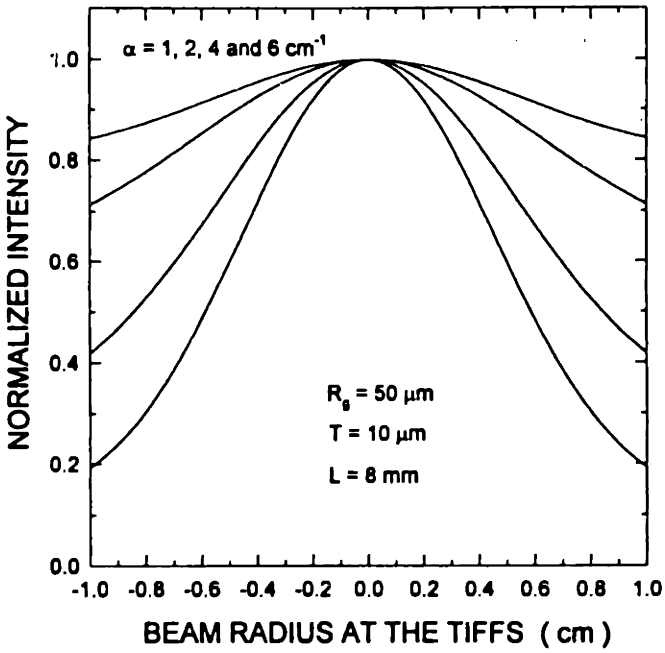

Figure 3.8: Beam formation for various values of small signal gain. With gain-length products over 1.6, beam localization at the TIFFS is clearly observed.

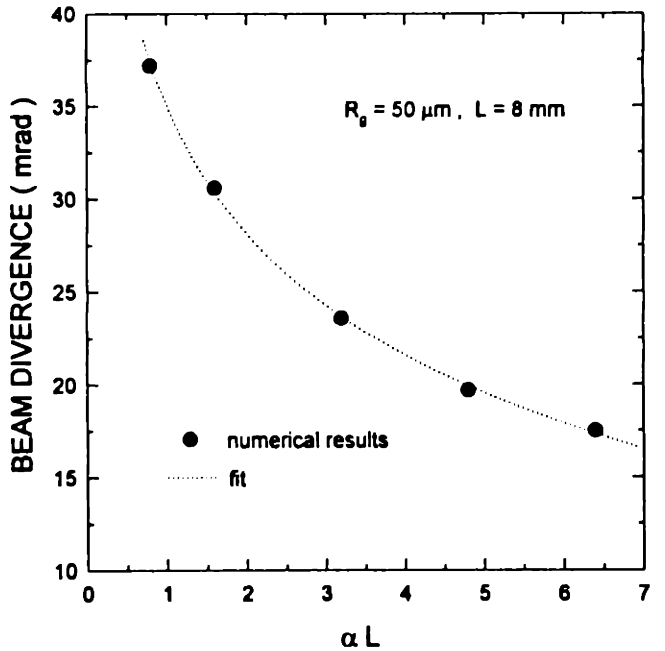

Figure 3.9: Beam divergence. The divergence of the ASE beam decreases with increasing gain-length product. For this plot, the length of the gain region has been fixed at 8 mm.

as $\alpha L \rightarrow 0$, which is reasonable since no beam forms with purely spontaneous emission. The result of Allen and Peters shows the divergence approaches a finite limit as $\alpha L \rightarrow 0$, which is not physically reasonable.

Results from the simulations of amplified spontaneous emission can be used to determine the actual small signal gain value, the minimum detectable gain, and the geometry of the gain region. The actual gain value can be determined from the measured value and knowledge of the detector apertures. The minimum detectable gain will also be determined by the detector apertures. This issue will be discussed in chapter 5. The geometry of the gain region can be determined from measurements of nonlinear intensity growth and beam formation. The intensity growth measurement will give the value of α, which can be used with a measurement of beam divergence to determine the gain region radius. Knowing the size of the gain region will also provide some information about the plasma density profile. The ASE simulations are very useful in interpreting gain measurements.

3.6 Line Absorption

For non-lasing lines, or in the absence of gain $\alpha < 0$ cm^{-1}, the plasma will absorb radiation. This effect can be described by equation 3.25 where the gain coefficient now takes on negative values. The analysis of the last section can then be used to simulate line absorption.

Intensity growth as a function of plasma length has been simulated for several values of α in figure 3.10. The results are compared to the Linford analysis. For the simulation, it has been assumed that there is no adjacent spontaneous emission. Comparing figure 3.10 with figure 3.6 show that detection of line absorption, or opacity, is more difficult than detection of gain. This is because off-axis emission can comprise most of the detected signal in the case of absorption. The problem worsens when adjacent spontaneous emission is included in the simulation, figure 3.11. The intensity growth of an absorbed line rapidly becomes linear when adjacent spontaneous emission is added or greater off-axis emission is collected.

Intensity profiles at the TIFFS image plane for optically thick lines are shown in figure 3.12. These profiles were calculated with the program ASE1, and show an intensity depression on the axis of the plasma column. The intensity depression should be readily detectable for absorption-length products below - 3.0. The results for line absorption indicate that detection of optically thick lines may best be achieved with the TIFFS.

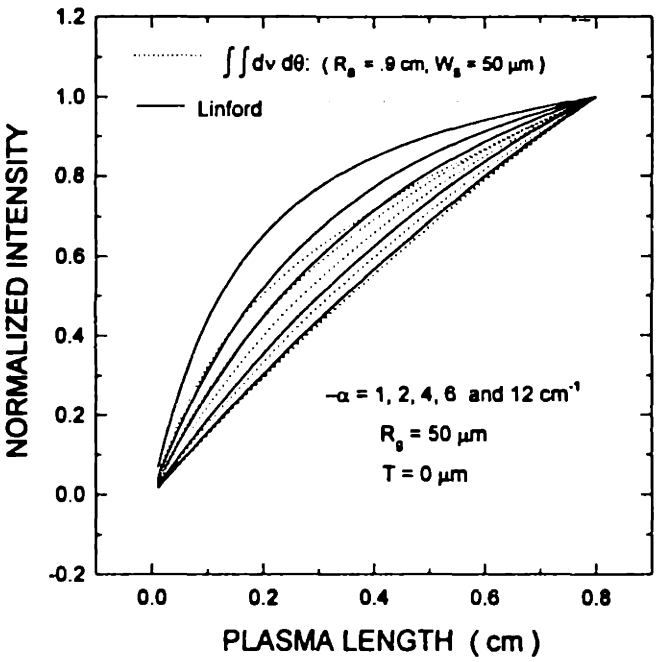

Figure 3.10: Intensity growth of an absorbed line. Frequency and angle integrated intensity as a function of plasma length for an absorbed emission, dotted lines, is compared to the Linford result, solid lines.

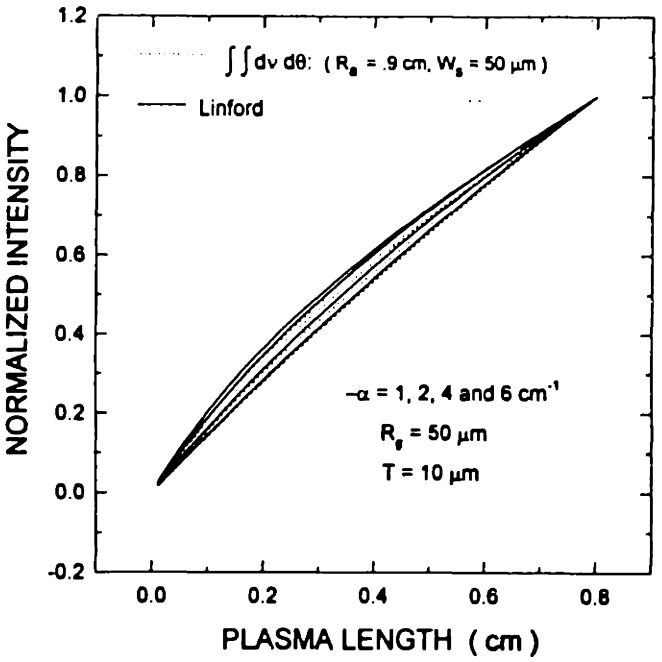

Figure 3.11: Intensity growth of an absorbed line with adjacent spontaneous emission. The intensity growth rapidly becomes linear when adjacent spontaneous emission is included in the simulation.

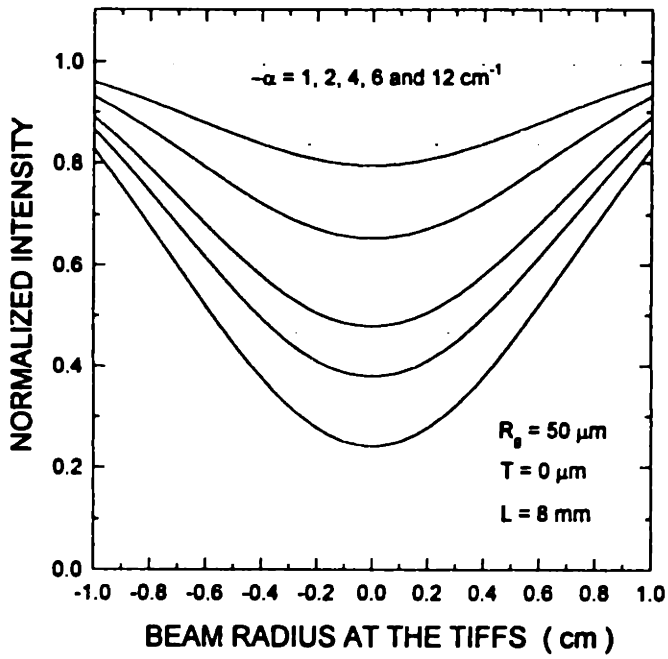

Figure 3.12: Intensity profiles of absorbed lines. An intensity depression appears on-axis for an optically thick line. The width of the depression depends upon the geometry of the plasma column.

3.7 Summary

A simple plasma heating analysis suggests that an electron temperature of about 150 eV should be produced in an 8 mm × 40 μm plasma column. Results from basic three-level models for collisional and recombination lasants indicate that gain-length products above 3 for Ne-like Ca and H-like B should be achieved for our experimental conditions with the electron temperature estimated above. Properties of amplified spontaneous emission have been described, and numerical simulations suggest that gain-length products over 3 should be readily detectable with the two spectrometers used in this study. Also, optically thick lines with absorption-length products below - 3 should be detectable with the TIFFS. Results from numerical simulations of amplified and absorbed spontaneous emission, will be useful in interpreting spectral data.

Chapter 4

The MIT Table-Top Extreme Ultraviolet System

4.1 Introduction

The MIT table-top extreme ultraviolet system is described in this chapter. First, an overview of the system is presented. Then, the three main components of the system, which are the pump-laser, the target chamber, and the EUV spectrometers, are described in greater detail. Most of the discussion is devoted to the pump-laser and the spectrometers. Alignment of the spectrometers and pump-laser beams is also described in this chapter. It is hoped that this chapter will provide a useful reference for operation of the table-top system.

4.2 Overview of the System

A block diagram of the MIT table-top EUV system is illustrated in figure 4.1. Three major components comprise the table-top system. These components are the pump-laser, the high-vacuum target chamber, and the EUV and soft x-ray spectrometers.

The pump-laser system system consists of a commercial mode-locked, Q-switched Nd:YLF oscillator/amplifier, supplied by Lumonics LTD, which has been modified [77] to deliver an optically isolated and nearly flat-top beam. This master oscillator/amplifier normally delivers a 300 ns train of 60 ps, 10 mJ pulses separated by 7.5 ns. One or several pulses may be selected internally from the oscillator pulse train for amplification with a high speed Pockel's cell. Pulse lengths and energies may be increased to 210 ps and 25 mJ by inserting an etalon into the oscillator cavity and reducing the RF power to the acousto-optic mode-locker.

The master oscillator/amplifier is followed by a chirped pulse amplification (CPA) stage.

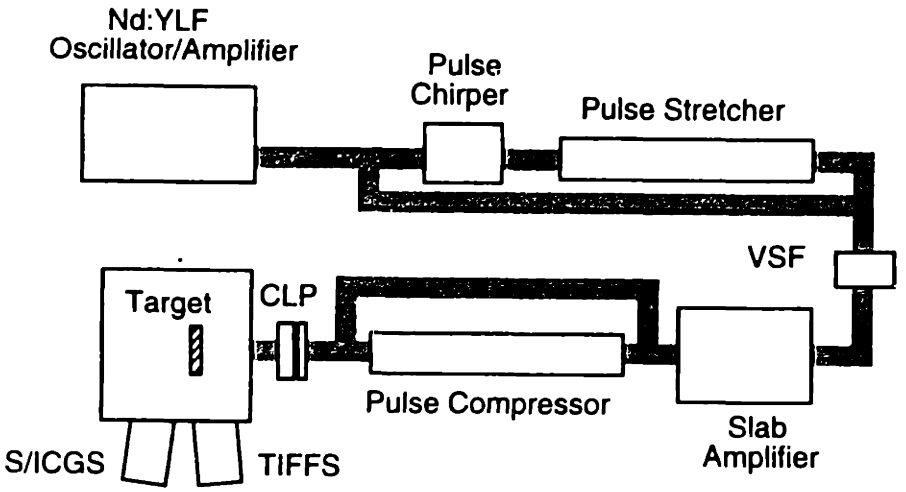

Figure 4.1: Block diagram of the MIT table-top EUV system. The system consists of a pump-laser, a high-vacuum target chamber, and two short wavelength spectrometers. VSF, vacuum spatial filter. CLP, cylindrical lens pair. TIFFS, time integrating flat-field spectrometer. S/ICGS, streaked or imaging concave grating spectrometer.

This stage consists of a bulk glass pulse chirping and spatial filtering assembly, a grating pair pulse stretcher, and grating pair pulse compressor. High power amplification is achieved in the CPA stage with an in-house zig-zag slab amplifier which is preceded by a beam shaping and filtering stage [77]. The pump-laser beam is focused with a cylindrical lens aplanat into the vacuum chamber.

The CPA stage has been designed such that various sections can be by-passed as shown in figure 4.1. This enables discrete pulse length adjustment. In short pulse mode, the pump-laser generates pulses as short as 20 ps with energies of 0.8 J. In long pulse mode, pulse lengths of 210 ps and pulse energies of 3.0 J have been achieved. The current system can provide a range of pumping conditions, which was not possible for initial gain studies [1,2] where only 60 ps, 1.0 J pulses were used.

The high-vacuum target chamber houses the laser-produced plasma and spectrometers. The chamber was designed by Dr. S. Basu and constructed by Huntington Vacuum Corporation. The chamber is large, 260 liters, and is evacuated with mechanical and turbomolecular vacuum pumps. The typical pump-down time of the chamber is about 45 minutes.

Two spectrometers are used to study plasma emission. One spectrometer is a streaked or imaging concave grating spectrometer (S/ICGS), and the other is a time integrating flat-field spectrometer (TIFFS). In streaked mode, the S/ICGS gives spectrally and temporally resolved traces of atomic lines. In imaging mode, the S/ICGS gives spatially and spectrally resolved images of plasma emission. The TIFFS focuses in, one dimension, spectrally resolved emission from the plasma onto a flat image plane. The S/ICGS covers a wavelength range from 18 nm to 42 nm, and the TIFFS covers a range from 3 nm to about 11 nm.

4.3 CPA for Long Pulse Lasers

For our first gain studies, the pump-laser could be operated only in 60 ps, 1 J mode. Being able to vary the pump-laser pulse length, would allow pumping at higher peak intensities, with shorter pulses, or at higher pumping fluence, with longer pulses. To achieve variable pulse length, the technique of chirped pulse amplification (CPA) was used [12] for our pump-laser system. This allowed pulses as short as 20 ps at 800 mJ to be generated with the pump-laser. Bypassing the final pulse compressor, see figure 4.1, resulted in 120 ps pulses at about 2 J. Using an intracavity etalon in the master oscillator, and reducing the RF power to the mode-locker, lengthened the pulses to 210 ps. For the long pulses, the pulse energy could be increased to 3 J. These modifications to the pump-laser allowed greater flexibility in exciting the laser-produced plasma.

Normally, CPA is applied to short pulse, < 20 ps, low energy, < 1 μJ, lasers. The bandwidth of the pulse is broadened in long optical fibers, which preserve the Gaussian beam profile. The amount of bandwidth broadening is roughly inversely proportional to the initial pulse width times the fiber length. Since the final pulse duration after compression is inversely related to the final pulse bandwidth, substantial bandwidth broadening is desired. Long optical fibers are well suited for CPA with short pulse, low energy lasers.

Unfortunately, the master oscillator used in these experiments could only produce pulses as short as 56 ps with energies of 20 μJ, which presented a challenging problem. The pulse energy exceeds the damage limit of optical fibers. Attenuation of the oscillator pulse energy would allow the use of optical fibers for bandwidth broadening, however the attenuation and the losses associated with the grating pair stretcher and compressor could not be recovered with both amplifiers. For this reason, bulk SF_6 glass was chosen as the bandwidth broadening medium.

Although bulk material has been used for high energy, short pulse compression [84], the method used in this experiment was the first such demonstration of high energy, long pulse compression, to the author's knowledge.

4.3.1 Self-phase Modulation in SF_6 Glass

Most optical materials exhibit the Kerr effect, which is an index change proportional to the square of the applied electric field, [85]. At high optical intensities, I, the Kerr effect results in an intensity dependent refractive index

$$n = n_0 + n_2 I \tag{4.1}$$

where n_2 is the materials nonlinear index [85, page 278]. SF_6 glass has a very high nonlinear index, $n_2 = 9 \times 10^{-13}$ esu. The high intensities of a short optical pulse will modify the refractive index of the material through which it propagates. This in turn will modulate the phase of the optical field. This phenomena is known as self-phase modulation.

Propagation of a high intensity optical pulse through a nonlinear medium is described by the nonlinear Schrodinger equation.

$$-2i\frac{\partial}{\partial z}E + \frac{\partial^2\beta}{\partial\omega^2}\frac{\partial^2}{\partial\tau^2}E = \kappa \mid E^2 \mid E \tag{4.2}$$

The transformation $t \equiv \tau + z\frac{\partial\beta}{\partial\omega}$ has been used in obtaining 4.2. β is the frequency and intensity dependent propagation constant, and $\kappa \propto n_2$, see [85, page 282] and [86]. The term on the right side of 4.2 results from 4.1.

Equation 4.2 has been solved numerically for dispersive and weakly dispersive materials [87]. Since our master oscillator operates at 1.053 μm and SF_6 glass is used for spectral broadening, the results for weakly dispersive materials applies to our system. For weakly dispersive materials, the bandwidth broadening factor, or final pulse compression factor with optimum compressor design, has been approximated by the following relation [87].

$$\frac{\tau_0}{\tau} \approx \frac{\Delta\nu}{\Delta\nu_0} \approx 1 + \kappa I_p L \tag{4.3}$$

The value of κ depends upon the nonlinear material used and the laser wavelength. For our laser and the SF_6 glass, κ evaluates to 7.3×10^{-11} cm W^{-1}. I_p is the peak optical intensity in the glass, and L is the length of the SF_6. The estimated value of I_p is 1.8×10^{10} W cm^{-2} and

the total path length through the SF_6 glass is about 4.6 cm. From these values, the final pulse compression factor, from expression 4.3, evaluates to 7.0.

The peak intensity in the SF_6 glass is restricted in value by a self-focusing limit. Transverse intensity variations in the laser beam will cause the SF_6 to exhibit lens-like behavior. If the propagation length through the SF_6 is long enough, or the peak intensity, I_p, is high enough, the beam will come to a focus and damage the glass. For collimated Gaussian beams, the whole beam self-focusing distance, D_f, is given by [88]

$$D_f = \frac{2\pi}{\lambda}\omega_s^2[\frac{P}{P_{cr}} - 1]^{-\frac{1}{2}} \tag{4.4}$$

where ω_s is the beam spot size and P is the optical power in the glass. P_{cr} is given by

$$P_{cr} = \frac{\lambda_0^2}{8\pi n_0 \gamma} \tag{4.5}$$

where λ_0 is the free space wavelength, $n_0 = 1.774$ is the refractive index of the SF_6 glass, and $\gamma = 21 \times 10^{-16}$ cm^2 W^{-1} is the nonlinear index of the glass in MKS units. For the above values and a 60 ps, 10 mJ optical pulse, the self-focusing distance is found to be about 4.5 cm, which is shorter than the length of the SF_6 glass.

The self-focusing distance was increased by placing the glass in the diverging region of the focused laser beam. For diverging beams with phase curvature R, the modified self-focusing distance, $D_f(R)$, can be obtained from the following expression [88].

$$D_f(R) = \frac{R \times D_f}{R - D_f} \tag{4.6}$$

The phase curvature radius of the expanding beam was estimated to be about 9.1 cm, which increased the self-focusing distance to about 8.9 cm, a distance sufficiently longer than the beam's path length through the SF_6 glass. This design was stable against power fluctuations by a factor of two.

The bandwidth broadening, or pulse chirping, stage is shown in figure 4.2. A double-pass arrangement has been employed. For each pass, the 8 mm diameter beam is focused and recollimated with a pair of 500 mm anti-reflection coated lenses. The SF_6 glass is placed about 80 mm from the minimum beam waist, and is mounted on one end of a small vacuum chamber. A 600 μm diameter pinhole is positioned at the minimum beam waist in the vacuum chamber. This pinhole spatially filters the focused laser beam which minimizes intensity ripple across the

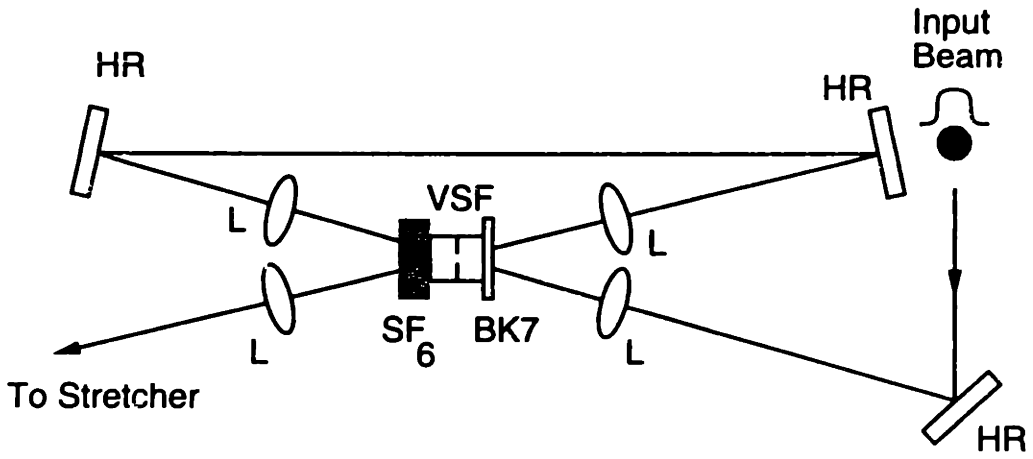

Figure 4.2: Double-pass pulse chirping stage. The amplified oscillator beam makes two passes through SF_6 glass as shown. Notations are lense, L, vacuum spatial filter, VSF, high reflector, HR.

beam in the SF_6 glass. A BK7 glass window is mounted on the other end of the vacuum chamber. Both the BK7 and the SF_6 glass are mounted at Brewster's angle to minimize reflection losses. Astigmatism, which results from the Brewster mounted optics, is cancelled by mounting the lenses at slight angles away from normal incidence [89].

4.3.2 Pulse Stretching and Compression with Gratings

Pulse stretching and pulse compression at optical frequencies is normally achieved with grating pairs [85, page 183], [87,90,?,92]. A pulse compressor and pulse stretcher are shown in figure 4.3. A simple grating pair normally acts as a negatively dispersive medium, because the higher frequencies travel a shorter distance through the assembly [85, page 186]. By inserting a lens pair between the gratings, the sign of the dispersion is flipped so that the assembly now exhibits normal dispersion [91,92].

The dispersion parameter, δ, for the compressor and stretcher is given by

$$| \delta | = d_{eff} \frac{\lambda^3}{2\pi c^2 \Lambda^2 \cos^2 \theta_r} \tag{4.7}$$

where Λ is the grating line spacing and θ_r is the diffraction angle from the grating. d_{eff} is the effective grating separation distance. For a simple pulse compressor, gratings without a lens

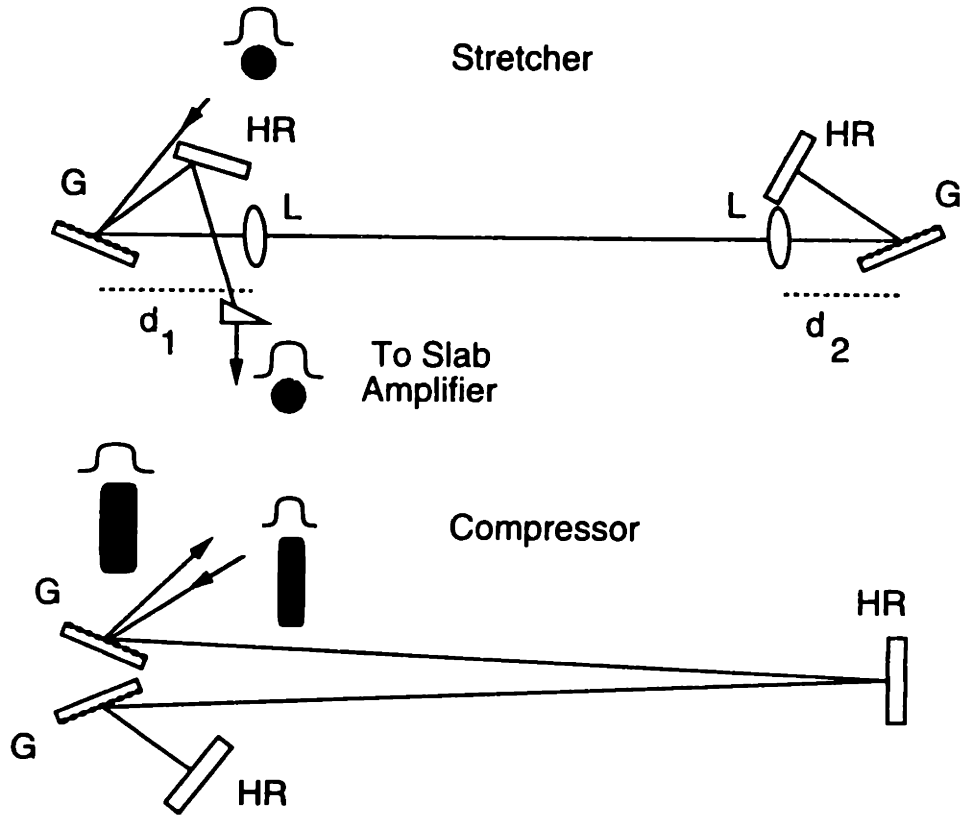

Figure 4.3: Pulse compressor and pulse stretcher. Grating pairs are used in double-pass arrangements to stretch and compress the optical pulses. For the stretcher, an identical lens pair is placed between the gratings as shown. Notations are lens, L, grating, G, distance, d.

pair, d_{eff} is just the measured grating separation. For a pulse stretcher with an identical lens pair between the gratings, the effective grating separation is given by [91]

$$d_{eff} = 2f - d_1 - d_2 \tag{4.8}$$

where f is the lens' focal length. d_1 and d_2 are the distances between the first(second) lens and the first(second) grating, as shown in figure 4.3.

The full width half maximum of the pulse, τ, after propagation through the grating pair assembly is given by [85, page 185]

$$\tau = 2\sqrt{\alpha_s \ln 2(1 + \frac{\delta^2}{\alpha_s^2})} \tag{4.9}$$

where α_s is related to the spectral bandwidth, $\Delta\nu$.

$$\Delta\nu = \sqrt{\frac{\ln 2}{\pi^2}\alpha_s} \tag{4.10}$$

In a properly designed CPA system, the increase in δ from the pulse chirping and pulse stretching stages is cancelled in the pulse compression stage.

Equation 4.7 indicates that the amount of compression or stretching can be increased by decreasing the grating line spacing Λ, or increasing the beam diffraction angle θ_r. However, there are physical and practical limits to these values. At small line spacing or diffraction angles near $\frac{\pi}{2}$, higher order dispersion becomes large, which will inhibit optimum pulse compression [93]. At large angles, the diffraction efficiency of the gratings decrease and the grating size must be increased to capture the incident beam. Also, the output beam will become astigmatic when the incident and diffracted angles are different [92]. These effects must be considered when designing the stretcher or compressor.

A pulse stretcher and pulse compressor, illustrated in figure 4.3, were used for CPA. The stretcher was developed by T. Savas. Both the stretcher and compressor were designed in a double-pass arrangement. Gold coated, pulse compression gratings, available from Spectragon U. S., Inc., were used in both stages. The gratings had a line density of 1800/mm.

For the stretcher, the gratings were separated by 3.4 m. Two 1.5 m, anti-reflection coated spherical lenses were used between the gratings to invert the dispersion. The first grating of the stretcher was 5 cm x 5 cm in size, and the second grating size was 3 cm x 11 cm.

The compressor gratings were placed 6.5 m apart, and three gratings were used. The "first grating" consisted of a stacked pair of 6.4 cm x 6.4 cm gratings. The input and output compres-

sor beams diffracted from the lower and upper gratings, respectively. Since the optical fluence was highest on the input grating, it would damage before the second grating. By using a grating pair at the input, replacement expenses would be minimized. The second compressor grating is a large area grating, 12 cm × 14 cm. The compressor was folded with a mirror between the two gratings so that it would fit on an optical table.

Alignment of the compressor and stretcher was carried out with both a He-Ne laser and the master oscillator. The He-Ne laser was used to center the gratings on the optical beam path, and to set the approximate grating angles. The master oscillator was used for final angle adjustment. The stretcher was designed to lengthen the chirped pulse to 120 ps, and the compressor was designed for a final pulse duration of 20 ps.

The compressor was optimized to achieve the shortest pulse. This was a somewhat tedious task, since gratings had to be moved and angles readjusted. Four combinations of grating angles and separations were tested. The shortest pulse length was observed with a 6.5 m grating separation and a diffracted angle, θ_r, of 73 degrees.

4.3.3 Four-Pass Amplification

The high power, zig-zag slab amplifier was designed and built by M. Muendel [77], and originally configured for three-pass amplification with one or two beams. In this configuration, one pass was made through the amplifier with a small, 8 mm × 8 mm, beam and two passes were made with a large, 50 mm × 8 mm, beam. Because of optical losses in the pulse chirping, pulse stretching and pulse compression stages, the slab amplifier was configured for four-pass operation. An additional pass was made with the small beam as shown in figure 4.4.

For high power amplifiers, self-focusing may occur within the amplifier, if designed improperly. The tendency to self-focus is indicated by the B integral, which is a measure of the accumulated nonlinear phase shift across the beam profile [86, page 386]. The value of the B integral should be below 3 for optical systems. The B integral was checked, for the four-pass arrangement and input beam profile from the pulse stretcher, with a commercial optical propagation program *Fresnel* [94]. The value of the B integral was found to be less than 0.5. To minimize beam propagation effects, the distances were minimized and the relayed image from the preceding vacuum spatial filter assembly was located at the beginning of the third pass. Beam expansion was performed before the third pass.

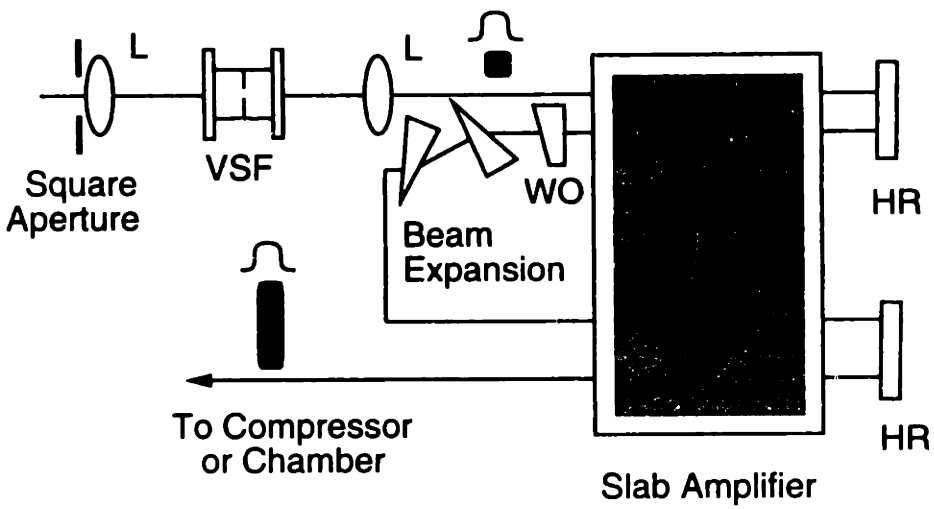

Figure 4.4: Four-pass amplification. An additional pass through the slab amplifier was made with the small beam, so that losses from the CPA stages could be recovered. The first and second, and third and fourth passes were down-and-back: the beam was reflected off a mirror at normal incidence on the right side of the slab. The small beam was expanded to an 8 mm x 50 mm size after the second pass. A wedged optic, WO, was placed after the second pass to allow minor beam steering before the last two passes.

Table 4.1: Measured Four-pass Gain Values

Lamp Dial Setting	Measured Gain
4.72	17
5.61	51
6.07	83
6.38	118
6.61	163
6.94	255
7.18	354

Alignment tolerances were found to be small for the four-pass arrangement shown in figure 4.4. The narrow tolerances were due to the down-and-back nature of all passes, and the narrow slab, 10 mm width. To facilitate alignment, an anti-reflection coated, wedged optic was used after the second pass to decouple the second and third passes. This allowed lateral separation of the entrance and exit beams for the first and second passes, and the third and fourth passes.

After alignment of the amplifier was completed, four-pass gain measurements were made with a diode and calibrated energy meter. The diode was placed before the slab amplifier, and was used to discriminate against energy fluctuations in the master oscillator/amplifier. An energy meter was placed after the amplifier and monitored the amplified signal. A portion of the amplified beam was reflected to the energy meter and neutral density filters were used to attenuate the amplified signal. Measured four-pass gain values are reported in table 4.1 for several flashlamp current dial settings. The measured values were based on a three shot average.

4.3.4 System Performance

The performance of the pump-laser and CPA system was evaluated. Stretched and compressed pulses were measured. Energy losses of the CPA stages were determined, and output energy was estimated with a calibrated diode for the different pulse lengths. Output beam quality was evaluated, and system stability was assessed.

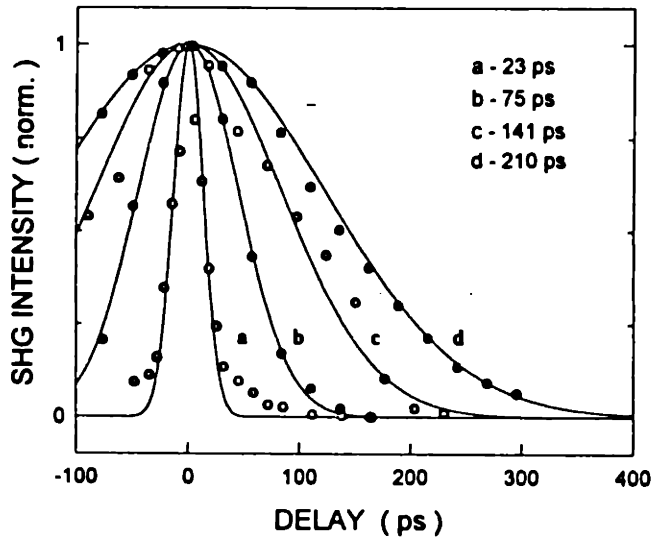

Figure 4.5: SHG pulse autocorrelations. The oscillator pulse, **a**, stretched pulse, **b**, and compressed pulse, **c** lengths were measured with a second harmonic autocorrelator. The etalon lengthened pulse, **d**, was also measured. These four pulse lengths were used to excite the EUV lasant plasma in later experiments.

To measure pulse lengths, a crossed-beam second harmonic autocorrelator was assembled. Long arms were used in the autocorrelator so that nearly collinear, interferometric electric field correlations could be made without the frequency doubling crystal. Because of the long pulse lengths, a four-bounce variable delay was used in one arm of the autocorrelator. A reference diode was used in autocorrelation measurements to discriminate against oscillator energy fluctuations. Autocorrelations were averaged over at least three shots.

Second harmonic autocorrelations of the oscillator pulse, stretched pulse and compressed pulse are shown in figure 4.5. The respective pulse lengths were found to be 75 ps, 141 ps and 23 ps. For the compressed pulse measurement, the pulse length was measured for the center of the laser beam, and for the whole beam. Intensity variations across the beam may result in pulse length variations across the beam. The difference between the beam center and whole beam measurements was negligible. The compressed pulse has long wings, which indicate uncompensated higher order dispersion. A comparison of the second harmonic and electric field autocorrelations, measured after the SF_6 glass, indicated that the bandwidth broadened pulse was about 3.3 times the transform limit. This indicates that the compressed pulse is nearly

Table 4.2: CPA Stage Losses

CPA Stage	Loss (%)
Chirping	4
Stretcher	35
VSF & Slab Amplifier	48
Compressor	28

transform limited.

The pulse compression factor $\frac{\tau_0}{\tau}$, measured to be about 3.3, is slightly more than one-half the value predicted from equation 4.3, using a 75 ps initial pulse width. The discrepancy may be due to a larger than expected beam radius in the SF_6 glass for the second pass, or for both passes. Notwithstanding, the 23 ps compressed pulse was short enough for initial plasma heating experiments.

Also shown in figure 4.5 is an autocorrelation of the etalon-lengthened pulse. To generate this pulse, a 4 mm thick uncoated fused silica etalon was placed in the oscillator cavity and the RF power to the mode-locker was reduced from 9.0 Watts to about 4.3 Watts. The cavity length was shortened to cancel the added path length due to the etalon, and the pulse chirping, pulse stretching and pulse compression stages were by-passed. The measured pulse length was about 210 ps. The four pulse lengths shown in figure 4.5 were used to excite the lasant plasma in several experiments which will be described in chapter 6.

Shortly after these pulse length measurements, the oscillator was rebuilt and the oscillator pulse was measured to be 56 ps, which should result in a 15 ps compressed pulse. However, results of plasma heating experiments suggested that long pulse operation was preferred, and the system was not configured for short pulse operation again.

Energy losses and output energies for the CPA system were measured with a calibrated energy meter and a calibrated diode. Energy losses for the various CPA stages are listed in table 4.2. The losses in the pulse stretcher and pulse compressor are primarily determined by the grating diffraction efficiencies. Since both grating pairs are double-passed, there are a total of 16 grating diffractions in the CPA system. Unfortunately, the largest grating in the compressor

Table 4.3: Measured Pulse Energies

Pulse Length (ps)	**Energy** (J)
23	0.8
75	1.2
141	2.0
210	3.0

had the lowest efficiency, about 90 %, whereas all other gratings had efficiencies over 95 %.

The estimated output energies, with the pump-laser configured to produce each of the four pulses shown in figure 4.5, are listed in table 4.3. Energies listed are energies delivered to the vacuum chamber and EUV lasant target. The short pulse energy is limited by the fluence on the first grating of the pulse compressor, which was specified to be at least 100 mJ cm^{-2} [95]. Optical damage was observed on this grating at a fluence of 120 mJ cm^{-2}. Interchanging the pulse compressor gratings and doubling the beam width before the compressor would allow the 23 ps pulse energy to be doubled to 1.6 J. All other pulse lengths were limited by the slab amplifier's intensity limit.

Two measurements were made to determine the quality of the output beam from the pump-laser and CPA system [96]. The beam's transverse intensity profile was measured with a linear CCD diode array. A sample profile, measured at high energy, is shown in figure 4.6. Because of the long propagation distance in the stretcher, the output beam had a $\sim$ 20% depression at its center.

The minimum waist of the focused pump-laser beam was also measured. A 37 μm wide slit was scanned across the focused beam, and a diode was used to measure the transmitted energy. High and low energy measurements were made with negligible difference noted between the two measurements. In another measurement, the CPA system was by-passed and the resulting beam waist was also nearly identical to the other measured waists. The data is shown in figure 4.7. A program, CONV1, was written to simulate the slit and beam waist convolution, so that the actual beam waist could be determined. A fit to the data is shown in the figure. The measured minimum beam waist was determined to be about 40 μm at full width half maximum.

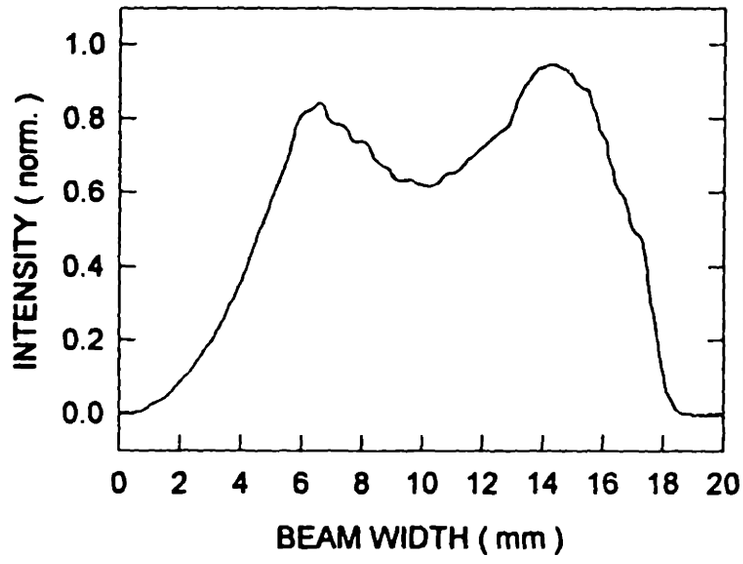

Figure 4.6: Transverse intensity profile of the pump-laser beam. The transverse beam profile was observed to have an intensity depression at its center, due to the 6.5 m propagation distance in the pulse compressor.

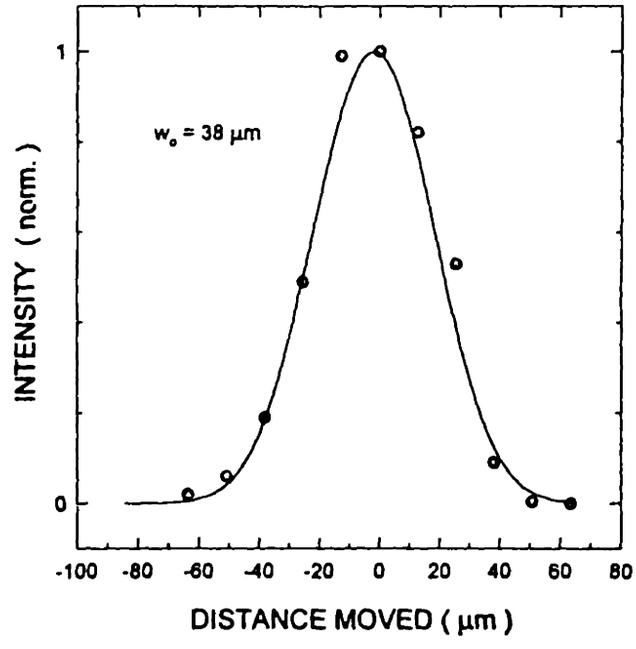

Figure 4.7: Minimum beam waist. The minimum beam waist was measured by scanning a slit across the focused beam.

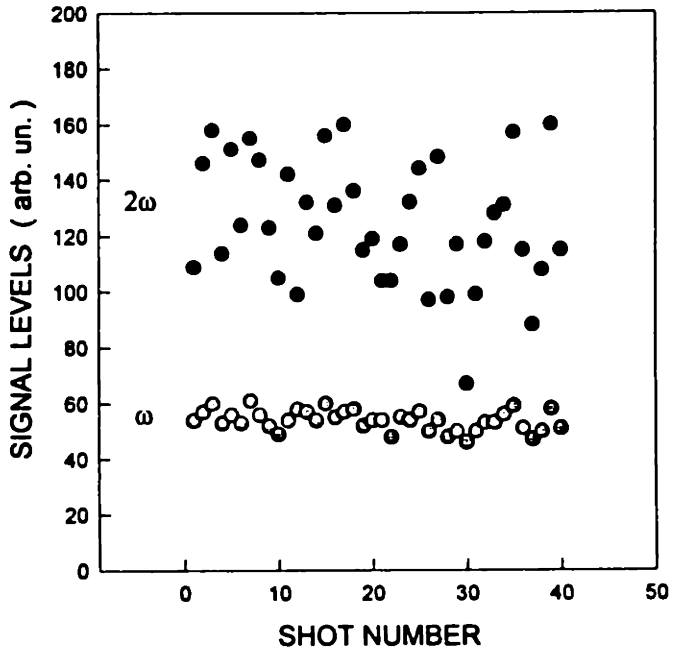

Figure 4.8: System stability. The fundamental, ω, and second harmonic, 2ω, signals showed pulse energy stability within ± 12 %, and pulse length stability within ± 6 %.

The system stability was determined by simultaneously measuring the fundamental and second harmonic pulse energies for forty consecutive laser shots. Alignment of the system was optimized before data was recorded. The second harmonic signal was obtained from the autocorrelator with no differential delay, so that the pulses were maximally overlapped in the frequency doubling crystal. After acquiring 20 data points, the pump-laser was not fired for 30 minutes. Then, the final twenty shots were taken without any adjustments made to the system. The data is shown in figure 4.8, and indicates that the pulse energy fluctuations were less than ± 12 % and the pulse length variations were less than ± 6 %. The measured stability was adequate for subsequent experiments.

4.4 The EUV Amplifier Target Chamber

The high vacuum target chamber was designed by Dr. S. Basu, and was constructed by Huntington Laboratories, Inc. The chamber size was designed to be large, 260 liter volume, to that EUV laser cavity experiments could be performed once EUV gain was detected. A sketch of the chamber is shown in figure 4.9. The chamber houses both axial short wavelength spectrometers, which will be described in the next section, and the EUV lasant target assembly.

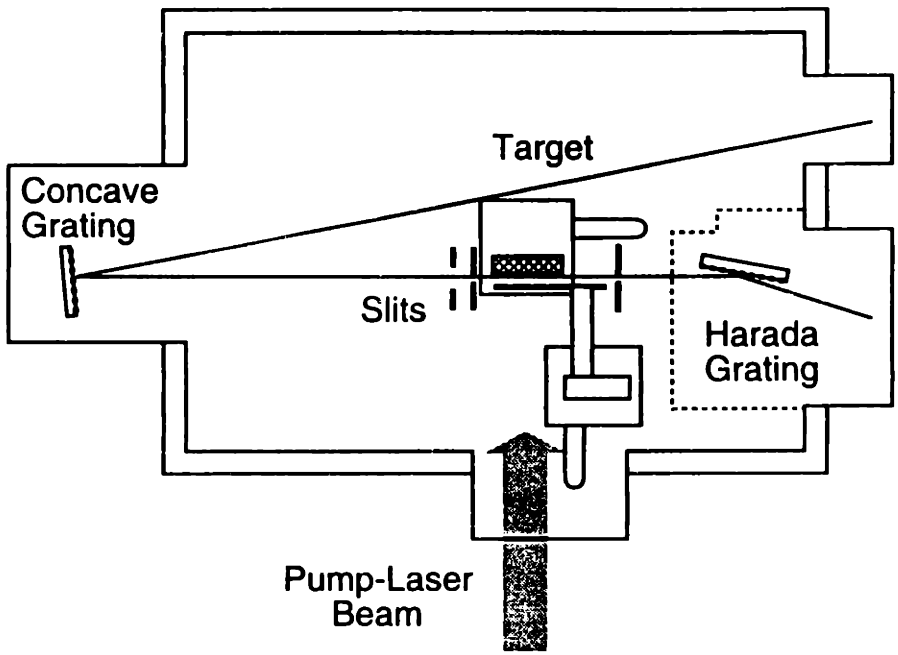

Figure 4.9: The EUV target chamber. A high vacuum chamber, designed by Dr. Basu, was used to house the lasant target and two axial, short wavelength spectrometers.

The target was mounted on a five-axis, remote positioning assembly developed by Dr. Basu and Dr. S. Kaushik. This assembly allowed fine adjustment of target alignment in vacuum, and allowed for translation of the target between pump-laser shots. The target was translated between shots to renew the surface of the lasant target. Two fixed slits were mounted on either side of the target, and were the input slits to the spectrometers.

For most recombination lasant studies, a blade assembly was mounted near the target. A spring mounted steel blade was mounted against the target surface as shown in figure 4.10. The springs kept the blade against the target surface as the target was moved. The blade was located about 50 μm above the pump-laser line focus, and the lower edge was beveled at an angle as shown. The distance between the lower blade edge and the target surface was varied from 150 μm to 700 μm. The optimum distance was found to be about 500 μm for H-like B.

Two vacuum pumps were used to evacuate the chamber. A mechanical pump, model SD-450 from Varian Associates, was used to rough out the chamber. High vacuum, about 10^{-6} Torr, was achieved with a turbomolecular pump, model Turbo-V450 also supplied by Varian. The total pumping time was about 45 minutes to achieve high vacuum. The high vacuum is necessary for operation of high voltage microchannel plates used in the spectrometers.

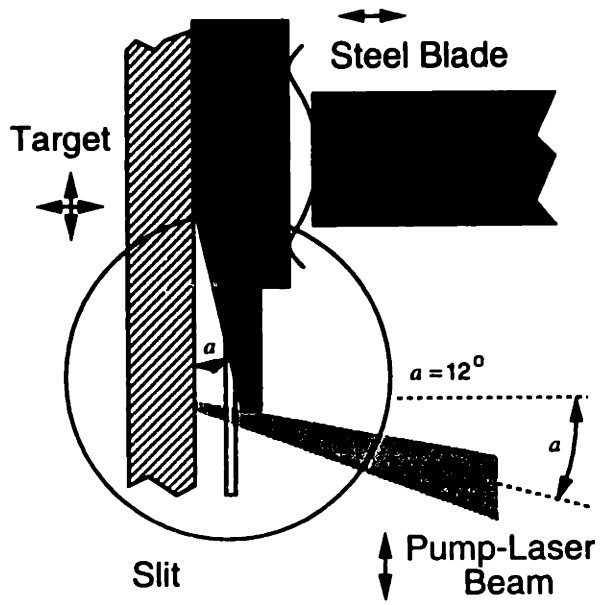

Figure 4.10: Blade assembly. For recombination studies, a steel blade was mounted near the target to increase the plasma cooling rate.

4.5 Short Wavelength Spectrometers

Emission from the lasant plasma was studied with two short wavelength spectrometers. Shorter wavelength emission was monitored on-axis with the time integrating flat-field spectrometer (TIFFS). Candidate lasing lines were detected on-axis with the streaked or imaging concave grating spectrometer (S/ICGS). Both spectrometers are described in this section.

4.5.1 The TIFFS

The time integrating flat field spectrometer is pictured in figure 4.11. This spectrometer is primarily used to detect short wavelength emission, 3 nm - 11 nm, pertinent to lasant ionization studies. The spectrometer consists of a 50 μm entrance slit, located 1.5 cm from the end of the lasant plasma, a Harada grating, and a vacuum insert, which holds the recording film. The Harada grating is a gold coated, spherically concave grating which focuses spectral emission, in one dimension, onto a flat field located 239 mm from the center of the grating [97]. The line density of the Harada grating is 1200/mm. The incident angle, θ_i, is fixed at 87.0 degrees, and the diffracted angle, θ_r, for a spectral line is determined by the standard grating formula.

$$\sin\theta_i + \sin\theta_r = m\frac{\lambda}{\Lambda} \tag{4.11}$$

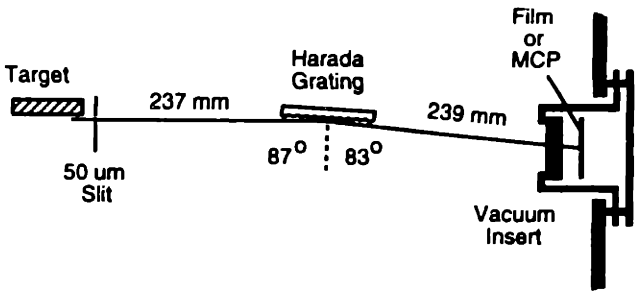

Figure 4.11: The time integrating flat-field spectrometer (TIFFS). The TIFFS consists of a slit, Harada grating and vacuum insert, which holds film or a microchannel plate, MCP, at the focal plane of the grating.

Λ is the grating line spacing, and m is the diffraction order.

A vacuum insert was designed to hold either photographic film or a microchannel plate (MCP) at the focal plane of the Harada grating. The insert allows film to be exchange without venting the large vacuum chamber, and decreased data acquisition time from 40 minutes to 2 minutes per photo. For all recent measurements reported in this study, Polaroid 107 film was used to record spectral data. With this film, the spectral range of the TIFFS extended from about 3 nm to 11 nm, although wavelengths below 4 nm were poorly focused [97]. The wavelength response was primarily determined by carbon in the film, which has a transmission window between 4 nm and 20 nm [98]. Two separate spectra can be recorded on a single photo.

In an alternate configuration, the wavelength response of the TIFFS may be extended to 50 nm by placing a microchannel plate at the image plane and using filters to attenuate the short wavelength emission. For this arrangement, the spectral image on the MCP must be optically relayed out of the vacuum insert, as is described for the S/ICGS in the next subsection. This will reduce the data acquisition time to the pump-laser firing rate, and allow simultaneous observation of the lasing line with both spectrometers.

Sample data from the TIFFS is shown in figure 4.12. Both the raw data, digitally inverted for clarity, and a densitometer trace of the film are shown. Wavelengths are identified from the film by measuring the distance from the 0-order signal, d_0. The distance, in millimeters, for a

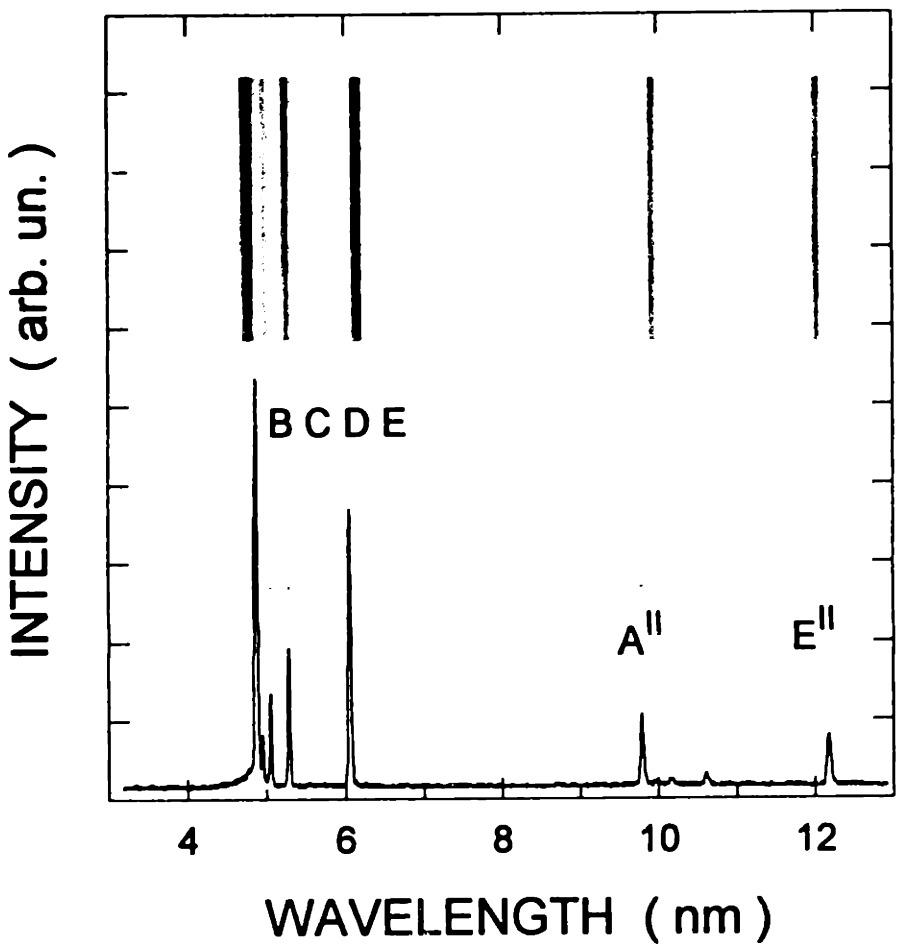

Figure 4.12: Spectral data recorded with the TIFFS. Short wavelength spectra from the TIFFS is recorded on Polaroid 107 film. A densitometer is used to obtain a spectral line-out of the film.

particular wavelength is given by

$$d_0 = \frac{239}{\tan\theta_r} - 12.3 \tag{4.12}$$

where θ_r is the diffracted angle determined by equation 4.11. The program HARADA has been written to determine line positions for m orders, or identify wavelengths from measured distances.

The TIFFS was calibrated with B and C targets, for which spectra was simple and transition wavelengths well known. The sample data shown in figure 4.12 was obtained from a B plasma. Dominant lines are from H-like and He-like B [28,31,99]. The first order spectral line-out in figure 4.12, obtained with a custom densitometer, shows that the H-like B 2p-1s line at 4.86 nm and the He-like B 5p-1s line at 4.94 nm are well resolved. This gives a spectral resolution better than $\frac{\lambda}{\Delta\lambda} \approx 60$ at 5 nm in first order. Slightly better resolution can be obtained by examining the film with a microscope. The highest resolution obtained with a microscope was $\frac{\lambda}{\Delta\lambda} \approx 150$ at 8 nm.

The intensity response of the TIFFS, with film, is determined by the Polaroid 107 film response. The intensity response was determined by taking a series of spectra, for which the optical dose was doubled for each successive photo. Peak intensity values of spectral lines, measured with the densitometer, are plotted in figure 4.13. The data shows that the intensity response is linear over a limited range, about a factor of 4. Beyond this range, saturation corrections must be made to obtain correct intensity values.

4.5.2 The S/ICGS

The streaked or imaging concave grating spectrometer is illustrated in figure 4.14. This spectrometer is primarily used to detect long wavelengths, 20 nm - 40 nm, pertinent to EUV amplification studies. The S/ICGS consists of a slit pair at its input, a 3.0 cm x 3.2 cm ruled concave grating with a 1 m radius of curvature, and detection apparatus. The grating line density is 3600/mm. The concave grating has been loaned to us by Uri Feldman at the Naval Research Laboratories. For high resolution measurements, a 1.8 cm diameter aperture is placed over the grating. The grating is on a rotation and tilt stage, which may be adjusted with feed-thru micrometers outside the vacuum chamber. Because the detection window is limited to about 2.5 nm, the grating must be rotated to access the full wavelength range. A He-Ne laser, reflected from the back side of the grating, is used to position the grating for observation of a particular

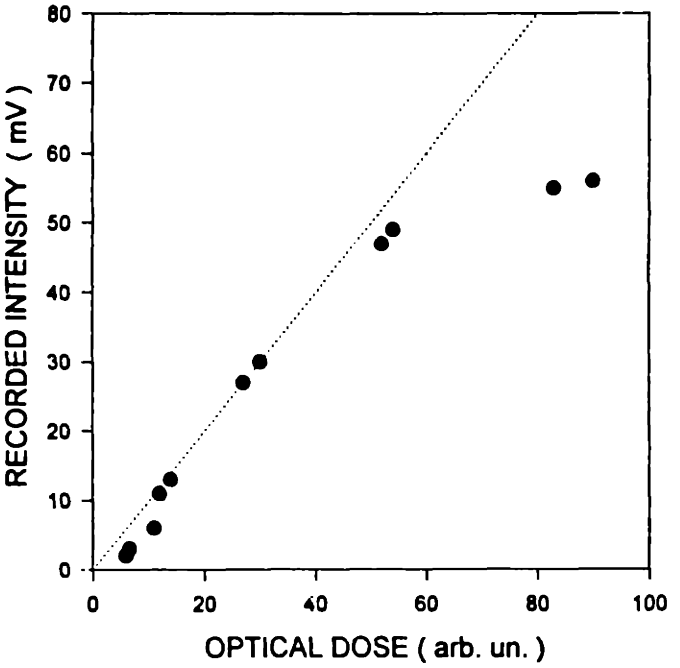

Figure 4.13: TIFFS intensity response. The intensity response of the TIFFS is determined by the Polaroid 107 film response, and is linear over a small range.

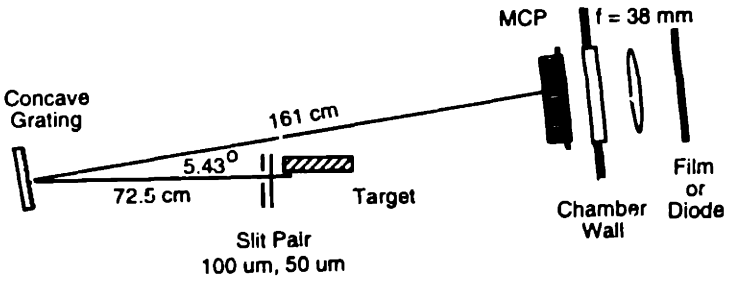

Figure 4.14: The streaked or imaging concave grating spectrometer (S/ICGS). The S/ICGS consists of an input slit pair, a 1 m radius, concave 3600 l/mm grating, and detection apparatus. In imaging mode, a microchannel plate, MCP, is placed at the image plane of the grating as shown. In streaked mode, a streak camera is used instead of the detection apparatus shown.

wavelength.

The detection apparatus used depends upon the operation mode of the spectrometer. There are two modes of operation: imaging mode and streaked mode. Imaging mode has been used for most of the data reported in this work.

In imaging mode, the spectrometer gives a time integrated, spectrally resolved image of the plasma. Different regions of the plasma are selected for viewing with the input slit pair. The plasma is imaged onto a microchannel plate, with a phosphor screen backing, inside the chamber as shown. The gain of the MCP can be easily adjusted externally with a variable high voltage supply. The image on the phosphor screen is optically relayed, through a view port, to an image plane outside the chamber. Total magnification of the spectrometer and optical relay is 3.0. Either instant film, Polaroid 667, or a photo diode can be placed at the image plane to observe spectral emission. With film, all lines within the 2.5 nm window can be recorded, and up to eight separate spectra may be recorded on a single photo. With a diode, only spatially integrated intensity of a single line can be recorded. However, diode detection is ideally suited for amplification analysis since it avoids film saturation problems.

In streaked mode, the spectrometer gives temporally resolved spectra, with about 50 ps resolution. To operate the spectrometer in streaked mode, the vacuum chamber must be vented and the imaging apparatus removed so that a streak camera, on loan from Mike Campbell at the Lawrence Livermore National Laboratories, can be located at the spectrometer's image plane. With the streak camera, only one spectral trace can be recorded per photo. The streak camera has been used for initial gain studies [1,2], but subsequently has been found to have substantial gain fluctuations. The gain of the streak camera cannot be controlled externally. Until repaired, the streak camera is unreliable for EUV amplification studies.

Since the target location and detection plane are fixed, wavelength identification is more difficult with the S/ICGS than with the TIFFS. For a chosen wavelength, λ, the grating incident angle, θ_i can be determined from a simultaneous solution of

$$\theta_i + \theta_r = 5.43^\circ \tag{4.13}$$

and the grating equation 4.11. Since the grating is used near normal incidence and has a high line density, short wavelengths are strongly attenuated and only first order diffractions are observed in the wavelength range. Two programs, NRL1 and NRL2 have been written to facilitate line identification with the S/ICGS.

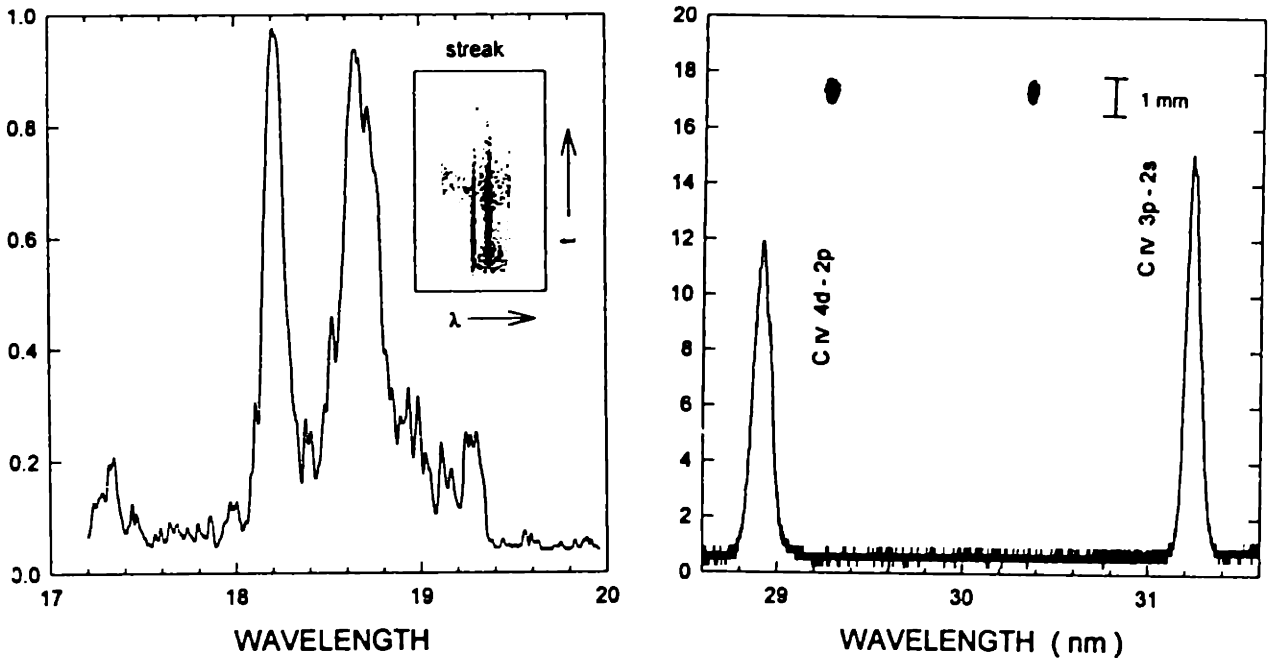

Figure 4.15: Spectral data recorded with the S/ICGS. Streaked, left, and imaged, right, raw data from the S/ICGS are shown, along with densitometer traces.

Spectrometer resolution and calibration measurements were made using C and B plasmas as was done for the TIFFS. Sample data from the S/ICGS is shown in figure 4.15, along with densitometer line-outs. For high resolution spectroscopy, the grating aperture was used, and the slit widths were reduced to 25 μm and 50 μm. The highest resolution obtained, using a microscope to examine the film, was $\frac{\lambda}{\Delta\lambda} \approx 700$ at 25 nm. Because of the low signal level, the slit widths were increased to 50 μm and 100 μm and the resolution was found to be 400 at 40 nm.

Since the grating had to be rotated to observe different wavelengths, accurate wavelength identification could only be achieved by recalibrating the spectrometer after each grating rotation. Without recalibration, the repositioning error of the grating location resulted in a wavelength uncertainty of ± 0.06 nm. For precise line identification, a C or B slab was attached to the lasant target to serve as a calibration source. By comparing the candidate lasant spectrum with the calibration spectrum, wavelengths could be determined to within ± 0.02 nm.

The intensity response for the S/ICGS, in imaging mode, was determined with a procedure

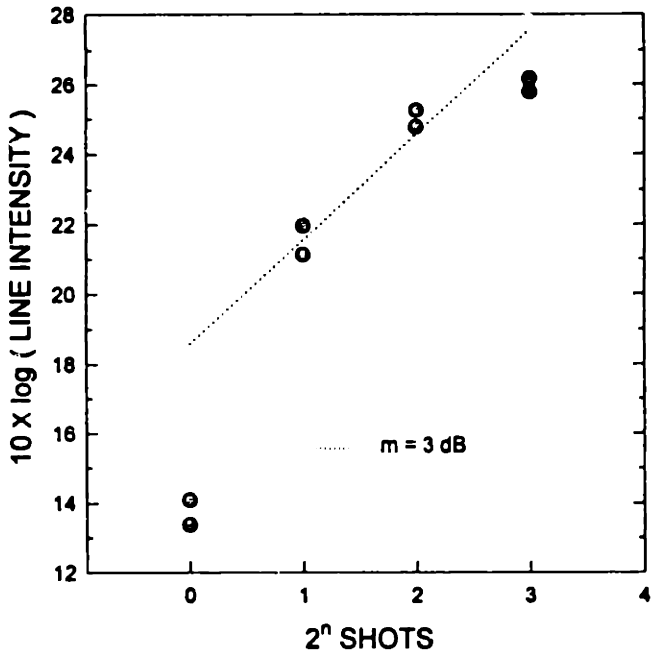

Figure 4.16: Intensity response of the S/ICGS. The intensity response of the S/ICGS is limited by the Polaroid 667 film and the MCP assembly.

similar to that used for the TIFFS. The intensity response in streaked mode has not been determined. In imaging mode, the intensity response is determined by the film and the MCP responses. The measured intensity response is shown in figure 4.16, and indicates a linear range less than a factor of 2.

In both of the spectrometer intensity response measurements figures 4.13 and 4.16, a low intensity roll-off is observed. This low intensity nonlinearity was not properly accounted for in the H-like B gain measurement reported previously [2]. Because of this nonlinearity and the failure to reproduce the previous gain results with a more accurate gain measurement technique, which will be described in chapter 5, the earlier reported gain results in H-like B are believed to be in error.

The change in MCP assembly gain as a function of applied high voltage was also measured. For this measurement, an optical diode was placed at the image plane and monitored the intensity of a single spectral line. The measured value was found to be $\frac{\Delta G}{\Delta V} \approx 27$ dB kV^{-1}, and was linear over an order of magnitude. The data is shown in figure 4.17. The measured value of $\frac{\Delta G}{\Delta V}$ was found to agree with the manufacturer's specification of $\frac{\Delta G}{\Delta V} \approx 25$ dB kV^{-1} [100].

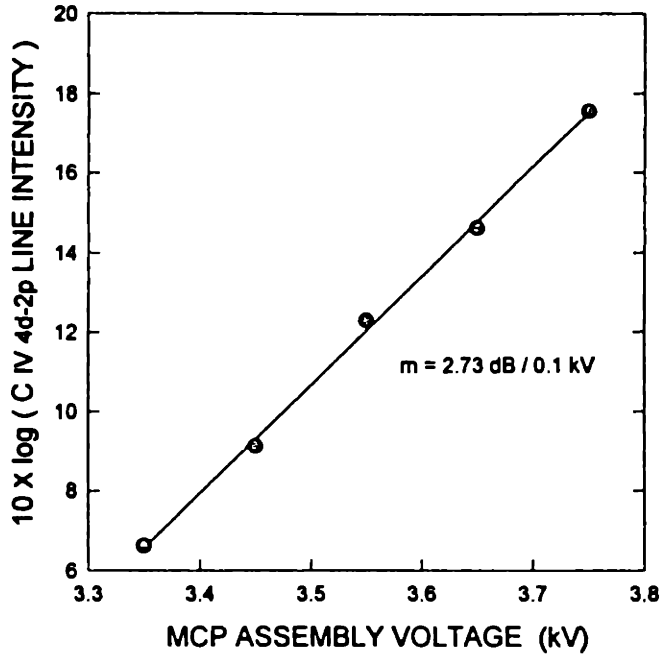

Figure 4.17: S/ICGS gain response. The variation in gain of the S/ICGS's MCP assembly was measured as a function of applied high voltage.

4.5.3 Spectral Readout with a Densitometer

Most spectral data reported in this study was recorded on Polaroid film. A densitometer was constructed to digitize data from the photos. This was necessary to obtain consistent intensity values for recorded spectral lines.

For initial gain studies [1,2], photos were digitized with optical scanners or video systems. It was later found that the scanner and video systems had internal automatic intensity and contrast adjustment features, so that accurate line intensity values could only be determined with a reference for each photo. This problem was circumvented by using the densitometer.

To obtain spectral traces with the densitometer, a focused He-Ne beam is scattered off the photos, and part of the scattered signal is collected with a photodiode. The film is mechanically scanned to obtain the complete spectrum. The film position and diode voltage are fed directly to a computer. A data acquisition program, DENSI, was written to collect data from the densitometer.

4.6 Spectrometer and Plasma Alignment

The acceptance angles of the TIFFS and S/ICGS are 11 mrad and 25 mrad, respectively. The plasma axis must be aligned to the spectrometers carefully, so that the amplified EUV signal may be detected. The alignment procedures for the spectrometers and plasma are described in this section.

The optical axis of the spectrometers and plasma was determined with a He-Ne laser. This axis was made level, to within .3 mrad, by using a long tubing and liquid. The axis was made normal to the pump-laser beam, to within ± 1 mrad, by using a right angle prism placed at the location of the target. The spectrometer gratings and slits were then centered on the optical axis defined by the He-Ne laser.

The alignment He-Ne laser is located outside the chamber, behind the concave grating used in the S/ICGS. The grating may be rotated so that the beam passes through the chamber, along the optic axis. The same He-Ne laser is also used to position the S/ICGS grating to observe a particular EUV wavelength.

The S/ICGS, used in imaging mode, was then used to align the plasma axis to the optical axis defined by the He-Ne laser. This was accomplished using parallax. The plasma was lengthened with a cylindrical lens, and point images detected from each end of the plasma, with the S/ICGS, were overlapped by rotating the target about a vertical axis and rotating the final cylindrical focusing lens pair about a horizontal axis. Using this procedure, the plasma axis could be aligned to the spectrometer axes to within ± 3 mrad. Since the beam divergence of the amplified signal was expected to be greater than 15 mrad, see figure 3.9 of chapter 3, the spectrometer and plasma alignment method described here assured detection of the amplified beam.

4.7 Multiple Pump-laser Beam Alignment

In some experiments, described later, two pump-laser beams were used to excite the lasant plasma. Since the focal width of the pump-laser beams were about 40μm, figure 4.7, careful alignment was required to overlap the beams. Again, the S/ICGS was used in imaging mode to assure beam overlap.

Short wavelength emission originated from a region of the plasma, which was typically $< 200\mu$m wide in the transverse direction, parallel to the target surface. The spectral im-

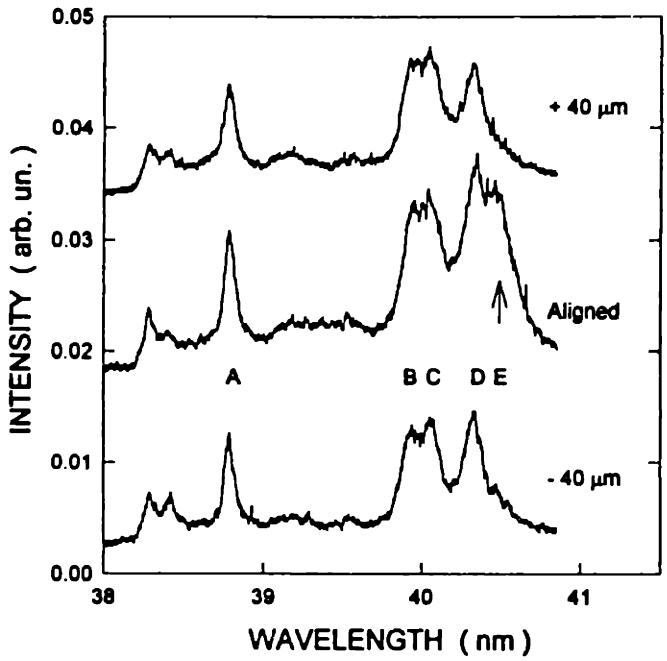

Figure 4.18: Alignment of multiple pump-laser beams. While aligning multiple pump-laser beams, spectra from the S/ICGS were monitored to determine the hottest plasma.

ages, created by each pump-laser beam, were monitored with the S/ICGS while one pump-laser beam was steered with a differential mirror mount. The minimum translation increment of the pump-laser beam was estimated to be about 20μm. Separate plasmas were observed when the beams were not overlapped, and an increase in line intensity was observed when the beams were overlapped. This technique was used to align multiple transverse pump-laser beams.

Sample data for this alignment procedure is shown in figure 4.18 for a Mg plasma. The figure shows three spectral traces. For the top and bottom traces, the two transverse pump-laser beams have been displaced by about 40 μm. When the two pump-laser beams are overlapped, or aligned, there is an increase in line intensities by about 30 %. What is most noticeable though, is the appearance of the spectral line, marked E, in the center trace. This line corresponds to the Li-like Mg 5g-4f transition. The other lines are N-like Mg 2p-2s transitions [61]. The ionization potential for N-like Mg is 186 eV and the ionization potential for Li-like Mg is much higher, 367 eV. The appearance of the Li-like Mg 5g-4f line clearly shows that the two pump-laser beams have been aligned.

For transverse and longitudinal pump-laser beams, a similar alignment technique was used. However, the longitudinal pump-laser beam was first aligned to the optical axis using the He-

Ne laser. The transverse beam was then scanned so that the plasmas created by each beam were overlapped. Other data, presented in chapter 6, also indicated that the two beams were adequately aligned.

Chapter 5

Constant Dose Gain Measurement Technique

5.1 Introduction

The goal of this work is to demonstrate a gain-length product, αL, larger than 5 at wavelengths below 40 nm. The S/ICGS is primarily used to identify lasing lines and to detect the presence of gain. Understanding the gain measurement technique is critically important to determine whether the goal of these experiments have been achieved.

During this study, a new technique for measuring extreme ultraviolet gain was developed [101]. This "constant dose" technique is well suited for low power, short wavelength systems for which the signal level is low, the expected gain-length product is low, and film is used to record plasma emission. The method will be described in this chapter, and the minimum detectable gain, using this technique, will be estimated for our experiments.

More accurate measurements of gain could be achieved using electronic detection only. Such gain detection apparatus might be a two-dimensional EUV diode array, or a phosphor-backed microchannel plate, which is fiber optically coupled to a 2-D optical diode array. However, these detectors are expensive, > $ 16,000, and repair or replacement costs would be high if the apparatus were damaged. When more funds become available, our apparatus might be upgraded to include one of these electronic detectors.

For our experiments, all spectral data has been recorded on instant film, as described in chapter 4. Film provides a sensitive, inexpensive, fast, 2-D permanent visual record of spectral emission. Presently, the cost per photo is about $ 1. The TIFFS records two spectra per photo, and the S/ICGS records five to eight spectra per photo in imaging mode, which reduces the cost

per spectra. In streaked mode, the S/ICGS records one spectrum per photo. The disadvantage of instant film is its small dynamic range [5, page 87], and see figures 4.13 and 4.16. To measure a gain-length product of 5, the detection apparatus must have a dynamic range of at least 40, which is well beyond the range of the films described in chapter 4. (At such large gain values a photodiode, rather than film, would be used to measure gain as described in subsection **4.5.2** of chapter 4.) The gain measurement technique described in this chapter avoids the problems associated with film nonlinearity.

The constant dose technique is not restricted to gain measurements. It may also be useful for absorption and line intensity ratio measurements. The constant dose measurement technique may also be applied to both spectrometers used with our EUV system. In this chapter, the description of the constant dose method will be limited to the S/ICGS, since this instrument is primarily used to detect gain in our experiments.

5.2 Description of the Technique

Once the candidate "lasing line" has been identified, gain measurements are normally made by measuring the intensity of the lasing line as a function of plasma length, an I *vs.* L measurement. The plasma length is varied by changing the width of the pump-laser beam. For our measurements, parts of the pump-laser beam are blocked. The intensity of the lasing line is expected to grow according to the Linford formula [81], or a modified version, as described in section **3.6** of chapter 3. The growth is nearly exponential.

To avoid problems associated with film nonlinearity, an I *vs.* L measurement should be made by maintaining constant optical dose on the film for each plasma length. This may be done in several ways. One way is to vary the number of exposures for each plasma length as illustrated in figure 5.1. Another way is to vary the gain of the microchannel plate used to convert the EUV image to a visible image in the S/ICGS. These two procedures have been used for our measurements. Also, EUV filters may be used to maintain constant dose as plasma length is varied, although this method is more cumbersome. When making constant dose measurements, the chosen dose must be in the film's linear range for best results.

As an example of the first procedure, consider the case of an optically thin line, $\alpha L << 1$. The intensity of this line is expected to grow linearly with plasma length. To measure this, one would first record the intensity of the line for the full plasma length with one pump-laser

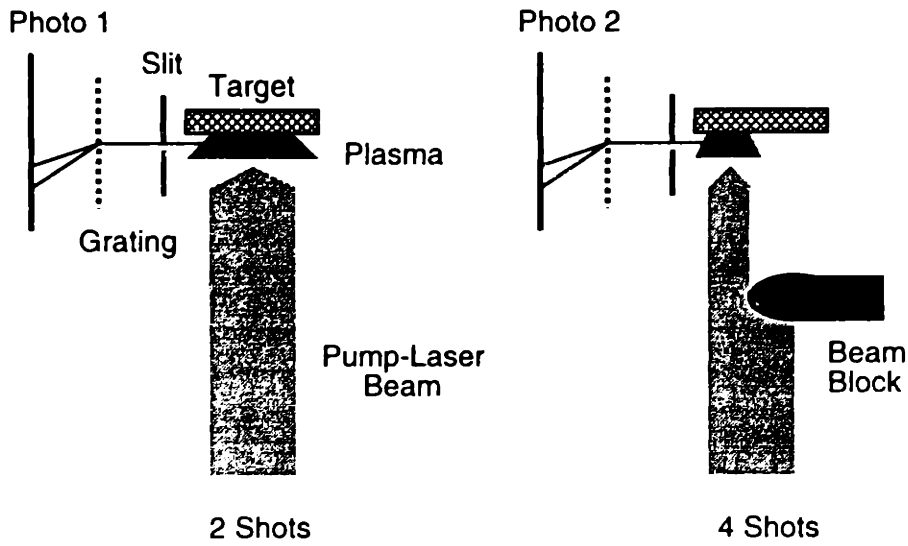

Figure 5.1: Constant dose, I *vs.* L measurement. As the plasma length is shortened, the number of exposures, or pump-laser shots, is increased to maintain constant dose on the spectrometer film. This technique, used to determine the presence of EUV amplification, avoids problems associated with the film's limited dynamic range.

shot. Half the pump-laser beam would then be blocked, and the intensity recorded with two pump-laser shots, a double exposure. Intensities for other plasma lengths would be recorded accordingly.

The second procedure for maintaining constant dose is to vary the gain of the MCP in the S/ICGS, see figure 4.14, for each plasma length. The change in MCP gain due to a change in applied high voltage was measured to be 2.73 dB kV$-$1, see figure 4.17. As the plasma length is reduced, the gain of the MCP can be increased accordingly to maintain constant optical dose.

The results of these two procedures should be the same. For an optically thin line, all recorded intensities for each plasma length should be identical to within system fluctuations. Dividing the recorded intensity by the number of shots, or the change in MCP gain, gives the linear growth of the optically thin line.

For a line with absorption or gain, the recorded line intensities will differ for each plasma length. For an absorptive line, the recorded line intensities will increase as the plasma is shortened. For a line with gain, the recorded intensities will decrease as the plasma is shortened, since the actual line intensity decreases nonlinearly. If the loss or gain of the line is large, then

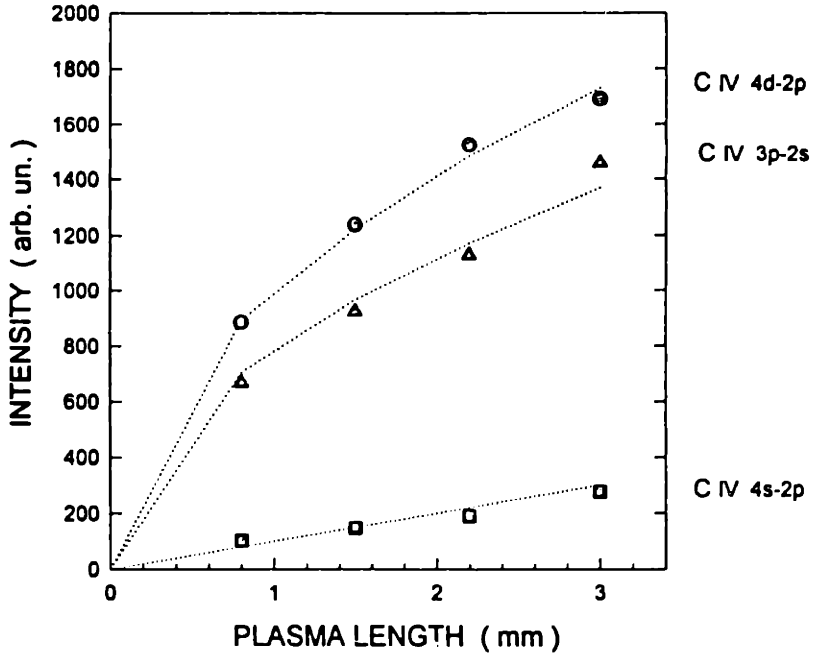

Figure 5.2: Constant dose, *I vs. L* measurement, I. Intensity growth of three lines were measured using the constant dose technique. Constant dose was maintained by varying the number of exposures for each plasma length.

the number of shots or MCP gain must be varied nonlinearly with plasma length to maintain constant film dose.

The graphs of figures 5.2 and 5.3 show the intensity growth of three Li-like C lines: 4d-2p, 3p-2s, 4s-2p. The ionization potential of Li-like C is 64 eV, which is easily achieved by our system. The pump-laser pulse duration and energy were 210 ps and 200 mJ. The emission 350 μm from the target surface was recorded. The data points represent an average of four shots for figure 5.2 and and average of two shots for figure 5.3. For the data of figure 5.2, constant dose was maintained by varying the pump-laser shots per photo. For figure 5.3, the MCP gain was varied to maintain constant dose at each plasma length. The graphs are in agreement, and indicate the presence of optically thin and absorptive lines. The data of figure 5.3 shows larger variations, which are likely due to the small number of shots taken.

For comparison, the measurements of figures 5.2 and 5.3 were repeated using the common gain measurement procedure. The dose from the full plasma length was adjusted to be just below the film's saturation level, and line intensity was directly recorded at each plasma length. Because of the spectrometer's nonlinear roll-off at low doses, see figure 4.16, all three lines exhibited exponential growth, or gain. This is not possible for these transitions with the long

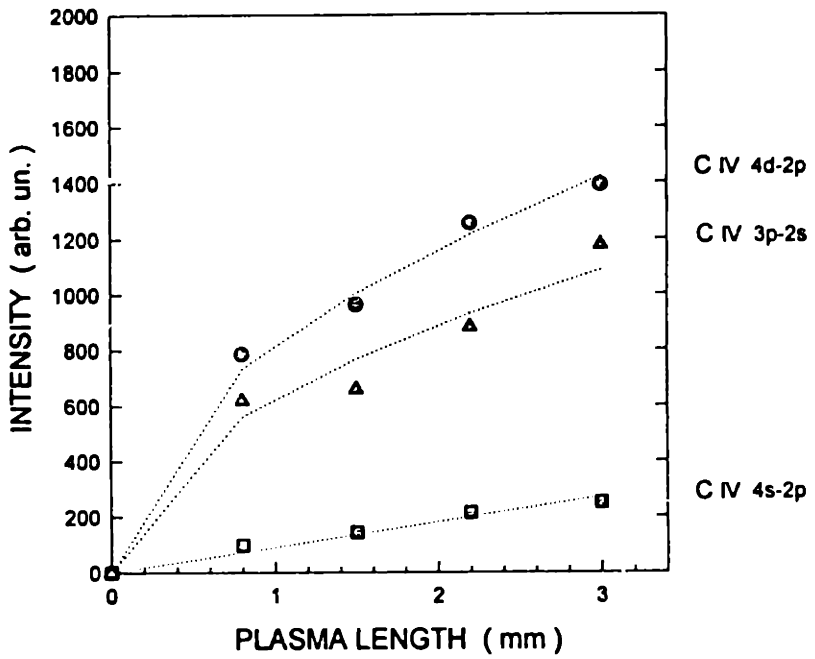

Figure 5.3: Constant dose, *I vs. L* measurement, II. The measurement of figure 5.2 was repeated. Constant dose was maintained by varying the MCP gain for each plasma length.

pump-laser pulse duration used. This result clearly indicates the inaccuracy of such a variable dose measurement.

5.3 Determining Gain or Loss

After the line intensity for each plasma length is determined from the constant dose measurement technique, the gain or absorption coefficient may be determined. The coefficient is determined by comparing or fitting the data to the gain or loss simulations described in chapter 3, sections bf 3.6 and **3.7**. Such a comparison is shown in figure 5.4.

In figure 5.4, the *I vs. L* data for the C IV lines, from figure 5.2, are compared with absorption simulations described in chapter 3. The dotted lines are theoretical curves obtained from the program ASE1. To obtain a reasonable fit, it was necessary to increase the plasma length, corresponding to the .8 mm data set, by .3 mm. Both graphs of figures 5.2 and 5.3 suggest that recorded intensities were high for the .8 mm measurement. Because of the short plasma lengths and the coarseness by which the plasma length is varied, the actual plasma length may have been longer for the .8 mm measurement. A plasma radius of 300 μm was assumed for the absorption simulation.

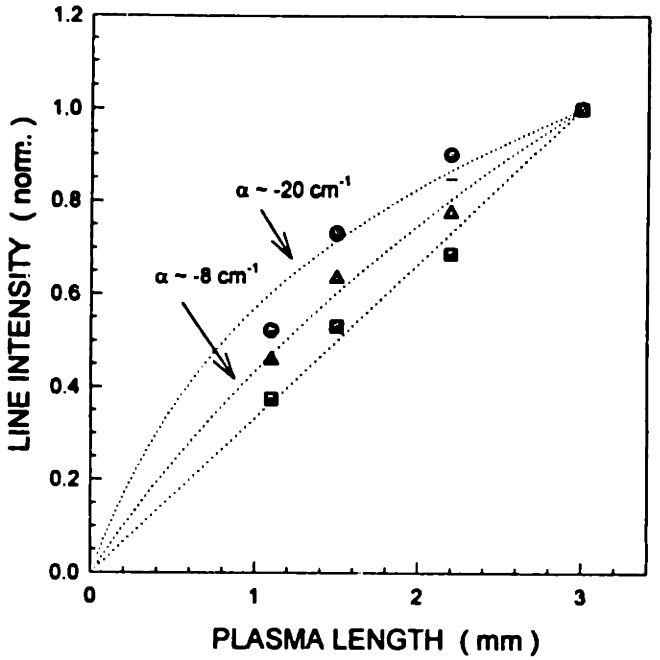

Figure 5.4: Estimate of line absorption. Results of the constant dose, I *vs.* L measurement, shown in figure 5.2, are compared with absorption simulations for the S/ICGS.

Two of the C IV lines, the 4d-2p and 3p-2s lines, show absorption. The C IV 4s-2p line grows linearly, which is expected since the transitions oscillator strength is small, $f_{ul} \approx 0.03$. The absorption coefficients of the other lines are estimated to be -8 cm^{-1} for the 3p-2s line and -20 cm^{-1} for the 4d-2p line. Better estimates of absorption might be obtained with longer plasma lengths, or with the TIFFS. The absorption values of figure 5.4 are coarse estimates, and have only been shown as a demonstration of gain analysis.

5.4 Minimum Detectable Gain-Length Product

The minimum detectable EUV gain-length product will be determined by several uncertainties. There are uncertainties associated with the plasma length, the measured "lasing line" intensity and in the value α. Also, since the S/ICGS integrates off-axis emission, the actual gain will appear much smaller in the measurement. These issues must be considered to estimate the minimum detectable gain for our system.

To obtain an estimate of the minimum detectable gain, we first consider the following hypothetical experiment. The S/ICGS is used to measure lasing line intensities for two plasma lengths: full length and half length. The maximum length of the plasma is 8 mm. Six shots are

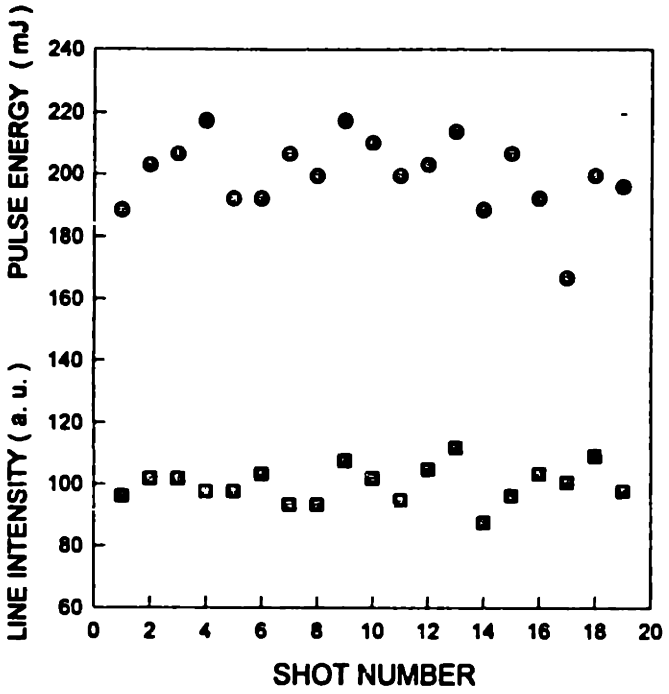

Figure 5.5: Fluctuations of pump-laser energy and S/ICGS line intensity.

taken at each length and the signals averaged for each length. The S/ICGS has a 50 μm input slit and a 1.8 cm diameter aperture over the concave grating. An intensity slope, m_g, is determined from the two data points, and the slope is compared to a "no gain" slope. Under these conditions and considering the experimental uncertainties, we desire to know the probability that an actual gain-length product will be missed in the measurement. Rephrased, we desire to know the probability that a "no gain" slope would be measured [102].

First, the uncertainties in plasma length, L, and line intensity, I, must be known. These uncertainties have been determined from the experiments. The error in determining plasma length is estimated from the experiments to be about ± 0.5 mm. This corresponds to the accuracy with which the beam block, figure 5.1, can be positioned. This error is systematic. The uncertainty in recorded line intensity arises from fluctuations in the pump-laser pulse energy. Fluctuations in the pump-laser pulse energy, see figure 4.8, will cause fluctuations in the EUV line intensity. The uncertainty in recorded line intensity, ΔI, has been determined experimentally to be about 6 %.

To evaluate ΔI, 19 measurements were made of the pump-laser energy and the intensity of a non-lasing EUV line. The signal levels for each shot are shown in figure 5.5. For this data, the pump-laser pulse energy was about 200 mJ and the pulse duration was 210 ps. Histograms

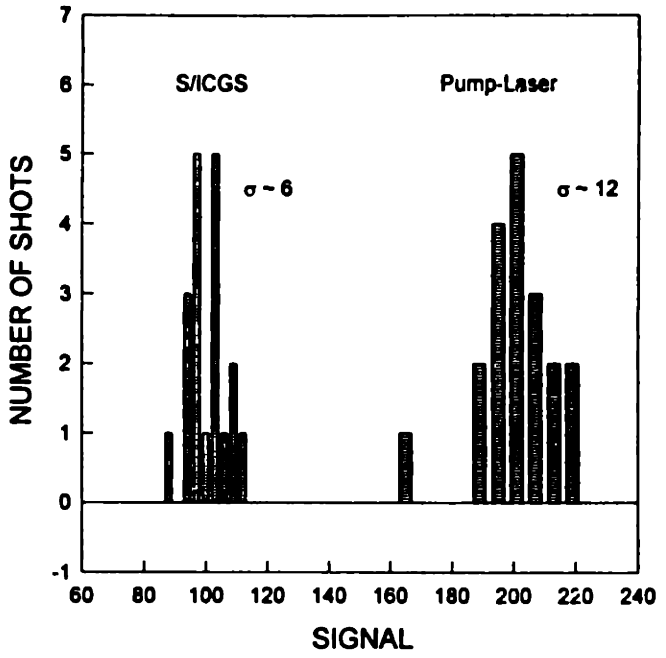

Figure 5.6: Histograms of EUV line intensity and pump-laser pulse energy.

of the two data sets are shown in figure 5.6. The standard deviation, σ, was estimated to be about 6 % of the mean signal value for both the data sets. Considering the complexity of the system, this small value for σ is somewhat surprising.

Fluctuations in the pump-laser energy will also cause fluctuations in the small signal gain, α. Different pulse energies will cause different plasma conditions, or gain conditions. Two values will be used for the uncertainty in α: 20 % and 40 % . Results from one recent experiment which resulted in gain [71], suggest that the actual uncertainty may be closer to 40 %.

Next, using the relation [103]

$$\sigma_f^2 = \frac{\partial f}{\partial u}^2 \sigma_u^2 + \frac{\partial f}{\partial v}^2 \sigma_v^2 \tag{5.1}$$

where σ_f^2 is the variance of $f(u,v)$, the uncertainties in I, L, and α can be propagated through the Linford expression. This gives an uncertainty for the measured line intensity at each plasma length. These uncertainties are propagated to find the uncertainty in the measured slope, Δm_g. The probability of detecting no gain may be evaluated from Δm_g and the number of standard deviations that the "no gain" slope is away from the measured "gain" slope, m_g.

Table 5.1 lists the probabilities of detecting no gain, P_n, for several values of gain-length product. Two cases have been analyzed. In the first case, the systematic error for plasma length, ΔL, is .5 mm. This systematic error can be reduced experimentally by verifying that

Table 5.1: Probabilities of measuring no gain.

αL	P_n	
	σ_L = .50 mm	
	$\Delta\alpha$ = 20%	$\Delta\alpha$ = 40%
0.4	56	66
0.8	28	42
1.6	10	22
2.4	6	18
	σ_L = .25 mm	
0.4	44	60
0.8	15	34
1.6	3	16
2.4	2	13

an optically thin line grows linearly. Consequently, a second case, for which $\Delta L = .25$ mm, has also been analyzed. The results show the sensitivity of P_n to both fluctuations in α, and to ΔL.

From table 5.1, it is reasonable to conclude that a gain-length product of 1.6 would be detected in the experiment. For smaller gain-length products, there is significant probability that no gain would be measured. Further, because of the off-axis emission collected by the S/ICGS, a gain-length product of 1.6 would appear as $\alpha L \approx 1$, see figure 3.6. Once gain is detected, a careful measurement with either more shots or more plasma lengths will determine the gain value more accurately.

Chapter 6

Laser-Driven Plasma Experiments

6.1 Introduction

Several preliminary laser-driven plasma experiments were conducted with the table-top EUV system. Basic plasma heating experiments were performed with boron-nitride and the time integrating flat-field spectrometer. This set of experiments was intended verify that the system behaved as expected. Another set of experiments was conducted to determine the best operating configuration for the system. Results from these experiments were used to configure the pump-laser in its best operating mode for EUV gain studies. A series of measurements were made to estimate the laser-produced plasma density profile under different pumping conditions. In one of these measurements, a specially designed blade placed over the lasant target was observed to create a plasma conduit which would be ideal for end-pumped plasmas. Finally, several ionization studies were carried out for different lasants. From the ionization studies, we estimate that an electron temperature of about 200 eV can be achieved with the pump-laser configured in long pulse mode. Descriptions of these experiments and selected data are presented in this chapter.

6.2 Preliminary Heating Studies

Two simple heating experiments were performed to verify that the pump-laser and laser-produced plasma behaved as expected. In the first experiment, soft x-ray emission from a boron-nitride (BN) plasma was monitored with the TIFFS as the pump-laser pulse energy was increased. In the second experiment, the same spectral emission was measured as the number of pump-laser pulses was increased. In these experiments, we expected the plasma emission to indicate a hotter plasma when pulse energy, or pulse number was increased. This result was observed.

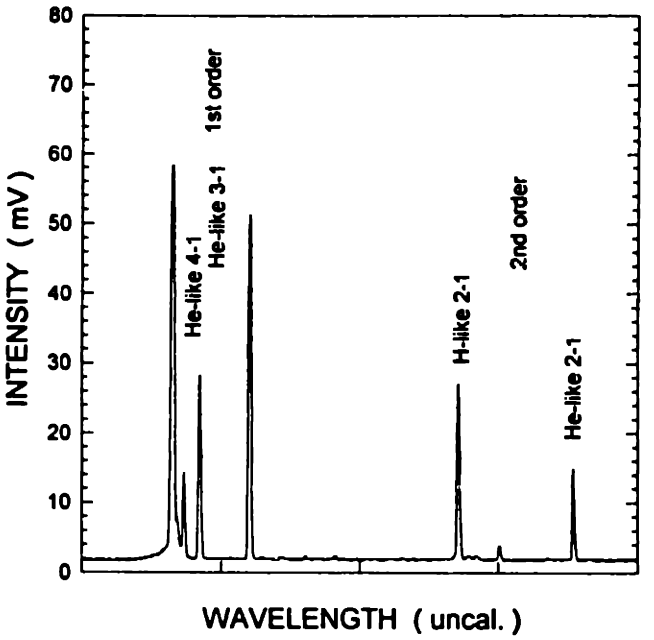

Figure 6.1: Sample BN spectrum used for preliminary heating experiments.

For both experiments, the pump-laser was focused to a spot, about 40μm×500μm, and pulse energies were kept below 200 mJ to avoid damaging the vacuum chamber entrance window. The pump-laser pulse length was 210 ps. The input slit of the TIFFS was 50 μm, and spectral data was recorded on Polaroid 107 film.

Four spectral lines from the BN plasma were monitored, in first and second order, with the TIFFS and are shown in the sample spectrum of figure 6.1. The detected lines corresponded to the H-like B 2p-1s (L1), He-like B 2p-1s (L2), He-like B 3d-2p (L3) and He-like B 4f-3d (L4) transitions. Three line ratios were determined from the measured spectra: $R_0 = \frac{L1}{L2}$, $R_3 = \frac{L3}{L2}$ and $R_4 = \frac{L4}{L2}$. The ratio R_0 was determined from the second order spectra while the other ratios were calculated from the first order spectra. Because Polaroid film was used, care was taken to restrict the exposures to the films linear range so that only small saturation corrections were needed estimate the line ratios. Since the wavelength response of the film and spectrometer are not known precisely, the determined line ratios are not absolute.

For the first heating study, one pulse was used to excite the plasma. The pulse energy was increased, by factors of two, from 25 mJ to 200 mJ. At 200 mJ, the intensity on the target was estimated to be 4.7 x 10^{12} W cm^{-2}. Two shots were required to expose the Polaroid film at 200 mJ, and 50 shots were necessary at 25 mJ. The TIFFS entrance slit was centered 220 μm

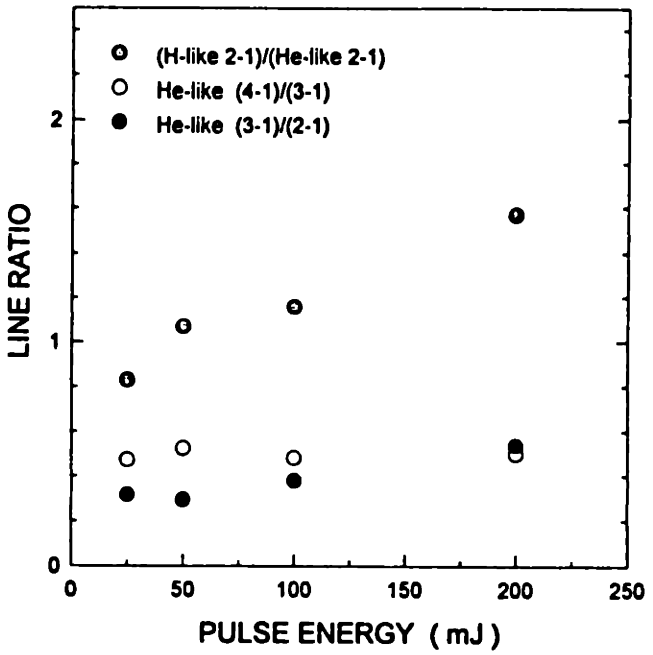

Figure 6.2: Spectral line ratios *vs.* pump-laser pulse energy.

above the target surface. The measured line ratios are plotted in figure 6.2 as a function of pulse energy.

Two observations can be made from figure 6.2. One observation is that the ratios R_0 and R_3 both increase by about a factor of two as pulse energy is increased. R_0 indicates ionization balance in the plasma, and a larger value of R_0 indicates an increased presence of H-like B ions. Since the ionization potential to produce H-like B, 259 eV, exceeds that required to produce He-like B. 38 eV, an increase in the ratio R_0 can also be interpreted as an increase in electron temperature.

Another observation from figure 6.2 is that the ratio R_4 increases only slightly. This result is not well understood. One possible explanation is that the He-like 4-3 transition is collisionally mixed [5, page 147] and that the plasma has cooled to a nearly constant temperature by the time it reaches the slit. The line ratio would then be determined by the electron density, which might increase slightly with higher pulse energy.

For the second heating study, multiple pulses were used to excite the BN plasma. The pulses were spaced 7.5 ns apart and the energy of each pulse was about 100 mJ. The TIFFS entrance slit was centered 190 μm above the target surface. Two shots were averaged for each data point.

Measured line ratios for the multi-pulse experiment are shown in figure 6.3. Since the TIFFS

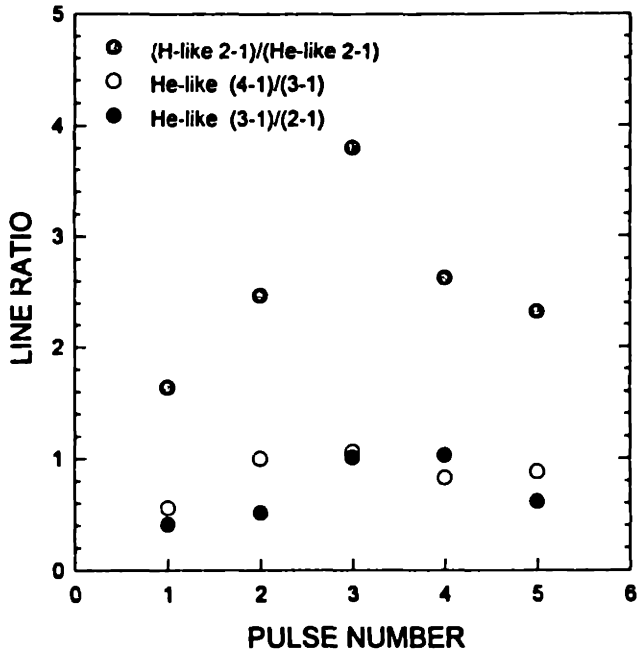

Figure 6.3: Spectral line ratios *vs.* pulse number.

was used, line ratios were calculated for each pulse by subtracting the contribution from previous pulses. Because of this procedure, uncertainties in line ratios increase with pulse number.

All line ratios are observed to increase until the third pulse in figure 6.3. The increase in line ratios is larger for two or three pulse pumping than was observed for increasing the energy of a single pulse. For example, doubling the energy of a single 210 ps pulse increases the R_0 value by a factor of 0.46. Using a second pulse increases the value of R_0 by a factor of 1.5. The data also indicates a hotter plasma at 190 μm above the target surface; compare the first pulse line ratios with the 100 mJ data set of figure 6.2.

The leveling-off of line ratios may be due to a steady state density profile established by the plasma. The decay in line ratios may suggest movement of the plasma's critical surface. As more pulses heat the plasma, more density is ablated and the critical surface may move toward the slit. As the critical surface approaches, the plasma temperature falls.

Qualitatively, temperature sensitive line ratios were observed to increase in both experiments. These results verify that the system operates as expected. Results from the multi-pulse experiment also indicate the advantage for using two or three pulses for collisionally pumped EUV lasers.

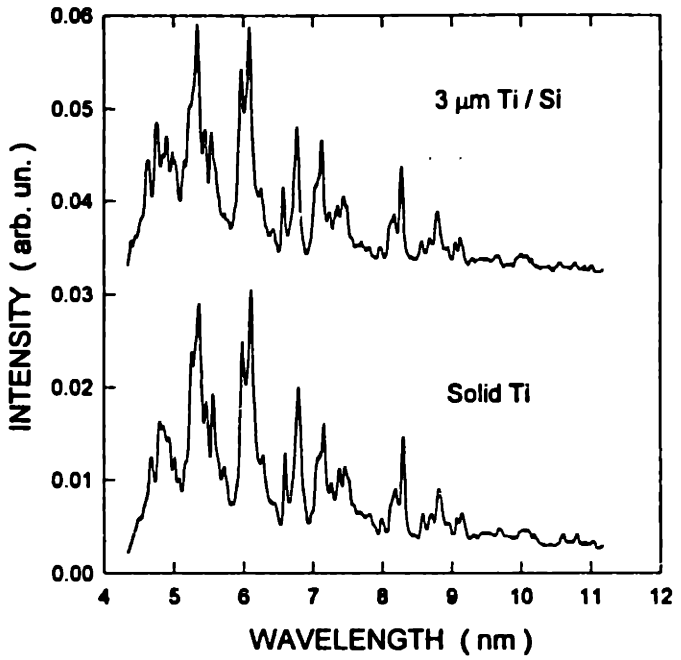

Figure 6.4: Comparison of spectra for solid and thin film Ti targets.

6.3 System Optimization Experiments

Several experiments were carried out to determine the best operating configuration for the EUV system. The goal of the experiments was to determine which configuration resulted in the hottest laser-produced plasma. In some experiments, target design and geometry was varied. The results from these experiments indicated that the hottest plasma was created with multiple 210 ps pulses which transversely pumped a flat slab target. These optimization experiments are described in this section.

6.3.1 Target Design

Spectral emission from two titanium targets, of slightly different design, were compared. One target was a solid slab, 2 mm thick, of Ti metal. The second target consisted of a 3 μm layer of Ti deposited on a 1 mm thick Si wafer. Because of a lower heat conductivity for Si, it was postulated that the Ti-on-Si target would result in a higher plasma temperature since less heat would be conducted to the solid substrate. The pump-laser pulse length was 210 ps and the pulse energy was 500 mJ. The plasma length was 5 mm. One pulse and one exposure were used to obtain the spectra, which were recorded with the TIFFS. The input slit width was 50 μm for the TIFFS. Short wavelength spectra from each target are compared in figure 6.4.

The spectra of figure 6.4 show little difference for the two Ti targets. Both spectra show an abundance of Na-like Ti ions, for which the ionization potential is 292 eV. Short wavelength lines between 4 nm and 6 nm are from Na-like Ti np-3s and nd-3d transitions. The lines at 6.1 nm and 8.2 nm are from the Na-like Ti 5p-3s and 4p-3s transitions, respectively [21]. By taking three exposures or increasing the pulse energy to 1000 mJ, lines below 3.5 nm could be detected for both targets. These lines corresponded to Ne-like Ti 3l-2p transitions [21].

The data from this experiment indicate that there is no significant difference in plasma heating between the two target designs. One possible reason for this result is that the 3 μm target was sufficiently thick so that it mimicked a solid target. However, earlier experiments with 1 μm thick Mo-on-Si targets indicated that the deposited layer was too thin: Si lines were observed in the spectra. Also, after completing the experiment, the 3 μm Ti-on-Si target showed large ablation spots, which appeared to be stripped to bare Si. Other data from the S/ICGS showed that only one pump-laser shot per mm of target length could be taken with the Ti/Si target. Taking a second shot at the same target location resulted in substantially reduced Ti emission from the plasma. From these results, we concluded that there would be little difference between choice of target for subsequent experiments.

6.3.2 Pulse-Length Studies

The pump-laser system could be operated in several configurations with several different pulse-lengths and pulse energies, as described in chapter 4. Shorter pulse durations result in higher peak pumping intensity, while longer pulse-lengths allow higher pulse energy. The result of C. Max, equation 3.2 of chapter 3, suggests that higher electron temperature can be achieved in the plasma with higher pumping intensity. Several experiments were carried out to determine the best operating configuration for the pump-laser system. Results from these experiments indicated that long pulse durations, 210 ps, and high pulse energies, 3 J, were preferred for creating plasmas with the hottest spectra.

For the pulse-length studies, the pump-laser was operated in four different configurations. Two configurations were with the chirped pulse amplification stages described in chapter 4, and two were without the CPA stages. Using the CPA stages, pulse durations of 24 ps and 140 ps were achieved. Without the CPA stages, 70 ps and 210 ps pulses were produced. Plasma emission, recorded with both the TIFFS and S/ICGS, was studied using these four pulse lengths.

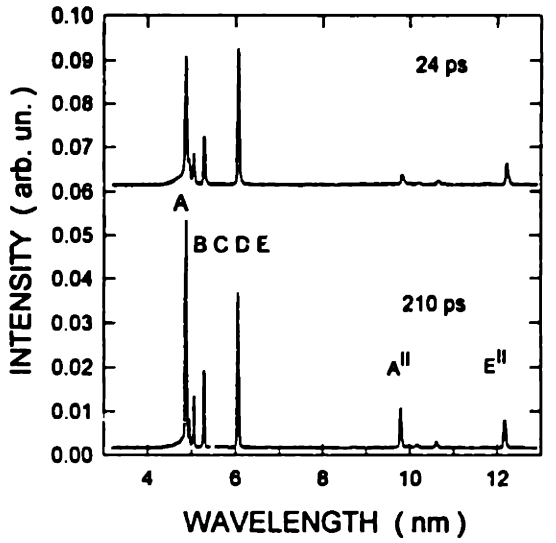

Figure 6.5: Soft x-ray spectral emission from a BN plasma created with 24 ps and 210 ps pulses. Lines identified in the graph are A: H-like B 2p-1s (4.86 nm), B: He-like B 5p-1s (4.94 nm), C: He-like B 4p-1s (5.04 nm), D: He-like B 3p-1s (5.27 nm), and E: He-like B 2p-1s (6.03 nm). Wavelengths are from reference [28].

Emission from both low Z targets, C and BN, and a moderate Z target, Ti, was observed for each pulse length. To simulate gain conditions, the plasma length was kept constant at 5 mm for all the measurements. Also, the pump-laser pulse energy was limited to 800 mJ. The input slit width for the TIFFS was 50 μm, and 25 μm for the S/ICGS.

In one experiment, a single pulse was used to create a BN plasma. For recombination EUV lasers such as H-like B or C, a single pulse is used to create the plasma. The pulse energy was 500 mJ. The spectrometer slits were scanned toward the target surface to locate the hottest plasma region. Raw data from the TIFFS is shown in figure 6.5 for two pulse lengths, 24 ps and 210 ps. Raw data from the S/ICGS is shown in figure 6.6 for the same pumping conditions.

The spectra of figure 6.5 clearly indicated that a hotter plasma was produced with the 210 ps pulse. The hottest plasma region was found to be about 180 μm above the target surface for the 210 ps pulse, and about 140 μm above the surface for the 24 ps pulse. The values of the line ratios, R_0, R_3 and R_4, which were defined in section **6.2**, were found to be 0.95, 0.35, and 0.64 for the 24 ps pulse and 1.48, 0.51 and 0.67 for the 210 ps pulse, respectively. For these measurements the peak pump-laser intensity for the 210 ps pulse, 1.2×10^{12} W cm^{-2}, was

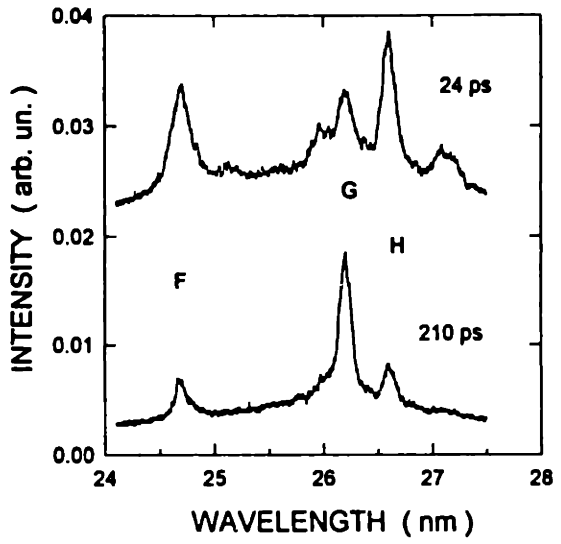

Figure 6.6: EUV spectra from a BN plasma created with 24 ps and 210 ps pulses. Lines identified in the graphs are F: Li-like N 3d-2p (24.7 nm), G: H-like B 3d-2p (26.2 nm), and H: Li-like N 3s-2p (26.6 nm). Wavelengths are from reference [31].

estimated to be nearly nine times lower than that for the 24 ps pulse. It should be noted that the time-integrated ionization spectra recorded in these measurements are indirect indicators of plasma temperature.

Long wavelength spectra recorded with the S/ICGS also showed that a hotter plasma was created with longer pulses. Emission near the H-like B 3d-2p "lasing line" was recorded for the 24 ps and 210 ps cases. Two nearby lines were determined to be Li-like N lines as noted in figure 6.6. The ionization potential for Be-like N is 77 eV, compared with 259 eV for He-like B. The prominence of the H-like B line in the 210 ps spectrum indicates a hotter plasma.

In a separate experiment with carbon as the target, the threshold pumping intensity required to produce emission from the H-like C 3d-2p transition was determined as a function of pulse length. The ionization potential of He-like C is 392 eV. Again, a single pump-laser pulse was used to create the plasma. For these measurements, the pump-laser pulse energy was reduced by factors of two until the H-like C 3d-2p emission at 18.2 nm was extinguished compared to a nearby He-like C line at 18.7 nm. The threshold was not well defined, but is estimated to be within ± 20 % of the reported value. The measured threshold pumping intensities are plotted in figure 6.7 for each of the four pulse lengths. The threshold value significantly decreased for

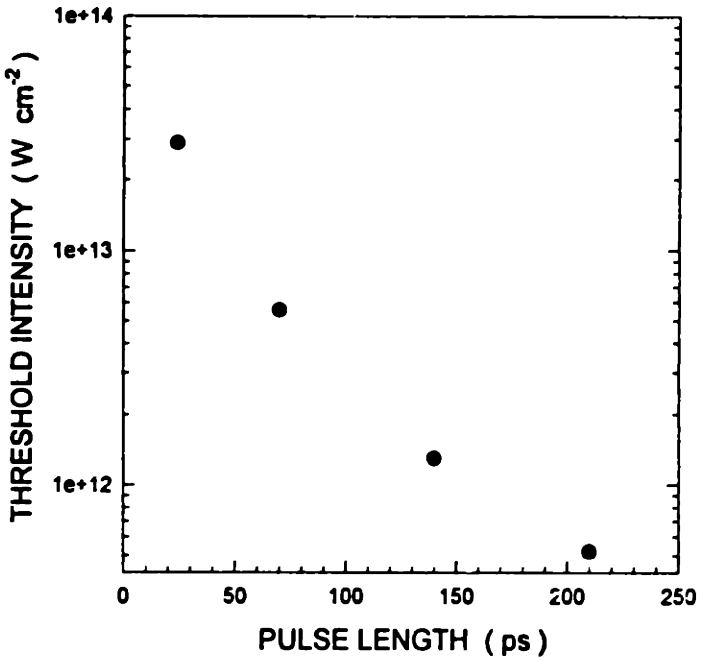

Figure 6.7: Pump-laser intensity required to produce H-like C 3d-2p emission for several pump-laser pulse lengths.

the longer pump-laser pulse durations.

Pulse-length studies were also made for the collisionally pumped EUV lasant, Ti. Short wavelength emission from a Ti plasma was recorded with the TIFFS for 24 ps and 210 ps pulses. The pulse energy was 500 mJ. The spectra from four measurements are shown in figure 6.8. For the 24 ps case, two pulses separated by 7.5 ns were used to excite the plasma, while one pulse was used for the 210 ps measurement. The spectra above 4 nm show an abundance of Na-like Ti emission for both pulse durations, and also show a dramatic increase in line emission for the long pulse case. This result suggests that less mass is ablated with the short pulses, although the temperature reached with two short pulses is nearly the same as that achieved with one long pulse.

The Ti spectra below 3 nm were obtained by taking multiple exposures with the TIFFS. Eight exposures were required to obtain the spectra. The hottest region of the plasma was observed to be 170 μm above the target for the 24 ps pulse, and 240 μm for the 210 ps pulse. Again, two 24 ps pulses were used for the short pulse case, while one 210 ps pulse was used for the long pulse case. This data also indicated that the plasma was heated more efficiently with the long pump-laser pulse.

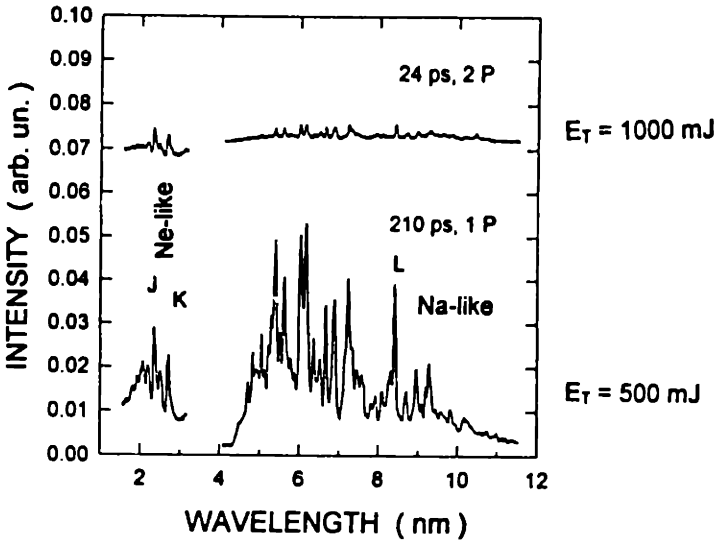

Figure 6.8: Ti soft .. ray spectra from a 24 ps and 210 ps laser-produced plasma. Lines identified are J: Ne-like Ti $2p^5 3d\text{-}2p^6$ (2.4 m), K: Ne-like Ti $2p^5 3s\text{-}2p^6$ (2.7 nm) and L: Na-like Ti 4p-3s (8.2 nm). Wavelengths from reference [21].

EUV emission near the candidate Ne-like Ti lasing line was observed with the S/ICGS for each pulse length. Na-like emission was observed for both long and short pulse durations. The intensity of spectral lines was significantly lower for the short pump-laser pulses as was observed for the short wavelength spectra in figure 6.8. The candidate lasing line was not observed in these measurements.

Results from the pulse-length studies for both low Z and moderate Z lasants indicated that the plasma was heated more efficiently with long pulses. Consequently, the pump-laser was configured for long pulse mode for the majority of lasant survey experiments, which will be discussed in chapter 7. However, a few survey measurements were also made with short pump-laser pulses.

A similar pulse length study has been carried out with fiber targets at another laboratory [104]. In these experiments pulse lengths were decreased to 800 fs, and the pulse energy was about 40 J. It was found that required ionization stages for recombination lasants were not achieved for pulse lengths below 2 ps.

6.3.3 Plasma Pumping Arrangements

Normally, EUV laser plasmas are created with a transverse pump-laser beam as illustrated in figure 1.1 of chapter 1. This pumping arrangement maximizes energy transfer to the plasma from the pump-laser beam [19]. Recently, several table-top EUV lasers have been longitudinally pumped with ultrashort pulses [69,70] to achieve high gain. In one of these experiments [69], the pump-laser is focused into a Xe gas, which was the EUV lasant. In the other experiment, the pump-laser is focused into a preformed plasma, which is created by a second transverse pump-laser beam. The advantage of longitudinal pumping is that the pump-laser can be tightly focused to achieve very high pumping fluence or intensity. However, this benefit may be cancelled by pump-laser beam refraction in the plasma.

Several pumping arrangements were tested experimentally in an effort to increase the plasma temperature. Transverse pumping and transverse-and-longitudinal (T & L) pumping arrangements were examined. For the pumping arrangements used, transverse pumping with two beams, was found to be the most efficient pumping scheme. Results from these experiments are discussed in this section.

The T & L pumping arrangement investigated in our experiments is shown in figure 6.9. A novel capillary target was used for the T & L pumping scheme, and the capillary diameters were 500 μm, 750 μm and 1 mm. The capillary was created by drilling a hole near the surface of the target, and then using the transverse beam to burn a slot through the edge of the capillary wall. The capillary was used to help guide the longitudinal pump-laser beam and minimize beam refraction effects. 5 mm and 8 mm long targets were tested.

The longitudinal beam was brought through the side of the vacuum chamber, nearly collinear with the EUV laser axis. To accomplish this, a spectrometer had to be disabled to allow passage of the pump-laser beam. Because of the chamber design, the minimum angle between the longitudinal pump-laser beam and the EUV laser axis was 2.3 degrees. A 1 m spherical lens was used to focus the longitudinal beam to a spot size of approximately 80 μm$\times$260μm.

The plasma was preformed by the transverse beam, which preceded the longitudinal beam by 3 ns in one experiment and 8 ns in another experiment. To verify interaction of the longitudinal beam with the preformed plasma, burn patterns of the longitudinal beam were recorded after the target, with and without the transverse beam. The burn patterns are shown in figure 6.10. The pattern obtained with both pump-laser beams indicates beam refraction and break-up due

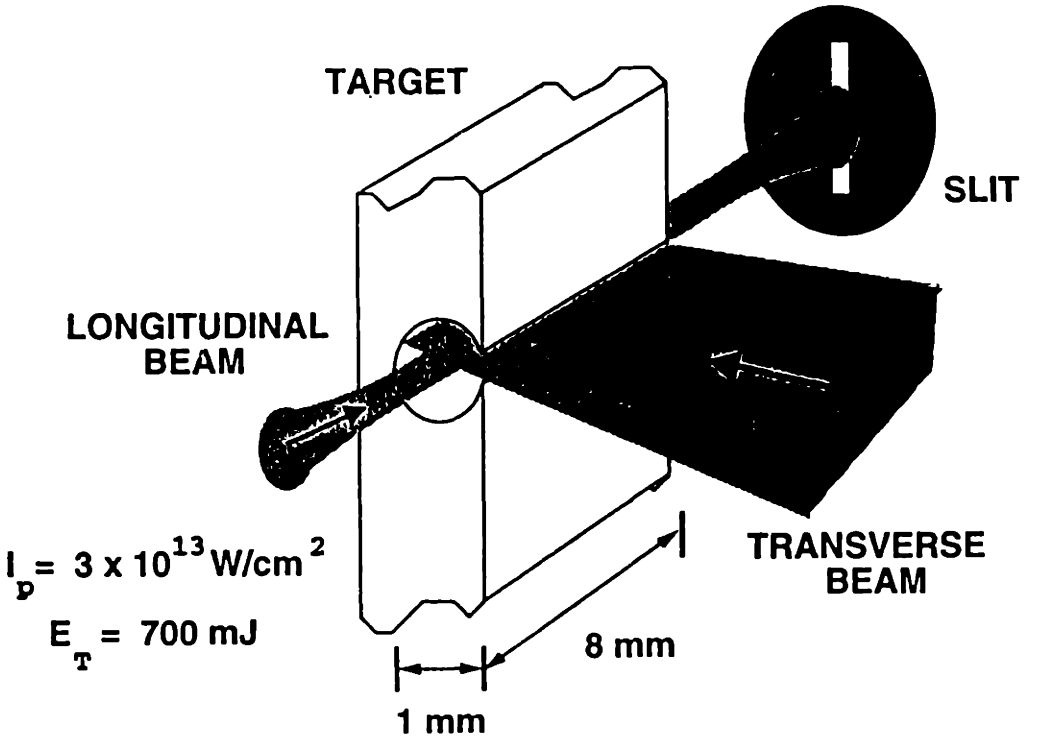

Figure 6.9: Transverse-and-longitudinal pumping arrangement.

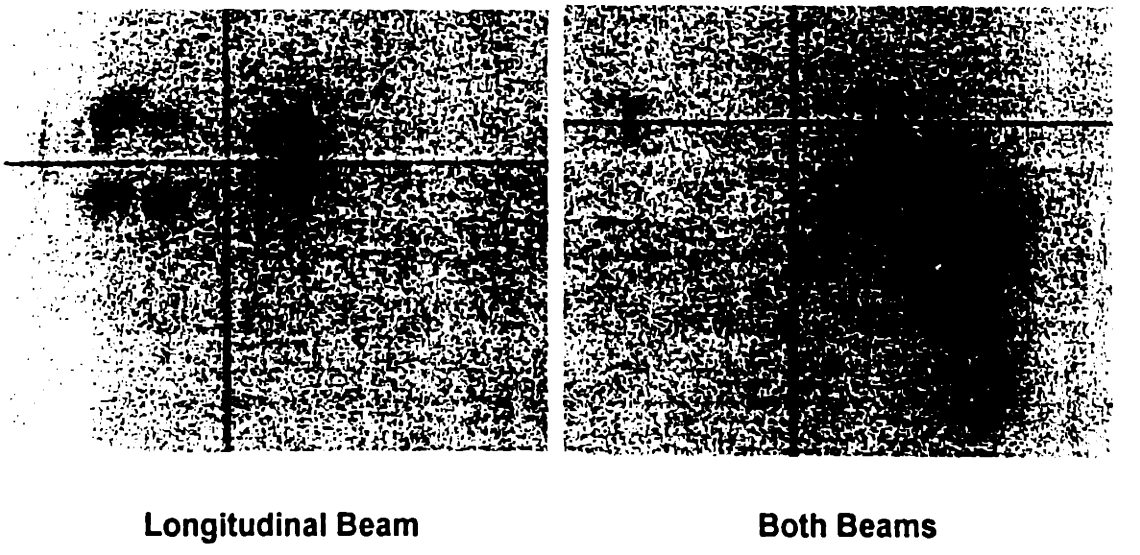

Figure 6.10: Interaction of the longitudinal pump-laser beam with the preformed plasma.

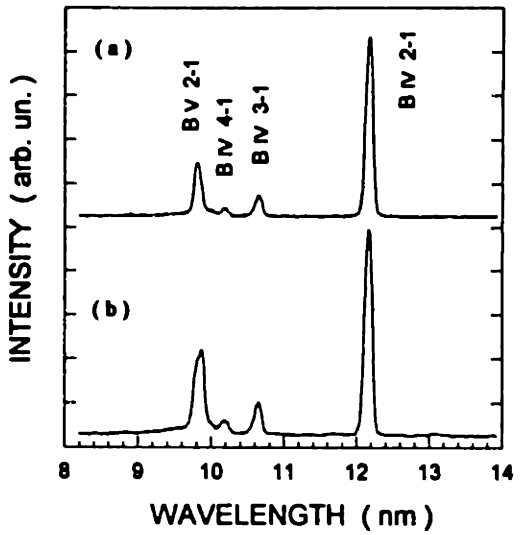

Figure 6.11: Short wavelength spectra for transverse (a) and transverse-and-longitudinal (b) pumped BN plasma. The spectra show little difference between the two pumping arrangements.

to the preformed plasma.

Spectra were recorded for the T & L pumped capillary target with both the TIFFS and the S/ICGS. Short wavelength spectra recorded with the TIFFS for an 8 mm long BN capillary is shown in figure 6.11. The pulse energy was 350 mJ, and the delay between transverse and longitudinal pulses was 3 ns. The spectra show little difference between the two pumping arrangements, which is surprising considering that the pump-laser fluence incident on the plasma is 15 times higher for the T & L pumping scheme. Data from the S/ICGS indicated that the T & L pumped plasma was colder than the transverse pumped plasma. EUV emission near the H-like B 3d-2p candidate lasing line is shown in figure 6.12. For this data, the pulse energy was increased to 1200 mJ.

Similar results for transverse-and-longitudinal pumping have been reported at another university [76]. In those experiments, it was discovered that the longitudinal pump-laser beam had to be carefully aligned to the EUV laser axis. Otherwise, emission from the plasma indicated a cold plasma. This was believed to be due to excess mass ablated by the tightly focused longitudinal beam. The experimenters did find that with careful alignment, a H-like C plasma shows signs of high gain. However, these results are very recent and not yet well understood.

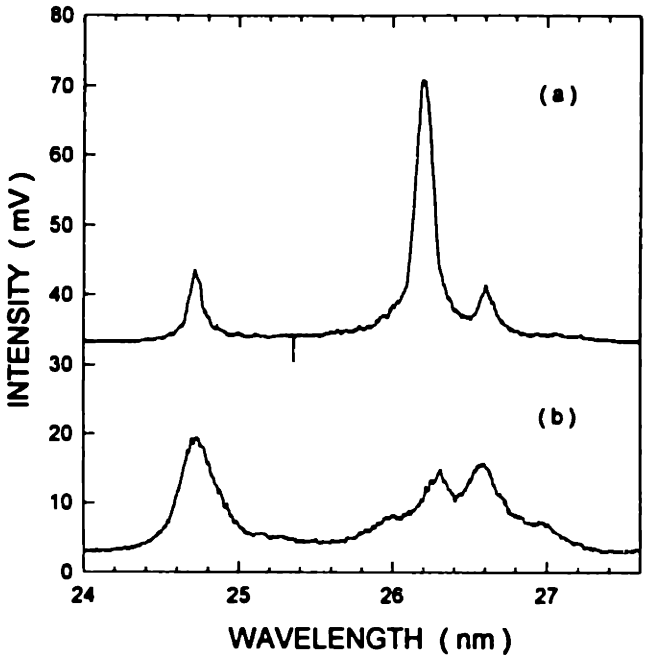

Figure 6.12: EUV spectra for a transverse (**a**) and T & L (**b**) pumped BN plasma. The T & L pumped emission indicates a colder plasma.

Based on our preliminary T & L pumping results, this pumping arrangement was abandoned in later experiments. All lasant survey data was obtained with transverse pumping only.

6.4 Plasma Profiles

Three observations were made of the plasma profile. In two of the measurements, a spectrally resolved image of the plasma was obtained with the S/ICGS. In the other experiment, the TIFFS was used to study short wavelength emission from the plasma. Results from a BN plasma is reported for each of these experiments. The data suggests that the density profile of the plasma is smaller than expected [77]. A small density profile would result in large density gradients, which would increase beam refraction in the plasma. Further experiments and analysis are required to determine the actual density profile for our plasmas.

6.4.1 Transverse Width of Plasma

The S/ICGS was used in imaging mode, with a 25 μm×3 mm input slit, to obtain spectrally resolved images of the plasma. Images were recorded between 100 μm and 1000 μm above the target surface. The resulting images at transition wavelengths were used to determine the transverse width of the plasma as a function of distance from the target. The transverse direction

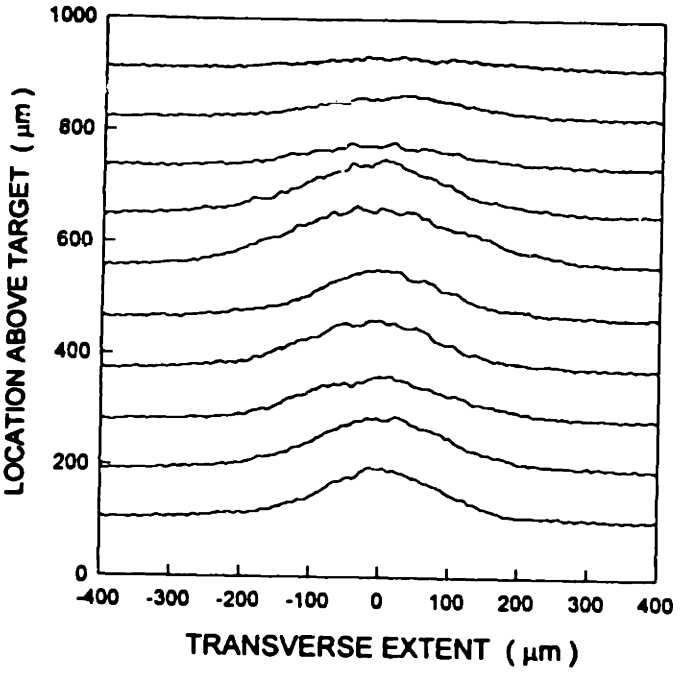

Figure 6.13: Transverse plasma profiles *vs.* distance from target surface.

was taken to be a direction parallel to the target surface and perpendicular to the EUV laser axis.

Images of the H-like B 3d-2p line were recorded at ten different heights above the target. Since the ionization potential for He-like B is about 259 eV, the 3d-2p line emission originated from a hot region of the plasma. For this measurements, the plasma length was 8 mm and the pump-laser pulse energy was 2.5 J. The pulse duration was 210 ps, and only one shot was taken at each distance above the target surface. The images were scanned with the densitometer, and the raw data is shown in figure 6.13.

The data indicates that the 3d-2p emission is prominent in a region about 200 μm wide extending 800 μm away from the target surface. The transverse width of the emission increases slightly with distance away from the target, and the line intensity decreases. Similar results were found with the H-like C 3d-2p line, although the emission extended only 600 μm above the target surface. The difference between C and B is expected qualitatively since C is heavier and more difficult to ionize.

The transverse plasma width and B V 3d-2p line intensity were determined from the traces of figure 6.13 for each slit location. The data, plotted in figure 6.14, shows the width of the plasma increases from $\sim$ 170μm to $\sim$ 250μm. Near the target surface, the transverse plasma width

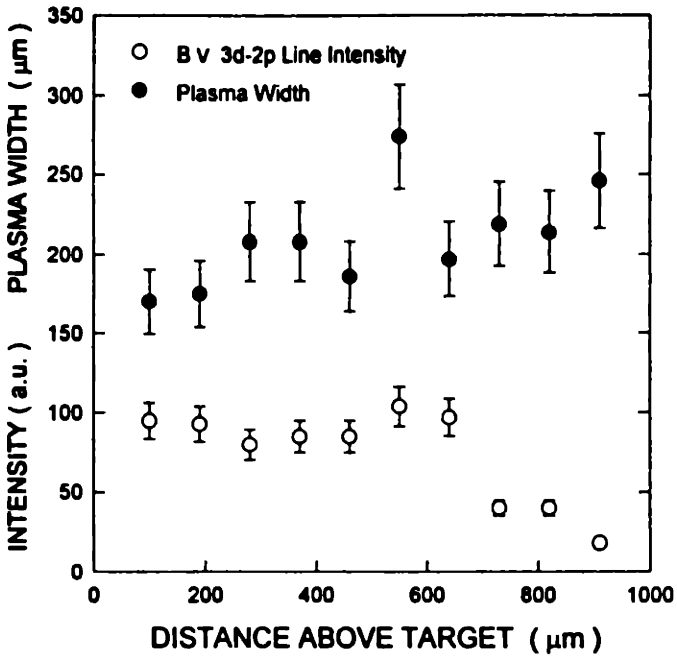

Figure 6.14: Plasma width and B V 3d-2p line intensity *vs.* distance from target surface.

measured is determined by the spatial resolution of the S/ICGS, $\sim 150\mu$. The actual plasma width is expected to be closer to the pump-laser line focus width of 40 μm. The measurement 900 μm above the target more accurately reflects the plasma width. However, the measured width is significantly smaller than would be expected for half-cylindrical expansion, and suggests that the plasma expansion may be closer to planar. The data may also indicate that a two-dimensional hydrodynamic model is required to simulate plasma formation more accurately.

The H-like B 3d-2p line intensity was observed to remain nearly constant from 100 μm to 600 μm above the target. This result cannot be interpreted as constant plasma conditions for this region. Near the target, the plasma is hotter and denser, and has a smaller transverse width. As the plasma expands, the density and temperature drop. Decreased line emission due to a reduction in density is offset by an increase in the recombination rate due to lower temperatures, see section **3.3** of chapter 3. Also, the optical density of the plasma decreases with density, so that more emission escapes. Consequently, the line intensity does not reflect the local ion density.

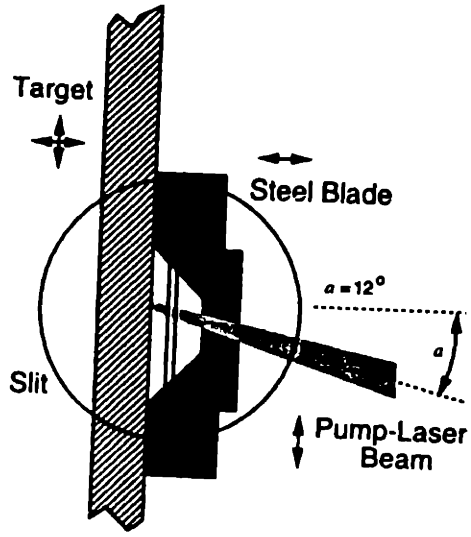

Figure 6.15: V-blade used to create a plasma conduit.

6.4.2 Creation of a Plasma Conduit

It was discovered in a series of "blade" experiments with recombination lasants, that a plasma conduit could be created with a special blade design. A plasma conduit consists of a region of low electron density surrounded by a region of higher electron density. Such a conduit can act as an optical waveguide. A plasma conduit would be ideal for EUV lasers and longitudinally pumped EUV lasers for which EUV or pump-laser beam refraction decreases EUV laser performance. Creation of a plasma conduit is described in this section.

A V-shaped steel blade was fabricated and placed over the BN target. The blade, shown in figure 6.15, was about 12 mm long and had a 45° wedge milled along the length of the blade. The depth of the wedge was 850 μm. At the apex of the wedge, a 120 μm wide slot was milled through the steel to allow passage of the line-focused pump-laser beam. The plasma length was 8 mm and the pump-laser pulse energy was reduced to 600 mJ in order to obtain a higher resolution image of the plasma. The S/ICGS was used in imaging mode to observe the end of the target and blade assembly.

Two transverse profiles of the plasma created with the V-blade are shown in figure 6.16. The actual image is inset in the figure. The profiles were obtained with a method which was described in the previous section. The lower trace, marked (b) in the figure, was taken in a spectral region for which there was no BN emission. The trace shows two emission peaks separated by

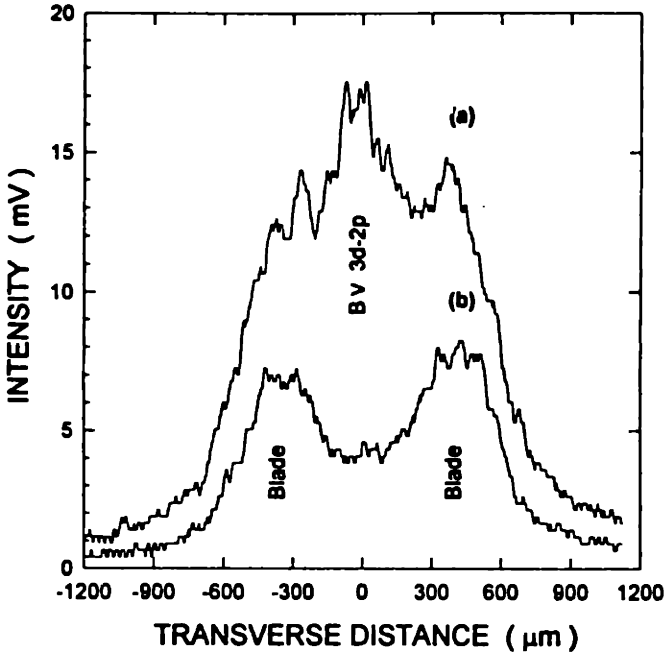

Figure 6.16: Transverse profiles of the plasma created with the V-blade.

800 μm. These peaks are due to plasma near the blade surface. Further experiments revealed that this secondary plasma is created by the expanding BN plasma, and its temperature is low, around 30 eV. The upper trace, **(a)**, of figure 6.1 was taken in the wavelength region around 26.2 nm, which contained the H-like B 3d-2p transition. The 3d-2p line appears between the blade plasmas. The reduced intensity between the peaks of trace **(b)** suggests the presence of a plasma conduit. This data also indicates that the pump-laser beam is not coherently reflected from the BN target surface as was previously thought [2].

The V-blade was used in several transverse pumped and T & L pumped gain experiments. The target design reported in section **6.3.3** was motivated by the results reported in this section. No improvements were noted when the V-blade design was used. For the transverse pumped BN experiment, the plasma appeared colder with the blade. However, for the reasons noted in section **6.3.3** this design may be useful for further T & L pumping experiments.

6.4.3 Absorption Measurements

The TIFFS was used to study soft x-ray emission from an 8 mm long BN plasma. The absorption coefficient for the H-like B 2p-1s line was estimated from several measurements. Results from these absorption measurements suggest that the plasma density gradient near the gain region is

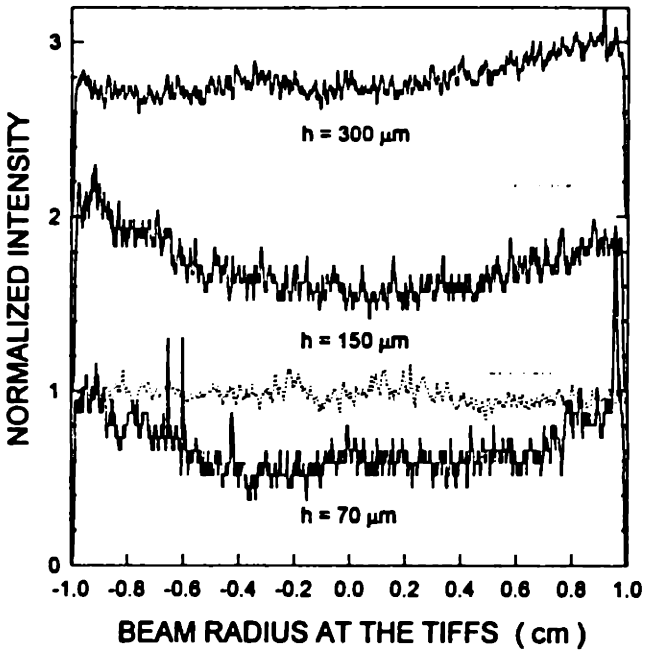

Figure 6.17: Absorption beam profile measurements.

moderately high, $\sim 5 \times 10^{21}$ cm^{-4}. This value for the density gradient is one-half the value for which beam refraction effects would reduce EUV gain. These deleterious effects were described in chapter 3. The results described in this section were obtained during the last two weeks of experiments, and are preliminary. Further experiments should be conducted to verify these results.

The TIFFS was used to make three beam profile measurements for three distances above the target surface. The input slit width for the TIFFS was 50 μm. The pump-laser was configured for 210 ps pulses, and the pump-laser pulse energy was 1 J. Emission from the H-like B 2p-1s line was recorded directly on Polaroid 107 film. The soft x-ray dose was adjusted so that the film was biased in its linear region. The resulting spectral lines were scanned with the densitometer to obtain beam profiles.

Beam profiles at three heights above the target surface are shown in figure 6.17. Two shots have been averaged at each height, and the data has been normalized and shifted. Two traces show an intensity depression at the beam center, which is expected for an absorptive line. The third trace, taken 300 μm above the target, shows a smaller depression which is not centered. A fourth beam profile measurement was taken of optically thin emission from a Ti plasma, and is shown in the figure as the dotted trace.

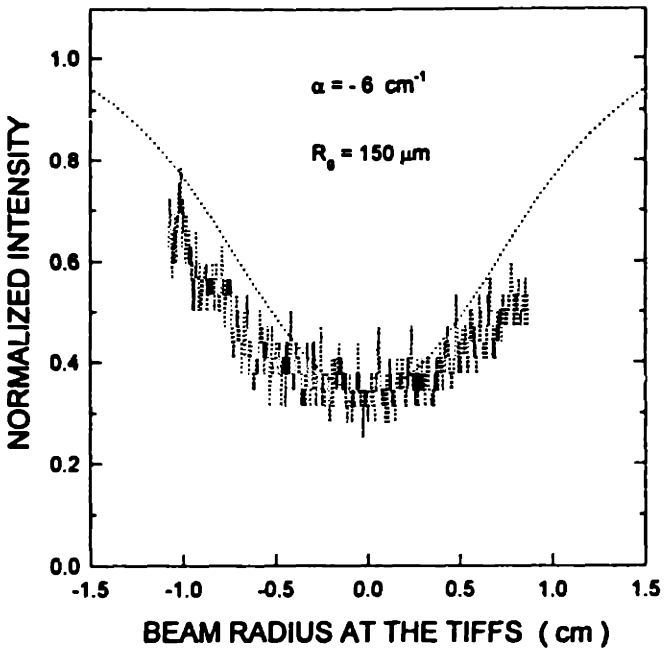

Figure 6.18: Measured and calculated absorption beam profile from a BN plasma. The measured profile was obtained 150 μm above the target surface.

The intensity depressions observed in figure 6.17 qualitatively agree with the predictions of chapter 3 for an absorptive line. The reduction in the depression at 300 μm is expected, since the ion density is lower further from the surface. The absorption coefficient for a Doppler broadened line is related to the ion density through the relation [5, page 39]

$$\alpha = r_0 N_i \lambda f_{ol} \sqrt{\frac{\pi M c^2}{2 k_B T_i}} \tag{6.1}$$

where λ is the transition wavelength, N_i is ion density, M is ion mass and T_i is ion temperature. As the plasma expands and cools, the ion density will decrease and the 2p-1s line absorption should also decrease.

A beam profile calculated with the program ASE1 is compared with the measured profile 150 μm above the target in figure 6.18. Parameters used for the calculated beam profile are shown in the figure. Since the TIFFS samples only a small portion of the beam, an accurate fit is difficult to achieve. Also, the discrepancy of the fit may be due to the Gaussian beam approximation used in the program ASE1. A rough estimate of the absorption coefficient from this data is $\alpha \approx -6$ cm^{-1}.

The TIFFS was also used to make intensity *vs* plasma length measurements of the H-like B 2p-1s line. The constant dose method was used for these measurements. Line intensities were

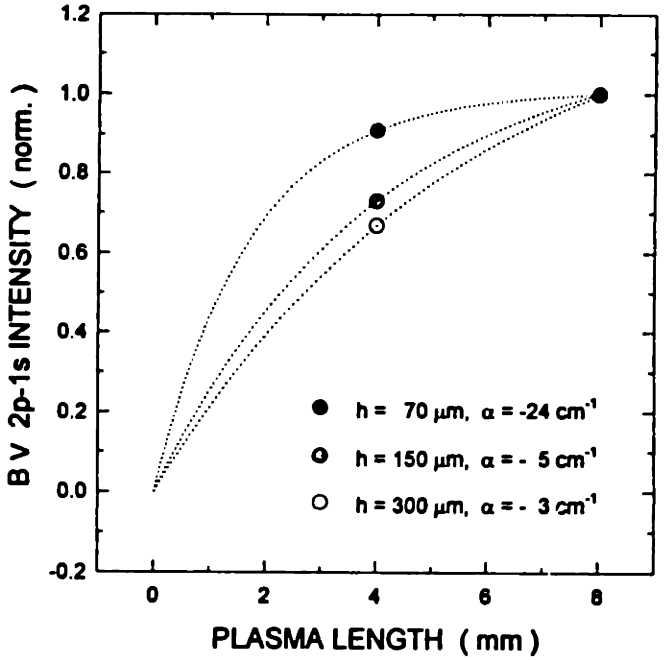

Figure 6.19: Intensity *vs* plasma length measurements of the H-like B 2p-1s line. Measurements were made at three heights above the target surface.

recorded for 8 mm and 4 mm plasma lengths at each of the three heights above the target surface. Line intensities were determined by scanning the spectra at the center of the intensity depression, which corresponded to the EUV laser axis. This minimized contribution from off-axis emission. Two shots were averaged at the 8 mm length and four shots were averaged at the 4 mm length.

The I *vs.* L measurements are plotted in figure 6.19. The results agree qualitatively with the beam profile measurements: $|\alpha|$ increases with decreasing distance from the target surface. The measurement at 150 μm is in good agreement with the value obtained from the beam profile measurement, considering the small number of pump-laser shots averaged. Better estimates of the absorption coefficients could be obtained by averaging more shots, and recording intensities for more plasma lengths.

The magnitude of the absorption coefficient for the h = 150 μm measurement is surprisingly low. Using a value of 6 cm^{-1} in the expression 6.1 and assuming an ion temperature of 20 eV, a value for the ion density N_i can be determined. With λ = 49 Å and f_{ol} = 0.42 [31], a value of 3.8×10^{15} cm^{-3} is estimated for the ion density. This value corresponds to an electron density of 5.6×10^{16} cm^{-3}. Assuming that the plasma's critical surface is about 50 μm above the target

surface and the profile is exponential, the corresponding value for the density gradient is about 5×10^{21} cm^{-4} near the gain region. This value implies that the gain region is less than 50 μm wide. At about 10^{22} cm^{-4} beam refraction effects begin to reduce the effective length of the plasma column; see figure 3.3 in chapter 3.

6.5 Ionization Studies

The final set of laser-driven plasma experiments was designed to determine the ionization stages achieved by candidate lasants. Ionization studies were carried out for eight elements, of which seven were found to be suitable for subsequent gain studies. Results from these studies indicate that an electron temperature of about 200 eV is achieved in our laser-produced plasmas.

For the ionization studies, the pump-laser was operated in long pulse mode and pulse energies were varied between 250 mJ and 1000 mJ. One to three pulses were used to excite the plasma, and the plasma length was typically 5 mm. These pumping conditions were chosen to simulate conditions for subsequent gain studies. 210 ps pulses were used because previous experimental results, section **6.3.2**, indicated that long pulses heated the plasma more efficiently.

The TIFFS was used to record soft x-ray emission from each of the elements, and these spectra were used to determine ionization stages achieved in the plasmas. In a few cases, the S/ICGS was also used to record EUV emission and verify or determine the presence of a particular ion. A 50 μm wide slit was used for both spectrometers. Soft x-ray and EUV wavelength tables [21,28,31,61] were consulted, and the programs HARADA and NRL2 were used to identify spectral lines.

Three ionization spectra have been selected from the data for presentation. The spectra correspond to C, Al, and Ti plasmas. C and Al are two candidate recombination lasants, which require H-like and Li-like ions, respectively. Ti is a candidate Ne-like collisional lasant. The necessary ionization stages have been identified from the spectra.

Two first-order spectra of carbon are shown in figure 6.20. One and two pulses have been used to obtain the spectra, and the pulse energy was 1000 mJ. Soft x-ray emission has been recorded from a region 180 μm above the target surface. A small increase in the ratios R_3 and R_4, H-like C (3-1)/(2-1) and (4-1)/(3-1), can be observed which indicates a hotter plasma for the two-pulse case. The value of R_0, (H-like C 2-1)/(He-like C 2-1), is about 7.2, which is more than twice the value recorded for boron. The difference cannot be attributed to film response.

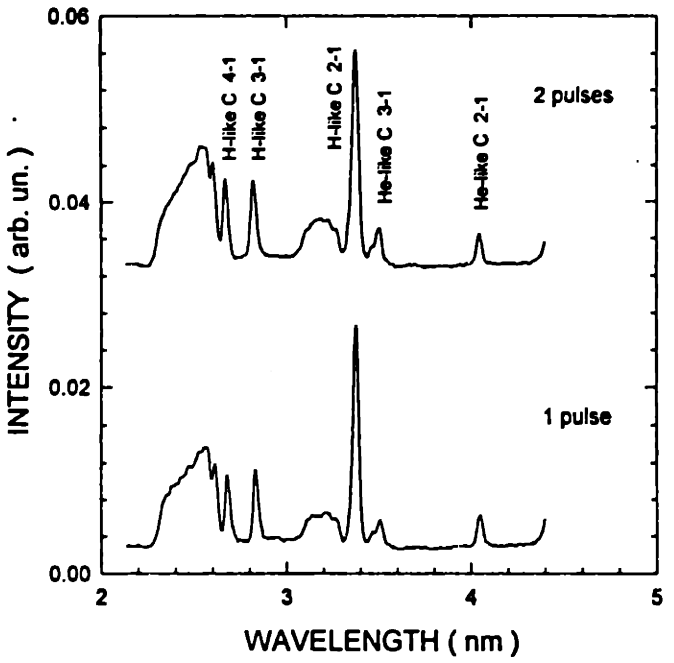

Figure 6.20: Ionization spectra for carbon.

This suggests that the energy couples more efficiently to the carbon slab target. The spectra clearly show abundance of H-like C and ionization of H-like C. The required ionization potential of 490 eV for H-like C has been achieved with the first pump-laser pulse.

Three spectra, obtained from an aluminum plasma, are shown in figure 6.21. The pulse energy has been doubled for two of the spectra as noted in the figure. Emission has been recorded from a region 180 μm above the target surface. The lines marked **a** - **e** are observed in second order, while the lines **f** - **h** are first order lines. The line identifications are noted in the figure caption. As the pulse energy is increased to 1000 mJ, the presence of Li-like Al is detected. The ionization potential of Be-like Al is 399 eV. One pump-laser pulse of 1000 mJ produces Li-like Al.

Soft x-ray spectra of titanium is shown in figure 6.22 for three pulse energies. One pump-laser pulse has been used to excite the plasma. Ne-like Ti lines, marked **D** and **F**, are observed in each spectrum. The ionization potential for Na-like Ti is 292 eV, and the excitation energy of the observed lines is about 500 eV. The results are surprising since the estimated pump-laser intensity is only 6×10^{11} W cm^{-2} for the 250 mJ measurement.

Other lines in the spectra of figure 6.22 have been identified tentatively as belonging to higher ionization stages of Ti. If the identification is correct, this would suggest a very high

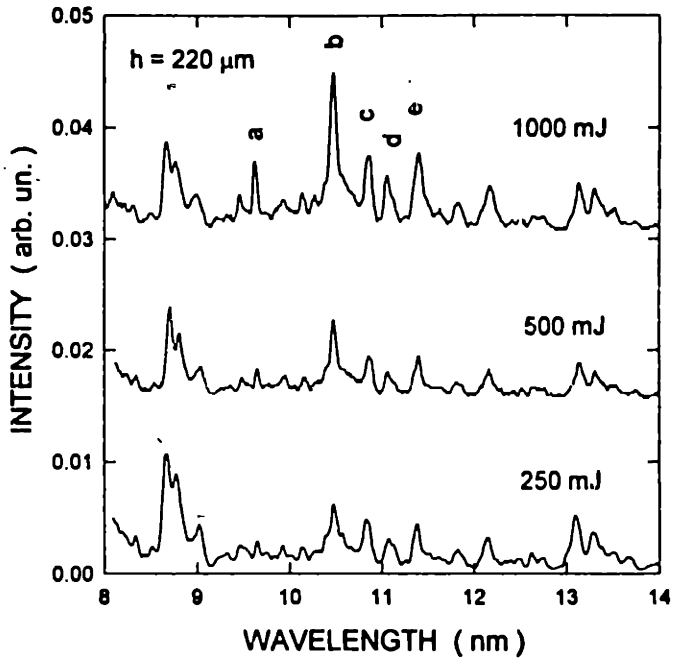

Figure 6.21: Ionization spectra for aluminum. Spectral lines have been identified as a: Li-like Al 3p-2s (4.83 nm), b: Li-like Al 3d-2p (5.23 nm), c: Li-like Al 3s-2p (5.42 nm), d: Be-like Al 3d-2p (5.54 nm), e: Be-like Al 3d-2p (5.74 nm), f: N-like Al 3s-2p (8.69 nm), g: N-like Al 3s-2p (8.80 nm), h: N-like Al 3s-2p (9.05 nm). Identifications are from reference [28].

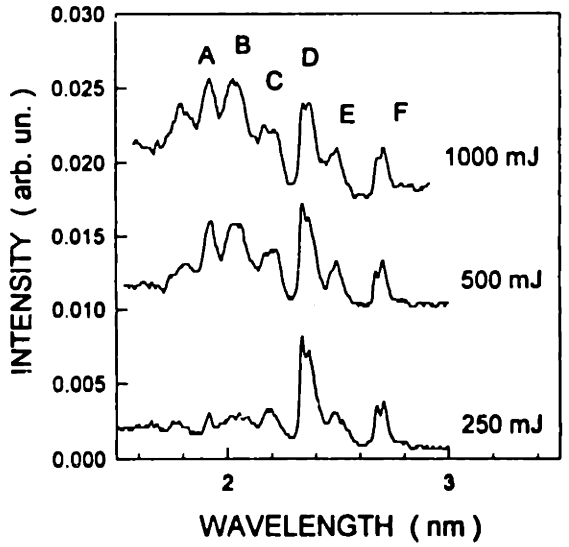

Figure 6.22: Ionization spectra for titanium. Ne-like Ti lines are identified as D: 3d-2p (2.34, 2.37 nm) and F: 3s-2p (2.67, 2.70 nm). Other lines are tentatively identified as A: N-like Ti 3d-2p (1.95 nm), B: O-like Ti 3d-2p (2.04 nm), C: F-like Ti 3d-2p (2.19 nm) and E: F-like Ti 3s-2p (2.45 nm). Line identifications are from reference [21].

Table 6.1: Summary of Ionization Studies

Element	Ionization Stage		E_i	I_p
	Observed	Required	(eV)	($\times 10^{11}$ W cm^{-2})
B	H	H	259	2
C	H	H	392	6
N	He	H	552	15
F	He	Li	185	6
Mg	Li	Li	328	12
Al	Li	Li	399	12
Ca	F	Ne (Na)	591	12
Ti	F	Ne (Na)	787	12

electron temperature. The ionization potential of F-like Ti is 861 eV. Some of the lines may be due to oxygen on the surface of the target. He-like O lines occur at 1.86 and 2.18 nm, and the ionization potential of Li-like O is 138 eV. However, similar results have been obtained for calcium, which would support attribution of the lines to higher ionization stages of Ti. The lines may also be due to dielectronic recombination satellites from Na- or Ne-like ions [105]. Higher resolution spectroscopy in this wavelength region would determine the actual ionization stages achieved.

Results from ionization studies are summarized in table 6.1. The table lists the elements used, and the ionization stages achieved. The ionization potential, E_i, required for the listed ionization stage is also listed. The estimated pump-laser intensity, I_p, for a 210 ps pulse is also given. The listed intensity is the lowest value for which the reported ionization stage is readily observed. In some cases, such as for Ti and Ca, results suggested that higher ionization stages can be achieved. Conservative results are given until further spectroscopic measurements can confirm the presence of higher ionization stages.

The results from the ionization studies are plotted on the graph of figure 6.23. To estimate the electron temperature from the ionization spectra, one-third the value of E_i in table 6.1 is taken as the average value of the peak electron temperature. The graph also shows the predicted

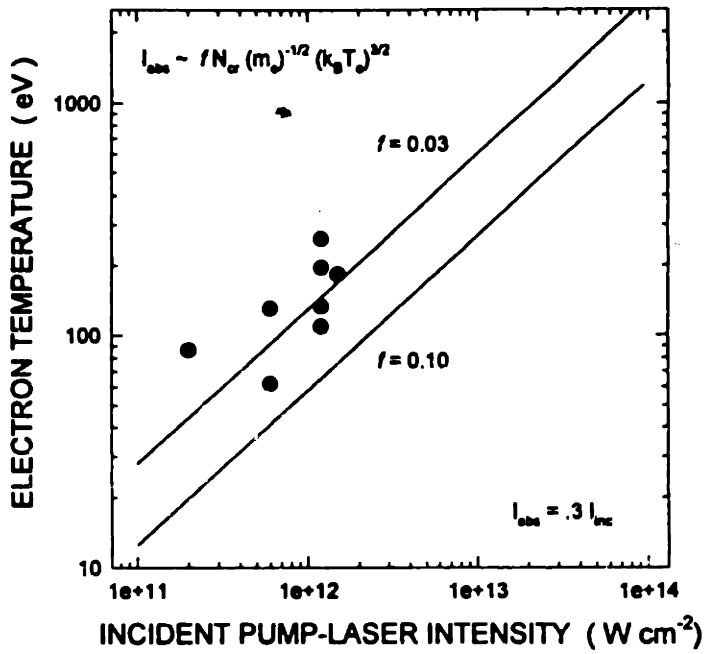

Figure 6.23: Inferred electron temperature *vs.* incident pump-laser intensity. Inferred temperatures from the ionization studies, plotted as points, are compared with predicted temperatures for two values of the flux limiter.

relation [19] between the absorbed pump laser intensity and the peak electron temperature for two values of the flux limiter f. The data suggests that the lower value of $f \approx 0.03$ more accurately predicts the electron temperature for the 210 ps pulses used to excite the plasmas.

From the achieved ionization stages, and short wavelength transitions, we estimate the electron temperature in the 5 mm long plasmas to be around 200 eV with 210 ps, 1000 mJ pump-laser pulses. The results of the ionization studies indicate that all elements, except nitrogen, are suitable for further gain studies. Ti and Ca can be used as Ne-like collisionally pumped or Na-like recombination pumped amplifiers. EUV amplification experiments will be summarized in the next chapter.

Chapter 7

Extreme Ultraviolet Gain Measurements

7.1 Introduction

Results from extreme ultraviolet amplification experiments are summarized in this chapter. With suitable elements identified and the pump-laser configured to produce the hottest plasmas, gain studies have been conducted for nine EUV lasants. A "gain measurement algorithm", described in the next section, has been followed for each lasant surveyed. Sample spectra, in the vicinity of candidate lasing transitions, and results of gain measurements are presented in the following sections. A small signal gain-length product greater than 1.6 has not been observed in these experiments.

7.2 Gain Measurement Algorithm

For the majority of gain experiments, the pump-laser was configured to deliver 210 ps pulses with energies up to 3 J per pulse. The pump-laser performance was also found to be the most consistent in long pulse mode. A transverse pump-laser beam profile, measured with a CCD array at the location of the target, is shown in figure 7.1. To maintain consistency for all gain experiments, a gain measurement algorithm was followed for each of the lasants surveyed. The basic algorithm is shown in table 7.1.

The first step of the algorithm was performed daily, and usually took about two hours to complete. However, the pump-laser required two hours to warm-up before system checks could be made. Target alignment was checked daily with a diode laser beam, which was made normal to the target surface after completion of the target alignment procedure described in section 4.6.

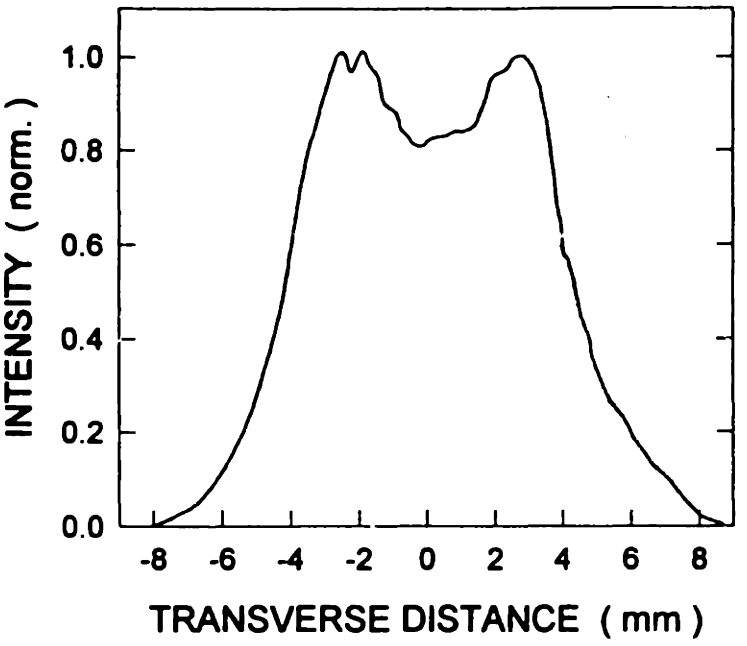

Figure 7.1: Transverse profile of the pump-laser beam. The profile was measured with the pump-laser system configured to deliver 210 ps pulses.

Table 7.1: Gain Measurement Algorithm

1. Preliminary system checks.
    - Load and align target.
    - Check pump-laser alignment and output.
2. Identify candidate lasing line with the S/ICGS.
    - Use C or BN calibration sources to determine correct spectral range.
    - Reduce length of lasant plasma until lasing line appears.
    - Bias signal to the linear region of the film.
3. Observe emission from different regions of the plasma.
    - Scan the target position to identify the plasma region where the lasing line is most intense.
4. Vary pump-laser pulse energy.
    - Scan pulse energy to see if a threshold energy exists for the lasing line.
    - Make minor adjustments to target position to track pulse energy.
5. Conduct constant-dose gain measurements.
    - Make several measurements at and near the location of peak line emission.

The pump-laser's mode-locked performance and energy output were checked daily. Additionally, pulse energies were recorded for nearly every shot. Also, pump-laser beam burn patterns were taken every day to assure a quality line focus on the target.

Candidate lasing transitions were identified using the S/ICGS, and consulting spectroscopic tables. Because the S/ICGS had a limited spectral range, C or BN calibration sources were used to position the spectrometer grating for line identification. After the grating was positioned, the C or BN source enabled accurate determination of lasing transition wavelengths to within ±0.05 nm. Normally, 8 mm long plasmas were first studied. If the lasing transition was not observed, the plasma length was reduced with a cylindrical lens before the target chamber.

As discussed in chapter 6, the intensity of spectral lines changed with distance from the target surface. Consequently, the target position was scanned so that the plasma region of most intense emission was located before the S/ICGS input slit. For all lasants surveyed, this region was located within a range 150 to 500 μm above the target surface.

With the target positioned properly, the pump-laser pulse energy was varied from 250 mJ up to 3 J. The line intensity was studied for a "threshold effect", a nonlinear increase above a threshold pump-laser energy. Such an effect could indicate lasing action. When the pump-laser energy was increased, the target was moved up to 100 μm to track the region of most intense emission. Also, the microchannel plate gain in the S/ICGS was reduced as pumping energy was increased, so that the EUV dose remained in the film's linear region.

With the target positioned, and pump-laser pulse chosen to produce the brightest lasing line emission with respect to surrounding spontaneous emission, constant-dose gain measurements were made. Typically, line intensities were recorded for 8 mm and 4 mm plasma lengths, and six shots were taken at each length. Measurements were made for several regions of the plasma near the region of brightest emission. In some cases, measurements were made up to 200 μm away from the region of brightest emission. In some measurements, the target was rotated up to 5 mrad to compensate for possible refraction effects. Recorded spectral data was scanned with the densitometer and analyzed for evidence of amplification.

After investigating several candidate lasants, following the gain measurement algorithm, the experimenter became calibrated to normal line intensities emitted by the laser-produced plasmas. Only one line appeared to be significantly brighter than any other line observed. The brightest emission observed was from a doublet 3d-2p transition in Li-like C at 38.4 nm. Because of

the long lifetimes of their lower states, these transitions cannot have gain under our pumping conditions. The Li-like C emission at 38.4 nm may serve as a comparison for a future observation of gain.

7.3 Results From Recombination Experiments

Results from gain measurements with H-like, He-like, Li-like and Na-like recombination lasants are presented in this section. For most of the experiments a single pump-laser pulse was used to excite the plasma. In many of the recombination experiments, measurements were made with a bare target and then repeated with a steel blade mounted near the target surface, as shown in figure 4.10 of chapter 4. In some experiments, excitation with two pump-laser pulses was also tried.

EUV spectra, recorded in the region of the lasing lines, will be presented along with samples of constant-dose *I vs. L* measurements. The spectra for which the lasing line appears most intense, have been chosen for presentation. Experimental conditions will be noted in the figures.

7.3.1 H-like Lasants

Gain studies were carried out for H-like B and C. Of all research time devoted to gain experiments reported in this study, the fraction of time devoted to H-like experiments is estimated to be about 80 %. Greater effort was expended for the H-like lasants because H-like C was shown to lase at low pump-laser intensity and fluence [14], which were accessible by our system. An estimated two hundred *I vs. L* measurements were made for H-like C and B under different pumping conditions. Many measurements were made with the S/ICGS used in streaked mode [2], for which a gain of $3.7 \pm .2$ cm^{-1} was reported. For previous experiments [2], the constant-dose gain measurement technique was not used. Accordingly, those results are believed to be in error. The results reported here are most recent and most accurate.

A lasing line spectra and an accompanying *I vs. L* measurement for H-like B are shown in figures 7.2 and 7.3. The candidate 3d-2p lasing line is marked with a star in the spectrum, and nearby lines are identified in the figure caption. The *I vs. L* measurement shows no gain for the lasing line. A steel blade was located 500 μm above the target surface, and emission from a region 300 μm above the target was recorded. The pump-laser intensity at the target was 1.5×10^{12} W cm^{-2}.

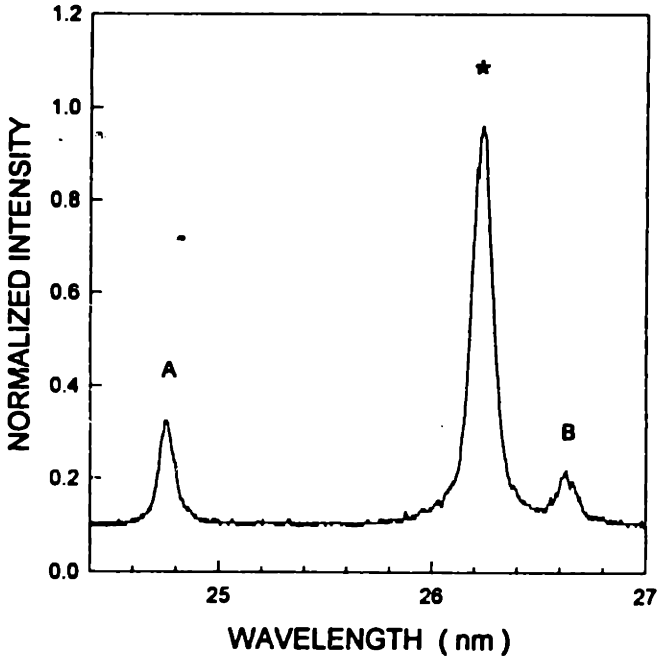

Figure 7.2: H-like B spectrum. Line identifications are *: H-like B 3d-2p (26.24 nm), A: Li-like N 3d-2p (24.77 nm), B: Li-like N 3s-2p (26.62 nm).

The Li-like N 3d-2p line in figure 7.3 appears to be optically thick with an estimated absorption coefficient of $\alpha \approx -3$ cm^{-1}. A significantly larger optical depth is expected for this ground state transition. Since the S/ICGS has been used for this measurement, angle-averaged off-axis emission from the plasma will reduce the apparent optical depth of this line. Figures 3.10 and 3.11 of chapter 3 show the effects of off-axis emission and adjacent optically thin emission on the detected intensity growth of absorption lines. The actual optical depth of the Li-like N 3d-2p line cannot be determined accurately with the S/ICGS. Since the TIFFS does not integrate appreciable off-axis emission, optical depths are determined more accurately with this spectrometer. The optical depth measurements reported in section **6.4.3** have been made with the TIFFS.

Similar graphs for H-like C are shown in figures 7.4 and 7.5. Both lines were found to be optically thin. A steel blade was located 500 μm above the target, and emission was recorded from a region 220 μm above the target. The pump-laser intensity was $I_p = 6.0 \times 10^{12}$ W cm^{-2}. The reflectivity of the concave grating used in the S/ICGS was estimated to be a factor of 20 lower at 18.2 nm than the reflectivity at 26.2 nm. Consequently, a high gain setting was required for the microchannel plate used in the S/ICGS. Because of ion feedback in the microchannel plate, it was difficult to obtain a clean spectrum.

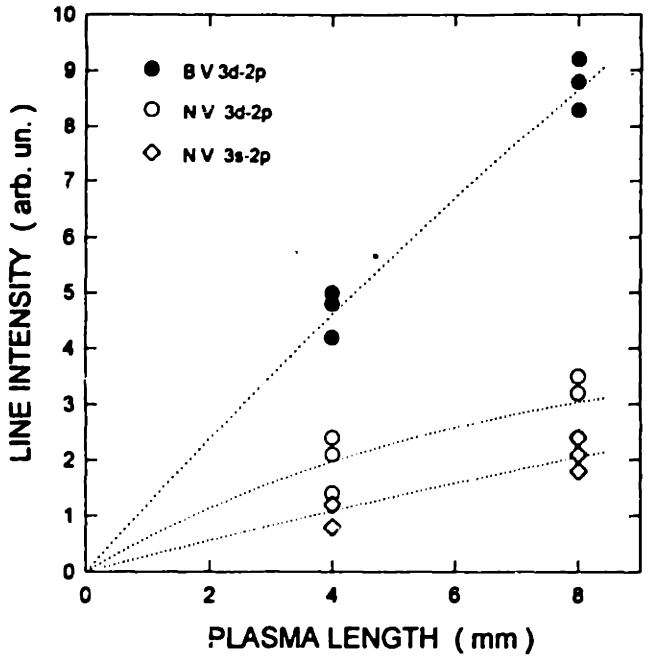

Figure 7.3: H-like B I *vs.* L measurement.

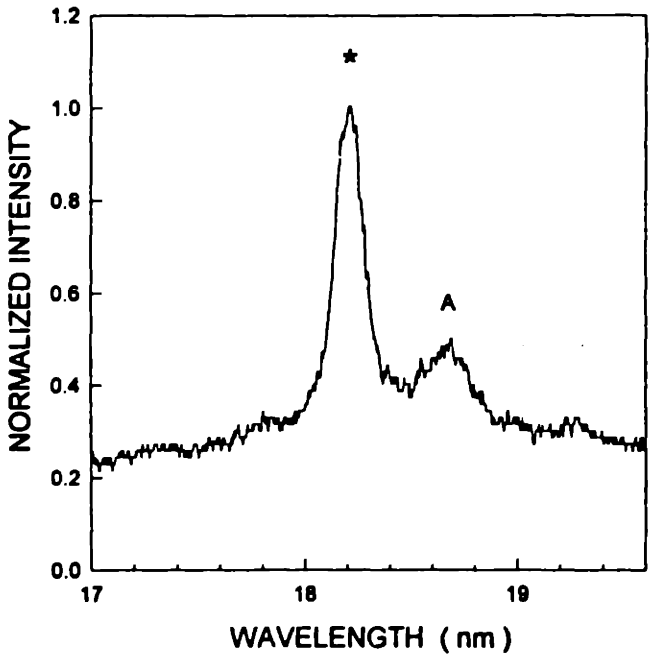

Figure 7.4: H-like C spectrum. Line identifications are *: H-like C 3d-2p (18.22 nm), A: He-like C 4d-2p (18.67 nm)

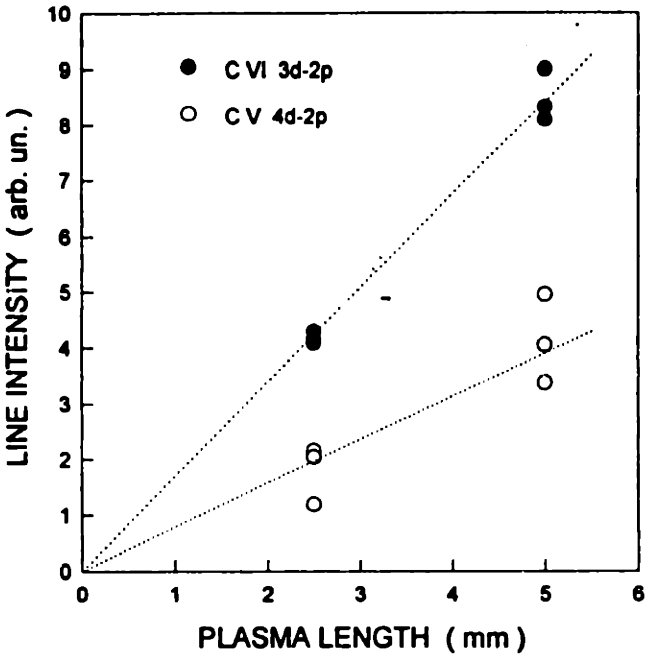

Figure 7.5: H-like C *I vs. L* measurement.

7.3.2 He-like Lasants

Preliminary gain measurements were made for He-like B and C, before the constant-dose gain measurement technique was developed. For these lasants, gain is expected on the 3d-2p singlet transition. Lasing line spectra from $\sim$ 1 mm long plasmas were obtained for each element. These were compared to spectra from a 5 mm long C plasma and an 8 mm long B plasma. The pump-laser pulse length and energy were 140 ps and 1300 mJ. The carbon spectra are shown in figure 7.6.

For carbon, the He-like 3d-2p singlet transition at 26.72 nm and the He-like 3d-2p triplet transition at 24.87 nm could be recorded simultaneously with the S/ICGS. For He-like B, the analog transitions were at 41.88 nm and 38.50 nm, and could not be recorded simultaneously within the S/ICGS spectral window. The transition rates and oscillator strengths for the singlet and triplet transitions are nearly equivalent. The presence of gain would be detected as an increase in the ratio of the singlet line intensity to the triplet line intensity for the 5 mm plasma length. Such an increase was not observed in C or in He-like B. Further gain studies with these elements were not pursued.

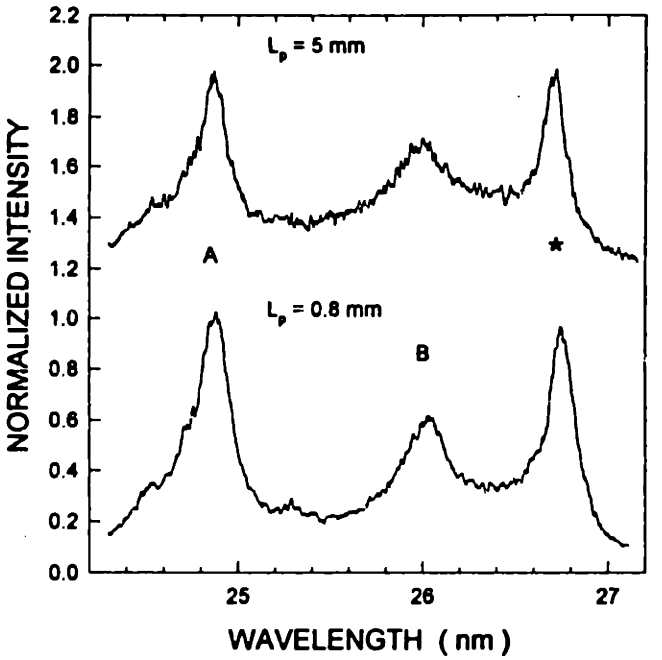

Figure 7.6: He-like C spectra. The lower trace is from a $\sim$ 1 mm plasma and the upper trace is from a 5 mm long plasma. Line identifications are *: He-like C 3d-2p singlet (26.72 nm), A: He-like C 3d-2p triplet (24.87 nm), and B: Li-like C 5d-2p (25.95 nm).

7.3.3 Li-like Lasants

Gain measurements were carried out for Li-like F and Mg. Because of its low ionization potential, Li-like F was studied more extensively than Mg. Candidate lasing transitions were identified in both elements, although no gain characteristics were detected for either lasant.

The low ionization potential of Li-like F, 185 eV, was easily achieved with our pump-laser system. The candidate 4f-3d lasing transition was readily observed at low pump-laser intensity, as shown in figure 7.7. For this measurement, the pump-laser intensity was 3.0×10^{11} W cm^{-2}. At higher pumping intensities, the intensity of the 4f-3d line was observed to extinguish, which indicated over ionization to the He-like stage.

The length of the plasma was increased to 20 mm for the Li-like F gain measurements. A blade was located 650 μm from the target surface, and emission from a region 330 μm above the target was studied. The target consisted of a 1 μm film of CaF_2 deposited on a Si wafer. The peak pumping intensity was 3.0×10^{11} W cm^{-2}.

Results from the constant-dose *I vs. L* measurement is shown in figure 7.8. The data indicates that both Li-like F transitions are optically thin. The Mg-like Ca line appears to be

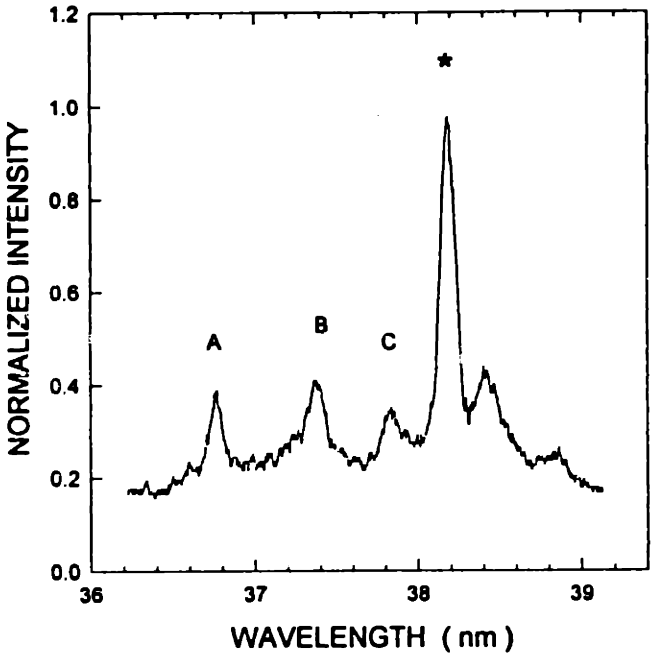

Figure 7.7: Li-like F spectrum. Line identifications are *: Li-like F 4f-3d (38.18 nm), A: Li-like F 4d-3p (36.79 nm) B: Mg-like Ca (37.39 nm), C: Mg-like Ca (37.81 nm). Ca lines are identified from reference [78].

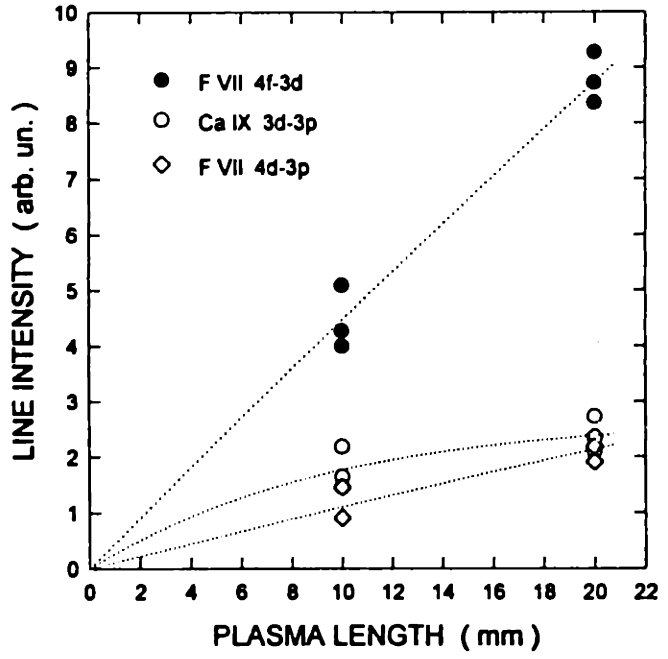

Figure 7.8: Li-like F I *vs.* L measurement.

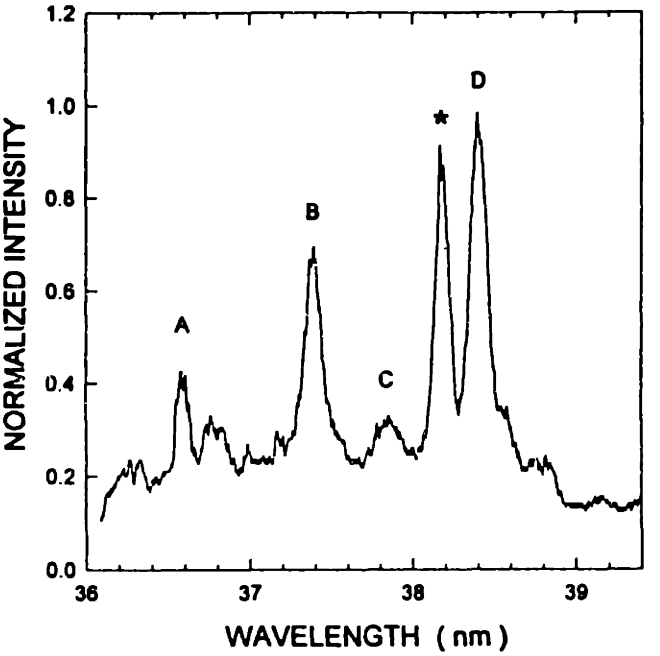

Figure 7.9: Li-like F spectrum at low pumping intensity. The line marked D has been observed in other experiments [78] but has not been identified.

optically thick.

Under different pumping conditions, all lines were observed to be absorptive. The plasma length was reduced to 8 mm and the pump-laser intensity was reduced to 8.9×10^{10} W cm^{-2}. Emission was observed 200μm from the target surface. The recorded spectrum and the *I vs. L* measurement are shown in figures 7.9 and 7.10. Six shots were overlayed on the film for the 4 mm length intensity measurement and two sets of three shots were recorded for the 8 mm length.

In the spectra of figures 7.7 and 7.9, the intensity ratio of the Li-like F 4f-3d to 4d-3p lines appears to be near an equilibrium value of 2.74. Because of nonuniform gain across the microchannel plate and film nonlinearity, the line ratio is enhanced which suggests the presence of gain. The *I vs. L* measurements clearly indicate the absence of gain. To determine the line ratio accurately, a constant-dose measurement is required.

Li-like Mg was studied briefly. Two possible lasing transitions in Mg were within the spectral range of the S/ICGS. The 4f-3d transition at 18.72 nm and the 5g-4f transition at 40.46 nm could be detected separately. The 4f-3d transition was observed from a point plasma with a pump-laser intensity of 3.7×10^{12} W cm^{-2}, but was faintly visible due to the spectrometer's

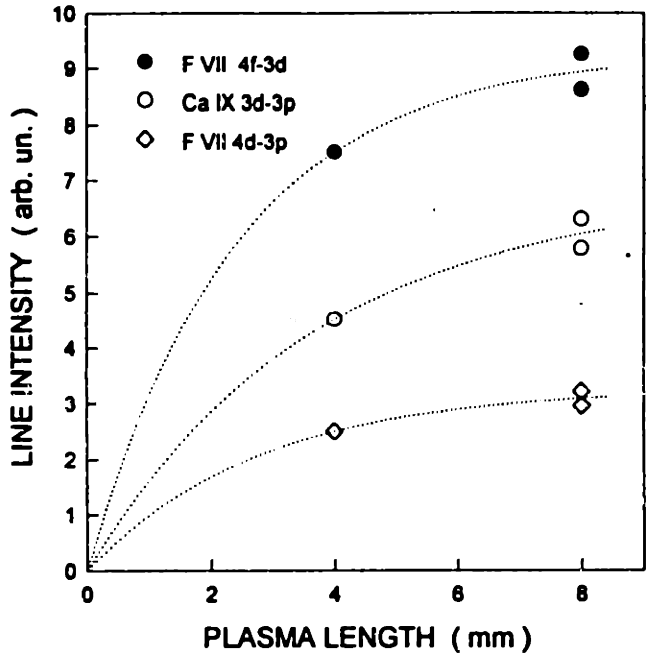

Figure 7.10: *I vs. L* measurement of Li-like F at low pump-laser intensity.

response. Due to ion feedback in the S/ICGS's microchannel plate, the 4f-3d transition could not be detected with an 8 mm plasma. The 5g-4f transition was more easily detected, but required a pump-laser intensity of 4.5×10^{12} W cm^{-2}.

Unlike the 4f-3d transition, the 5g-4f transition is not optically trapped. The 3d level decays directly to the ion's ground state, whereas the 4f level empties into the short lived 3d level. This minimizes reabsorption and repopulation of the lower laser level. Any reduction in optical trapping will increase EUV gain.

A Mg spectrum in the vicinity of the 5g-4f transition is shown in figure 7.11. The candidate lasing transition, marked with the asterisk, is just resolved with the S/ICGS. To the author's knowledge, this is the first observation of this transition. The observed wavelength is 40.43 ± .02 nm, which is near the estimated value of 40.41 nm. The spectrum was obtained from a point plasma to increase spectral resolution.

An *I vs. L* measurement for the 5g-4f transition of Li-like Mg is shown in figure 7.12. The line intensity grows nearly linearly with plasma length. Nearby N-like lines appear to be optically thick. At a pump-laser intensity of 4.5×10^{12} W cm^{-2}, the intensity of the Li-like 5g-4f line is nearly equal to the intensity of the adjacent N-like Mg 2p-2s line. At an intensity of 2.1×10^{13} W cm^{-2} for an 8 mm long plasma, the intensity of the 5g-4f line was about 1.5×

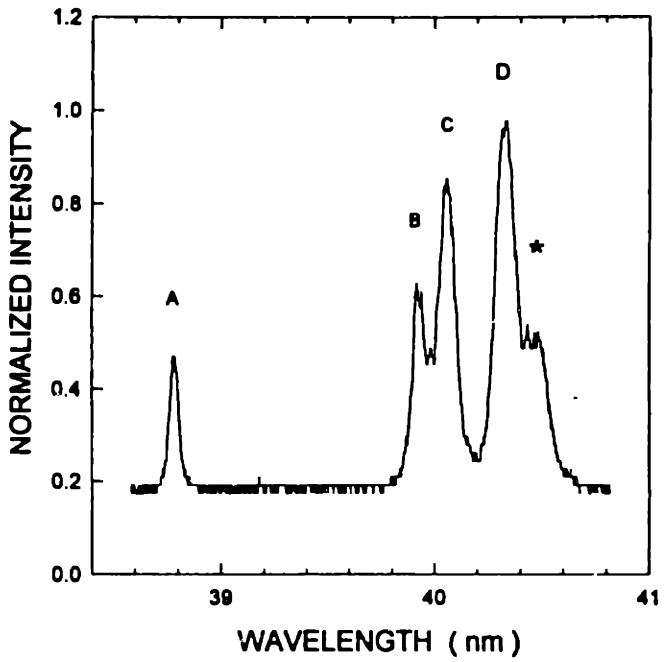

Figure 7.11: Li-like Mg spectrum. Line identifications are *: Li-like Mg 5g-4f (40.43 nm), A-D: N-like Mg 2p-2s (38.80, 39.92, 40.07, and 40.33 nm).

the intensity of the adjacent N-like line. Due to detection difficulties, an *I vs. L* measurement of the Li-like Mg 4f-3d transition has not been made.

7.3.4 Na-like Lasant

The only Na-like lasant investigated was calcium, and the investigation was not as thorough as investigations of other recombination lasants. The first four steps of the gain measurement algorithm were carried out, although extensive *I vs. L* measurements were not made for Na-like Ca. The candidate 5g-4f lasing transition was not prominent in any of the recorded Na-like spectra.

The calcium spectrum in the vicinity of the Na-like lasing line is shown in figure 7.13. The Na-like Ca 5g-4f candidate lasing line has been observed at 40.16 ± .02 nm, and is estimated from atomic energy levels [21] to be at 40.14 nm. To the author's knowledge, this is the first observation of the 5g-4f transition. EUV emission from a region 330 μm above the target surface was recorded, and the pump-laser intensity was 2.4×10^{12} W cm^{-2}.

One *I vs. L* measurement was made for Na-like Ca, and is shown in figure 7.14. The S/ICGS was adjusted so that both the Li-like F 4f-3d and Na-like Ca 5g-4f transitions could be observed simultaneously. Due to nonuniform gain across the S/ICGS's microchannel plate, the intensity

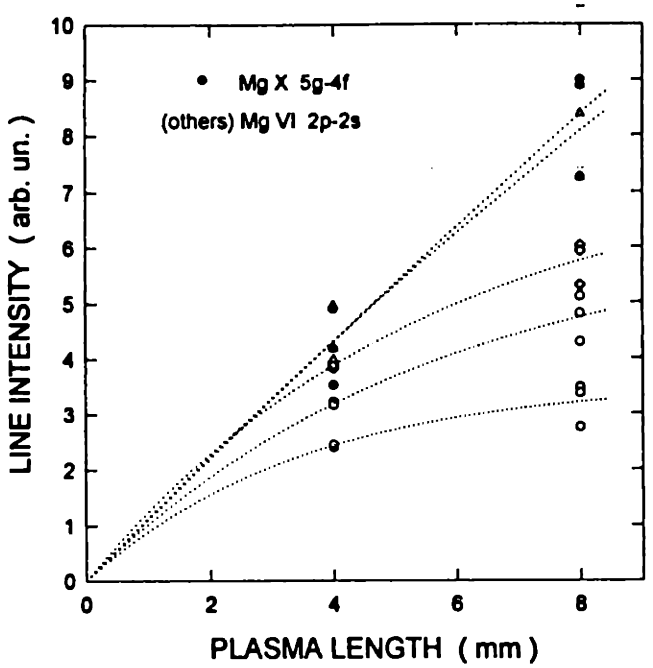

Figure 7.12: Li-like Mg I *vs.* L measurement.

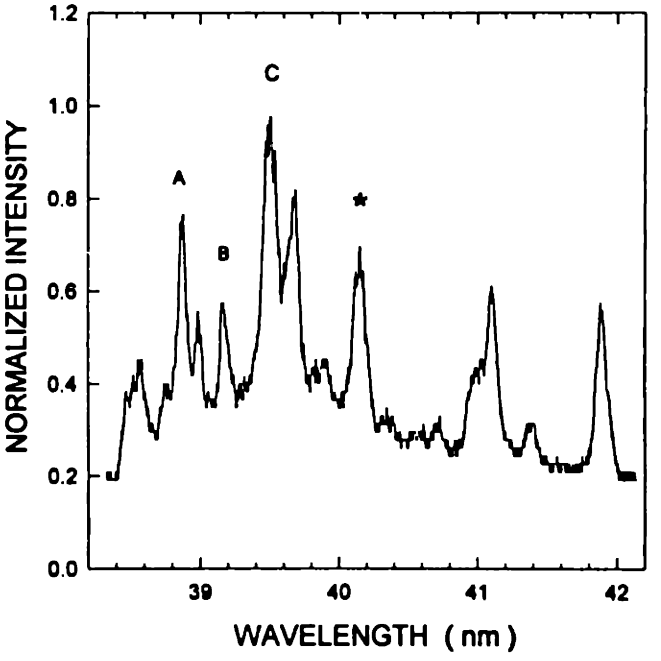

Figure 7.13: Na-like Ca spectrum. Line identifications are *: Na-like Ca 5g-4f (40.16 nm), A: Mg-like Ca (38.88 nm), B: Li-like F (39.18 nm), and C: Mg-like Ca (39.50). Mg-like line identifications are from reference [78].

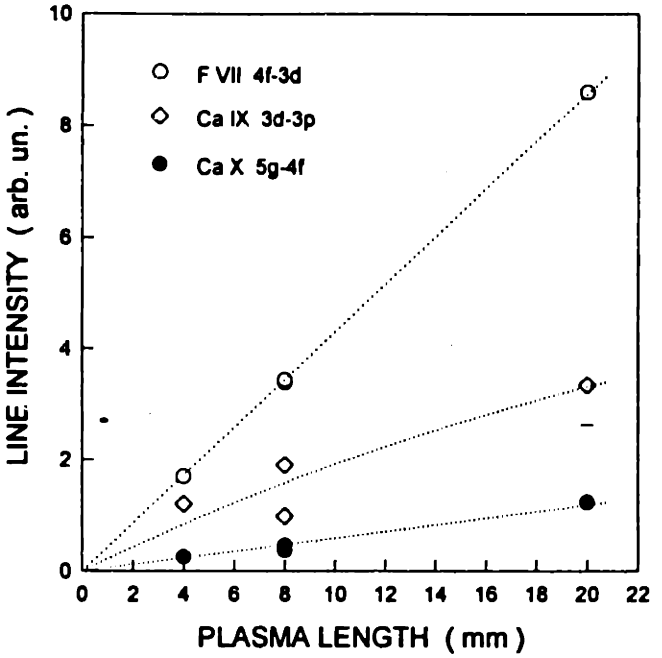

Figure 7.14: Na-like Ca *I vs. L* measurement.

of the Na-like line is recorded as one-half its actual value. The measurement indicates no gain for either of the lasing transitions.

In other measurements, the pump-laser intensity was increased to 3.0×10^{12} W cm^{-2} for an 8 mm plasma, and 4.8×10^{12} W cm^{-2} for a 5 mm plasma. The CaF_2-on-Si target was used for all recorded spectra. The intensity of the Na-like Ca candidate lasing transition did not increase significantly above the intensity of the nearby Mg-like Ca line at 39.50 nm in any of the measurements. This further indicated the absence of amplified spontaneous emission.

7.4 Results From Collisional Experiments

Gain studies were carried out for Ne-like and Ni-like collisionally pumped lasants. Experiments were conducted with the pump-laser configured for 60 ps or 210 ps. One to three pump-laser pulses were used to excite the plasmas, and the pulse energy was increased to the maximum limit sustainable by the slab amplifier. A steel blade was not used for these experiments. For the Ne-like lasants tested, the candidate gain lines were not conclusively identified. For the Ni-like lasant tested, a spectral feature was noted to be in the location of a line identified earlier as a gain transition [1,77]. However, this feature showed no evidence of gain in these recent experiments.

Sample spectra and experimental conditions will be reported in this section. All spectral data was recorded with the S/ICGS, which had a 50μm wide and 100 μm wide input slits located 1.5 cm and 3 cm from the end of the plasma. Carbon and boron nitride were used to calibrate the spectrometer for the different regions of observation.

7.4.1 Ne-like Lasants

Two Ne-like lasants were investigated under a variety of pumping conditions. The two lasants, Ca and Ti, have been shown to lase with higher pumping fluences [58] or higher pumping intensities [71] than used in our experiments. For our studies, 1 μm thick CaF_2-on-Si and 1 μm thick Ti-on-Si targets were used. Pump-laser intensities were varied from about 1.0×10^{11} W cm^{-2} up to 1.8×10^{13} W cm^{-2}. The highest pumping intensities were achieved by reducing the pump-laser pulse duration to 60 ps. Under these pumping conditions, no prominent lasing line was identified for either lasant.

Two spectra from point source Ca plasmas are shown in figure 7.15. EUV emission has been collected from regions at two different heights, h, above the target surface, as noted in the figure. The spectral lines are more easily identified further from the target surface. Continuum emission near the target surface adds considerable background emission to the spectra of higher Z elements. Line identifications are noted in the figure caption [28,78].

The location of the candidate Ne-like 3p-3s J=1-0 lasing line is marked as a dotted line in figure 7.15. The lasing line has been observed at 38.33 nm in laser-driven plasmas [58] and in discharge plasmas [78]. The candidate lasing line is not expected to be observed with our spectrometer from a point plasma, for the reasons discussed in section **2.2** of chapter 2. For longer plasmas, in which amplification occurs, the lasing line may be observed.

Spectral emission from a 5 mm long Ca plasma is shown in figure 7.16. Four different pump-laser intensities were used as noted in the figure. Emission was collected from a region 330 μm above the target surface, and a single 210 ps pump-laser pulse was used to excite the plasma. As the pump-laser pulse energy was increased, a spectral feature near 38.33 nm appeared. This feature, possibly due to the candidate gain line, never became more prominent than shown in the top trace of figure 7.16. An accurate identification of the line required higher resolution spectroscopy, which we have been unable to achieve with the S/ICGS.

Other pumping conditions were used in an attempt to increase the intensity of the candidate

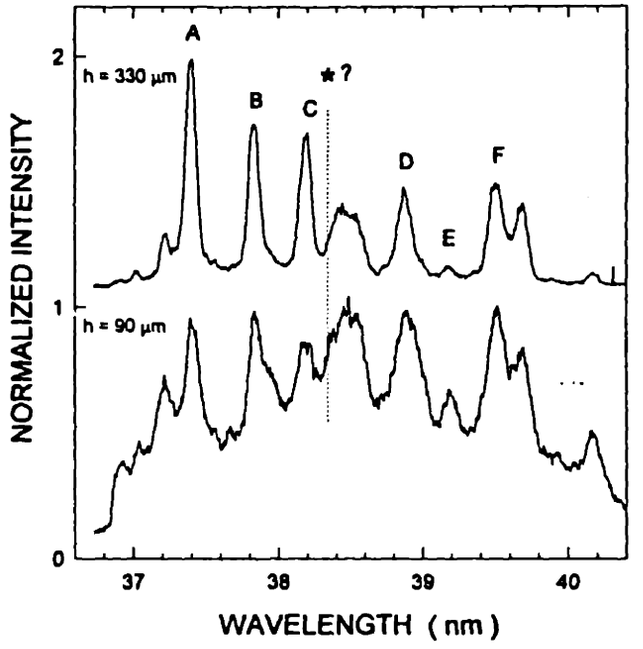

Figure 7.15: Ca spectrum in the vicinity of the candidate Ne-like lasing line. Line identifications are *: Ne-like Ca 3p-3s (38.33 nm), A: Mg-like Ca (37.39 nm), B: Mg-like Ca (37.81 nm), C: Li-like F 4f-3d (38.18 nm), D: Mg-like Ca (38.88 nm), E: Li-like F 4s-3p (39.18 nm), and F: Mg-like Ca (39.50).

Ne-like Ca gain line. Multiple pulses and pulses with higher intensity were also used to excite the plasma. Spectra from two of these measurements are shown in figure 7.17. In one measurement, marked **(a)**, two 210 ps pump-laser pulses separated by 7.5 ns were used to excite a 5 mm long Ca plasma. The pumping intensity of each pulse was 2.4×10^{12} W cm^{-2}. In the other measurement, **(b)**, the pulse length was shortened to 60 ps and two pulses were used to excite an 8 mm long plasma. The peak pumping intensity for **(b)** was 1.1×10^{13} W cm^{-2}.

The feature at 38.33 nm may appear in the spectrum from the 210 ps pulse measurement of figure 7.17, but does not appear to be present for the 60 ps case, **(b)**. If this feature is indeed the Ne-like candidate lasing line, the spectra of figure 7.17 would suggest that long-pulse excitation is preferred. This result would then be consistent with the results of ionization studies, presented in section **6.3.2** of chapter 6. The intensity of the spectral feature at 38.33 nm was not observed to increase significantly above nearby spontaneous emission lines in any of our measurements.

Preliminary gain studies were also carried out for titanium. Lasing in Ne-like Ti has been observed at 32.63 nm in laser-produced plasmas [58,71]. In our experiments, an 8 mm long Ti plasma was excited with 210 ps or 60 ps pulses, and pumping intensities ranged from 3.7 ×

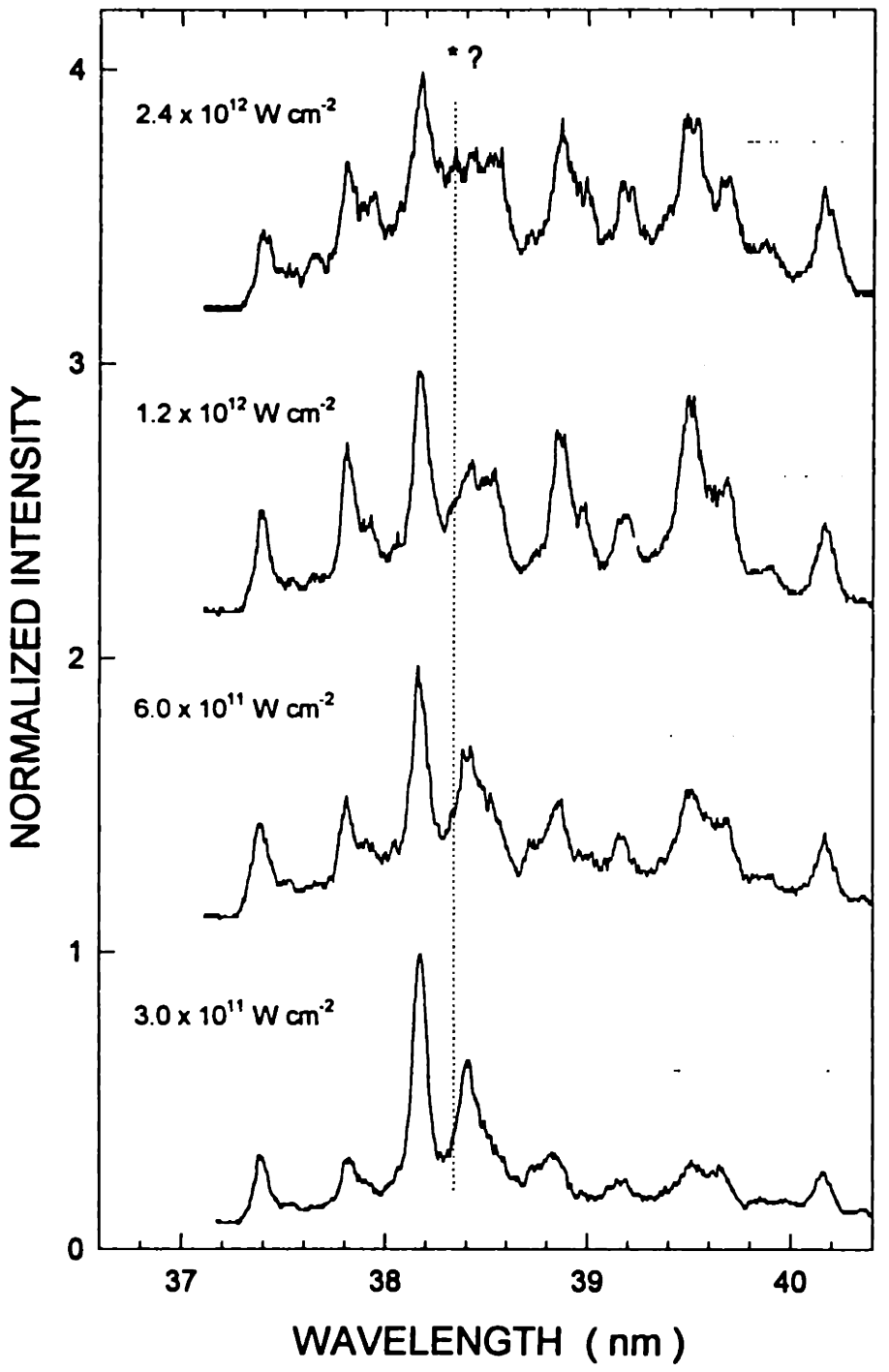

Figure 7.16: Ca spectra for increasing pump-laser intensity. The pump-laser intensity was increased for a 5 mm long plasma. A spectral feature was observed at the location of the candidate Ne-like Ca 3p-3s lasing line, marked with the dotted line. See figure 7.15 for identification of other spectral lines.

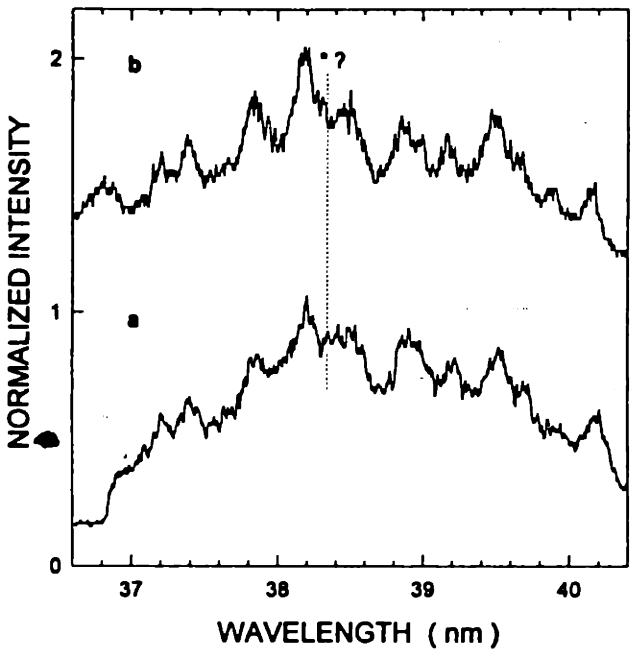

Figure 7.17: Ca spectra. **(a)** 5 mm long plasma excited by two 210 ps pump-laser pulses. **(b)** 8 mm long plasma excited by two 60 ps pulses. The dotted line marks the position of the candidate lasing transition. See text for other details.

10^{11} W cm^{-2} to 1.7×10^{13} W cm^{-2}. The lasing line was not conclusively observed in any of our measurements.

Figure 7.18 shows four Ti spectra recorded under different pumping conditions. These spectra were the best recorded spectra for the pumping intensity used to excite the plasma. The pumping intensities are listed in the figure. A carbon target was used to calibrate the spectrometer in this wavelength region. Spectral lines are identified in the figure caption [78,106,107,108]. The location of the lasing transition at 32.63 nm is marked with a dotted line.

For the spectra **(a)** - **(c)**, 210 ps pulses were used to excite the 8 mm long plasma. One pulse was used for the measurements **(a)** and **(b)**, whereas two pulses were used for the measurement **(c)**. For **(d)**, three 60 ps pump-laser pulses were used to drive the plasma. A prominent line at 32.63 nm does not appear in the high intensity spectra of **(c)** and **(d)**. A spectral feature at or near the candidate lasing transition appears in the low intensity spectra. However, this feature may be due to a line at 32.62 nm, which has been observed in beam-foil measurements [78,108]. Higher resolution spectroscopy is required to determine the presence or absence of the Ne-like Ti 3p-3s J=1-0 lasing line.

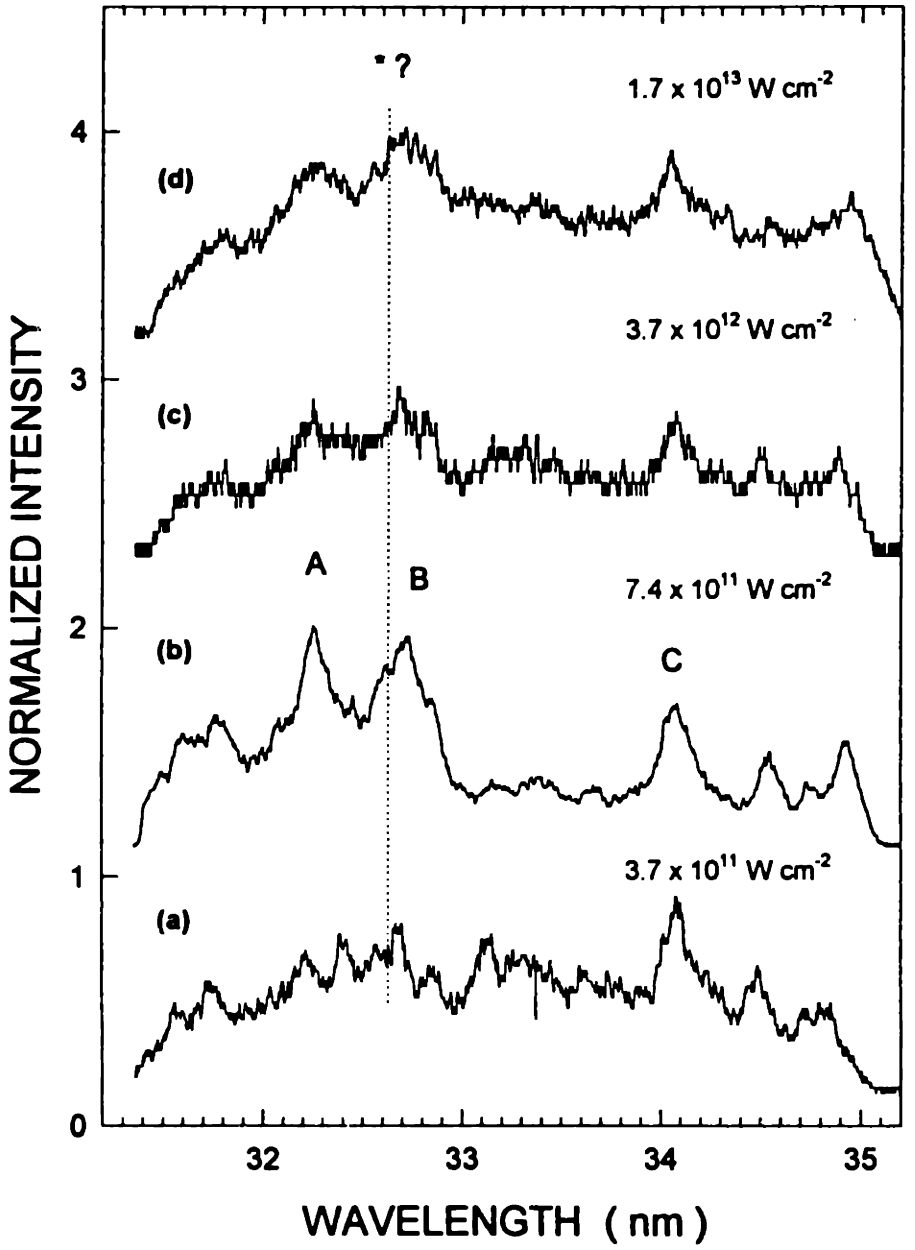

Figure 7.18: Ti spectra from 8 mm long plasmas. See text for details of the pumping conditions. Lines are identified as *: Ne-like Ti 3p-3s (32.63 nm), A: Mg-like Ti 5g-4f (32.25 nm), B: Mg-like Ti 3d-3p (32.72 nm) and C: Mg-like Ti 3d-3p (34.07 nm).

7.4.2 Ni-like Lasant

Earlier investigations with Ni-like Nb indicated the presence of gain in 8 mm [1] and 3 mm [77] long plasmas. These initial investigations were conducted with the S/ICGS used in streaked mode, and *I vs. L* measurements were not made using the constant-dose technique. After the first experiments [1], it was discovered that the pump-laser was mode-locked improperly and that pulse lengths fluctuated from about 20 ps to more than 200 ps. The laser was mode-locked properly for the second set of experiments, and 60 ps pulses were used to excite 3 mm long plasmas. In these experiments, the gain line was not observed with longer plasmas. In both experiments, a spectral feature at $20.42 \pm .02$ nm was reported to show amplification of $2.8 \pm .6$ cm^{-1} [1], and 5 cm^{-1} [77].

A brief study of Ni-like niobium was carried out at the conclusion of EUV gain experiments in an effort to reproduce earlier results. The S/ICGS was used in time-integrating imaging mode, and the pump-laser was configured for 210 ps pulses or 60 ps pulses. Spectra recorded in the vicinity of the candidate gain line showed a spectral feature near 20.42 nm, although this feature did not show evidence of amplification.

Three Nb spectra, from recent experiments, are shown in figure 7.19. Two lines in the spectra have been identified as belonging to Cu-like Nb transitions [1]. The pumping conditions vary for each spectrum. For the lower spectrum, marked (**a**), a point plasma was excited with two 210 ps pulses. The pumping intensity was 1.5×10^{12} W cm^{-2}. For the trace marked (**b**), the plasma was created with two 210 ps pulses, and the pumping intensity was 3.0×10^{12} W cn^{-2}. For (**c**), two transverse beams were used to excite the plasma, and each beam had two 60 ps pulses. The estimated pumping intensity was 9.7×10^{12} W cm^{-2} for (**c**).

In figure 7.19, the traces (**a**) and (**b**) show a spectral feature near 20.42 nm. In the point plasma of (**a**), the feature appears at $20.45 \pm .02$ nm. This feature was not observed in earlier measurements for point source plasmas of Nb [1]. The feature is also apparent in the 8 mm long Nb plasma of (**b**), but shows no evidence of amplification. For the shorter pulse, higher intensity measurement of (**c**), the spectral feature is not observed, and the prominence of the Cu-like lines is diminished. The short pulse result also suggests that longer pulses are preferred for low energy laser produced plasmas. Identification of the spectral feature near 20.42 nm as the Ni-like Nb 4d-4p lasing line requires further evidence of amplification or higher resolution spectroscopic measurements.

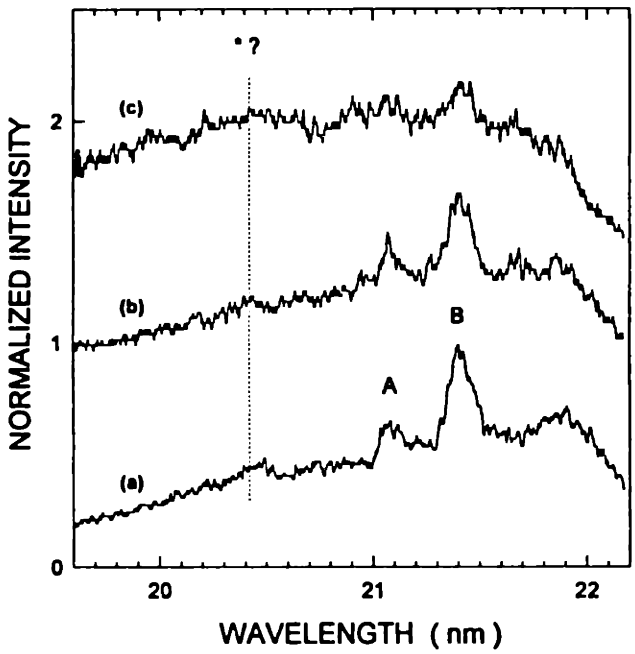

Figure 7.19: Spectra from a laser-produced niobium plasma. See text for details of pumping conditions. Lines are identified as *: Ni-like Nb 4d-4p (20.42 nm), A: Cu-like Nb 5p-4d (21.08 nm) and B: Cu-like Nb 5g-4f (21.41 nm).

7.5 Summary of Gain Studies

A gain-length product greater than 1.6 has not been observed in recent experiments with the MIT table-top EUV system. Both recombination and collisional lasants have been investigated. A gain-length product of 1.6 represents the estimated detection limit of the S/ICGS, which was used for all gain studies. Since gain was not observed with the S/ICGS, gain verification was not carried out with the TIFFS, an instrument with lower spectral resolution.

Several recombination and collisional lasants have been investigated under a variety of pumping conditions. Candidate lasing transitions were identified in most of the recombination lasants. Li-like Al and Na-like Ti recombination lasants were not thoroughly investigated, because lower Z isoelectronic ions showed no evidence of gain. I *vs.* L measurements were carried out for most of the collisional lasants, and these measurements showed no evidence of amplification.

Three collisional lasants have been studied, and spectral features have been observed at the location of the candidate lasing line for two of the lasants: Ne-like Ca and Ni-like Nb. Spectra from highly ionized Ti showed no spectral feature at the location of the gain line for high pumping intensities. A feature at 20.42 nm was observed from a Nb plasma, although the

feature was more prominent from a point plasma than from an 8 mm long plasma, figure 7.19. A spectral feature at 38.33 nm became evident in a 5 mm long Ca plasma as the pumping intensity was increased, figure 7.16. This feature was observed at the location of a previously measured Ne-like Ca 3p-3s gain transition [58,78], and was not observed from a point plasma. Under a variety of pumping conditions, the feature at 38.33 nm did not become a prominent identifiable line in the recorded spectra.

For the collisional gain studies, some experiments were carried out with 210 ps pump-laser pulses and others were conducted with 60 ps pulses. The spectral features at the locations of candidate gain lines for Ne-like Ca and Ni-like Nb were observed when 210 ps pulses were used. Additional spectral data suggested that the plasma appeared hotter with the 210 ps pulses, even though the intensity could be increased three to four times with the 60 ps pulses. This result is consistent with the observations from the ionization experiments, and is not well understood at this time.

To assist the reader, table 7.2 summarizes the shot conditions for each of the recorded spectra reported in this chapter.

Table 7.2: Summary of pump-laser shot conditions.

Spectrum of figure	t (ps)	# of pulses	I_p (x 10^{12} W cm^{-2})
7.2	210	1	1.5
7.4	210	1	6.0
7.6	140	1	4.6
7.7	210	1	0.3
7.9	210	1	0.09
7.11	210	1	4.5
7.13	210	1	2.4
7.15	210	1	1.0
7.16 a	210	1	0.3
7.16 b	210	1	0.6
7.16 c	210	1	1.2
7.16 d	210	1	2.4
7.17 a	210	2	2.4
7.17 b	60	2	11.0
7.18 a	210	1	0.4
7.18 b	210	1	0.7
7.18 c	210	2	3.7
7.18 d	60	3	17.0
7.19 a	210	2	1.5
7.19 b	210	2	3.0
7.19 c	60	2	9.7

Chapter 8

Conclusion

8.1 Summary of Thesis

The objective of this work was to demonstrate a gain-length product greater than 5 at a wavelength near or below 40 nm with a table-top system. Such a demonstration would be considered an essential step toward developing an extreme ultraviolet laser suitable for research applications. This objective has not been achieved with the MIT table-top EUV system. A gain-length product larger than 1.6 was not detected from several recombination and collisional lasants, which were investigated in our experiments. The research summarized in this thesis has followed the directive: based on the premise that EUV gain of more than 5 cm^{-1} can be produced in an 8 mm long laser-produced plasma, carry out a set of experiments to demonstrate, detect and verify the presence of amplification.

Much of the research effort has been devoted to upgrading the pump laser system and determining its optimum operating configuration. The pump-laser has been redesigned to operate in short pulse mode, $\sim$ 20 ps, or long pulse mode, $\sim$ 200 ps. The long pulse mode has been found to be optimum for creating plasmas with pulse energies below 3 J. This work has been described in chapters 4, 6 and 7.

Considerable effort has been devoted to developing and understanding the two extreme ultraviolet spectrometers used in our studies. Dynamic ranges and spectral resolution of the instruments have been determined, and a gain measurement technique has been developed to accommodate the limited dynamic ranges of the spectrometers. Additionally, a basic amplified spontaneous emission model has been developed to simulate results from gain measurements. This work is described in chapters 3, 4 and 5. From this work, we estimate that the minimum detectable gain-length product for our system is about 1.6.

With the pump-laser configured for long pulses and the EUV detectors well understood, a series of gain studies have been carried out for recombination and collisional lasants. Results from these measurements are presented in chapter 7. For recombination lasants, H-like, He-like, Li-like and Na-like lasants have been investigated. For collisional lasants, Ne-like and Ni-like lasants have been studied. H-like B, Li-like F, Ne-like Ca and Ni-like Nb have received the largest amount of research time. Results from these measurements have shown no convincing evidence of EUV amplification. Data from gain studies and other experiments reported in this thesis are collected in fifteen notebooks, which remain with the table-top system.

8.2 Possible Reasons for Absence of Gain

The author proposes four arguments to explain the absence of gain in cur experiments. One explanation pertains to the time-integrated detection used in the experiments. The other explanations relate to the physics of the plasma. These arguments are presented briefly to aid in providing direction for future research.

An argument can be made that the time-integrating imaging mode of the S/ICGS obscures direct observation of gain. If the peak gain were small and the gain lifetime short compared to the spontaneous emission lifetime of the lasing transition, then gain may go undetected. Our initial gain measurements [1,2,77] were made with the S/ICGS used in streaked mode, which provided temporal resolution. From these measurements, the lifetime of candidate lasing transitions was observed to be about 1 ns. However, for initial reports of gain, the temporally resolved spectra were averaged over 800 ps to estimate gain coefficients. Consequently, the temporal resolution was only necessary to discriminate second or third pulse emission from pre-pulse emission in collisionally pumped experiments. In previous experiments and recent experiments it has been found that emission from the pre-pulse is at least a factor of two lower than second or third pulse emission. Due to the limited dynamic range of the S/ICGS used for gain measurements reported in this thesis, most of the emission recorded on film is due to the second or third pump-laser pulses, for which gain is expected. Additionally, if the time integrated amplified signal is weaker than the time integrated spontaneous emission, than coherent EUV applications would be impractical. Time-integrated observations of low, ~ 4, and high, ~ 11, gain-length products have been reported at other laboratories [14,58,76].

One physical explanation for the absence of gain may be that the electron temperature

in the plasma is significantly lower than the value of 200 eV, which has been inferred from the ionization studies. This would explain the absence of amplification for collisional lasing schemes. Recall that the arguments of chapter 3 show an exponential temperature dependence of the upper laser level population on electron temperature. A low electron temperature cannot explain the absence of gain for the recombination lasants, which favor rapid cooling. Ionization studies indicate that the requisite recombination ions are produced and fully ionized. Although the electron temperature may be too low for collisionally pumped lasants, results from the ionization studies suggest that recombination pumped lasants should exhibit gain.

Another physical explanation may be that the ion density is low. Since the gain coefficient is directly proportional to ion density, this explanation would explain the absence of gain in both recombination and collisional schemes. Results from the ionization studies indicate that the requisite ions are created for both lasing schemes. Since our plasmas are created from slab targets, we expect that the correct ion density exists somewhere above the target surface. Therefore, the correct electron temperature is required to exist at the location of the correct ion density for gain to be observed.

Finally, the absence of a large gain-length product may be explained by a steep density gradient in the plasma. As discussed in chapter 3, a large density gradient causes several problems. Problems associated with EUV beam refraction become significant with a density gradient above 10^{22} cm^{-4}. Results from line opacity measurements reported in section 6.4 of chapter 6 suggest that the density gradient near the gain region approaches this value for a BN plasma. The gradient would be larger for higher Z elements. These opacity measurements are only preliminary and need to be verified. Further, the opacity measurements are easily corrupted by off-axis emission or optically thin emission from adjacent regions of the plasma as noted in chapter 3.

Another problem associated with a large density gradient is a reduction in the volume of the gain region. As the plasma density profile steepens, the width of the region of high gain decreases. If the gain region is too narrow compared to the region observed in the measurements, then small gain values may go undetected. Optically thin emission from adjacent plasma regions may equal or exceed emission from the gain region.

A further problem is related to a steep density gradient and thin gain region. Under these conditions, the gain-length becomes more strongly dependent on plasma uniformity, which in

turn depends upon the uniformity of the pump laser beam. A non-uniform pumping intensity along the plasma column is expected to create non-uniformity in electron density, and therefore gain conditions. For a narrow gain region, EUV emission may pass through regions of gain and regions of absorption as it propagates along the plasma column. This effect could cancel any amplification.

8.3 Suggestions for Future Research

The author has three general suggestions for future research with the MIT table-top EUV system. The first suggestion is to determine which of the physical explanations proposed in the previous section are responsible for the absence of gain in our experiments. The second suggestion is to carry out two gain experiments with the present table-top EUV system. Minor modifications to the system would be required for these experiments. The last suggestion is to add a second pump-laser or slab amplifier to the existing system.

The EUV laser research effort at MIT may benefit from a detailed study of laser-produced plasma conditions. Results from such a study may explain why moderate gain-length products have not been observed in our experiments, when values larger than 4 are expected. Spectral line ratio measurements, and careful line opacity measurements may reveal information about the plasma temperature and density gradient. To carry out these measurements, frequency responses of the spectrometers must be determined, and it may be necessary to use the S/ICGS in streaked mode to obtain temporally resolved information. The method of constant-dose will be useful for line ratio analysis in these experiments. If the electron temperature and plasma density profile can be determined accurately, measurements should be made for plasmas produced with short and long pulses, 60 ps and 210 ps. These results may explain the observations in this work that longer pulses are preferred for exciting plasmas. Results from such a study may be interesting to the table-top EUV laser community.

There are two gain experiments that may be carried out with the current table-top EUV system, after making minor system modifications. In one experiment H-like C should be used, and for the other experiment the author proposes that Ne-like Ca be used as the lasant. Both lasants have been shown to lase at other facilities [14,58].

The first experiment would be an effort to reproduce results reported at another laboratory. A gain-length product of about 2 and 4 have been reported for a H-like C recombination laser,

which is pumped with 2 ns pulses from an infrared laser [14,72]. Only four to six joules of energy are used in a single pulse. For one experiment, the peak pumping intensity is 6.7×10^{11} W cm^{-2} and the peak pumping fluence is 1333 J cm^{-2} for a 6 mm long plasma. With the MIT system configured for 210 ps pulses, as reported in this thesis, pumping intensities of 6.2×10^{12} W cm^{-2} and fluences of 1250 J cm^{-2} are achieved for 5 mm long plasmas.

We expect, with a pumping intensity nearly ten times higher in our system, that a larger gain-length product would be observed with our system. Many H-like C experiments, which have been carried out with our system, have failed to show any evidence of gain on the H-like 3d-2p lasing transition. The different results may be due to the pump-laser pulse length difference between the two systems.

If a long pulse is required to demonstrate gain, the the MIT system should be redesigned to produce long pulses. This might be achieved by inserting a multi-plate birefringent filter into the oscillator cavity and reducing the acousto-optic mode-locker RF power. With long pulses, the energy in the slab may be increased further. The pulse energy will then be limited by the energy damage limit of the slab amplifier. It may be necessary to expand the beam further to avoid damaging optics after the slab amplifier.

Another experiment, which may require fewer modifications to the system, is to further investigate a transverse-and-longitudinally pumped Ne-like Ca plasma. Preliminary T & L pumping experiments, as described in section **6.3.3** have been carried out for a bare CaF_2 target with 5 mm long plasmas. Because of the vacuum chamber design, and to avoid damaging the S/ICGS grating, the longitudinal beam was inclined at an angle of 2.1° from the plane of the target. Also, the spectrometer input slits were removed to avoid optical damage, which severely degraded spectral resolution.

In recent experiments with longitudinally pumped plasmas, it has been found that pump-laser alignment to the EUV laser axis is critically important [109]. If not properly aligned, the longitudinal beam ablates too much mass from the target surface. It is conjectured that the excess mass cannot be sufficiently heated.

If a T & L experiment is to be repeated with the MIT system, the chamber should be configured so that the longitudinal beam can be aligned to the EUV laser axis. For this experiment, it will be difficult to avoid damaging the spectrometer grating. Additionally, experiments should be performed using a calcium V-blade, as described in section **6.4.2** of chapter 6, to create a

plasma conduit. The experiment may also benefit from an improved spectrometer, which has at least twice the resolution of the S/ICGS. This would enable positive identification of the Ne-like Ca 3p-3s lasing transition at 38.33 nm.

A final proposal for continued research will require additional project funding. It is proposed that a second ultrashort pulse laser be used to excite a preformed plasma as has been demonstrated in several recent experiments [69,70,71]. A passively mode-locked Ti:Al_2O_3 laser, which has been used in two of these demonstrations, is recommended as a second laser. The Ti:Al_2O_3 laser can readily produce subpicosecond pulses and can be tuned to a wavelength within the amplification bandwidth of our system. This proposal requires substantial funding and considerable experimental effort.

Bibliography

[1] S. Basu, et. al., "Amplification in Ni-like Nb at 20.4 nm pumped be a table-top laser", *Appl. Phys. B*, **57**, (1993) p. 303.

[2] J. Goodberlet, et. al., "Observation of gain in a recombining H-like boron plasma", *J. Opt. Soc. Am. B*, **12**, (1995) p. 980.

[3] B. J. MacGowan, et. al., "Short wavelength x-ray laser research at the Lawrence Livermore National Laboratories", *Phys. Fluids B*, **4**, (1992) p. 2326.

[4] J. J. Rocca, et. al., "Demonstration of a discharge pumped table-top soft-x-ray laser", *Phys. Rev. Lett.*, **73**, (1994) p. 2192.

[5] R. C. Elton, *X-Ray Lasers*, Academic Press, Inc., New York, (1990) p. 5.

[6] P. L. Hagelstein, "Physics of short wavelength laser design", Report No. UCRL-53100, Lawrence Livermore National Laboratory, Livermore, California, 1981, and P. L. Hagelstein *Physics of Short Wavelength Design*, MIT PhD Thesis, 1981.

[7] C. Chenais-Popovics, et. al., "Laser amplification at 18.2 nm in recombining plasma from a laser-irradiate carbon fiber", *Phys. Rev. Lett.*, **59**, (1987) p. 2161.

[8] D. Matthews, et. al., "Demonstration of a soft x-ray amplifier", *Phys. Rev. Lett.*, **54**, (1985) p. 110.

[9] A. S. Wan, et. al., "X-ray laser interferometry for probing high-density plasmas", in *Soft X-Ray Lasers and Applications*, J. J. Rocca, P. L. Hagelstein, Editors, Proc. SPIE 2520, (1995) p. 268.

[10] K. Siegbahn, *From X-Ray to Electron Spectroscopy*, Department of Physics, University of Uppsala, Sweden, Pub. 30 (1988)

[11] H. Smith, "Submicron and nanometer-structures technology" Course 6.781 Lecture Notes, MIT, Cambridge, Massachusetts (1993) p. 16-3.

[12] P. Maine, et. al., "Generation of ultrahigh peak power pulses by chirped pulse amplification", *IEEE J. of Quant. Elec.*, **24**, (1988) p. 398.

[13] V. Bhagavatula and B. Yaakobi, "Direct observation of population inversion between Al^{11+} levels in a laser-produced plasma", *Opt. Commun.*, **24**, (1978) p. 331.

[14] C. O. Park, et. al., "Recent results on development of a table-top soft x-ray laser", *Appl. Phys. B*, **58**, (1994) p. 19.

[15] T. Hara, et. al., "Compact soft x-ray laser pumped by a pulse-train laser", in *Soft X-Ray Lasers and Applications*, J. J. Rocca, P. L. Hagelstein, Editors, Proc. SPIE 2520, (1995) p. 217.

[16] L. I. Gudzenko and L. A. Shelepin, "Radiation enhancement in a recombining plasma", *Sov. Phys.*, **10** , (1965), p. 147.

[17] A. N. Zherikhin, et. al., "Gain in the far vacuum ultraviolet region due to transitions in multiply charge ions", *Sov. J. Quant. Electron.*, **6**, (1976), p. 82.

[18] D. Jacoby, et. al., "Observation of gain in a possible extreme ultraviolet lasing system", *Opt. Commun.*, **37**, (1981), p. 193.

[19] C. E. Max, *Physics of Laser Fusion, Vol. 1: Theory of the Coronal Plasma in Laser Fusion Targets*, National Technical Information Service, Springfield, VA (1982), p. 7.

[20] D. Matthews, et. al., "X-ray laser research at the Lawrence Livermore National Laboratory Nova laser facility ", *J. Opt. Soc. Am. B* , **4**, (1987), p. 575.

[21] S. Bashkin and J. O. Stoner, Jr., *Atomic Energy-Level & Grotrian Diagrams 2*, North-Holland Pub. Co., New York, NY (1978).

[22] G. Pert, "Model calculations of XUV gain in rapidly expanding cylindrical plasma ", *J. Phys. B: Atom. Molec. Phys.*, **9**, (1976), p. 3301.

[23] J. Zhang and M. H. Key, "Hydrogen-like recombination x-ray lasers using ps pulse drivers ", *Appl. Phys. B*, **58**, (1994), p. 13.

[24] S. Suckewer and H. Fishman, "Conditions for soft x-ray lasing action in a confined plasma column", *J. Appl. Phys.*, **51**, (1980), p. 1922.

[25] S. Suckewer, et. al., "Population inversion and gain measurements for soft x-ray laser development in a magnetically confined plasma column", *IEEE J. Quant. Elec.*, **19**, (1983), p. 1855.

[26] S. Suckewer, et. al., "Amplification of stimulated soft x-ray emission in a confined plasma column", *Phys. Rev. Lett.*, **55**, (1985), p. 1753.

[27] D. Kim, et. al., "Gain measurements at 18.22 nm in C VI generated by a Nd:glass laser", *Opt. Lett.* , **14**, (1989), p. 665.

[28] R. L. Kelly, *Atomic Emission Lines Below 2000 Angstroms: Hydrogen Through Argon*, U. S. Government Printing Office, Washington, D. C., (1968).

[29] J. Kirz, et. al., *X-Ray Data Booklet*, D. Vaughan, Ed., Lawrence Berkeley Laboratory, Berkeley, CA (1986) p. 2-26.

[30] B. J. MacGowan, et. al., "Soft x-ray amplification at 50.3 Å in nickellike ytterbium", *J. Opt. Soc. Am. B*, **5**, (1988), p. 1858.

[31] W. L. Wiese, M. W. Smith and B. M. Glennon, *Atomic Transition Probabilities, Volume I: Hydrogen Through Neon*, U. S. Government Printing Office, Washington, D. C. (1966) p. 6.

[32] A. K. Bhatia, U. Feldman and J. F. Seely, "Atomic Data and Spectral Line Intensities for the Neon Isoelectronic Sequence (Si V through Kr XXVII)", *Atom. Data and Nuc. Data Tab.*, **32**, (1985) p. 435.

[33] F. V. Bunkin, et. al., "Prospects for light amplification in the far ultraviolet", *Sov. J. Quant. Elec.*, **11**, (1981), p. 981.

[34] P. Jaegle, et. al., "Soft x-ray amplification by lithiumlike ions in recombining hot plasmas", *J. Opt. Soc. Am. B*, **4**, (1987), p. 563.

[35] C. J. Keane, et. al., "Soft x-ray laser source development and applications experiments at Lawrence Livermore National Laboratory", *J. Phys. B: At. Mol. Opt. Phys.*, **22**, (1989), p. 3343.

[36] J. Steingruber and E. E. Fill, "Soft x-ray gain in Na-like copper and nickel ions",in *X-Ray Lasers 1990*, G. J. Tallents, Ed., IOP Publishing Ltd., Bristol, England (1990), p. 123.

[37] M. Grande, et. al., "Measurement and detailed analysis of single pass gain at 81 Å in a recombining laser produced fluorine plasma", *Opt. Commun.*, **74**, (1990), p. 309.

[38] Z-Z Xu, et. al., "Study of recombination x-ray lasers and related plasma physics at Shanghai", in *X-Ray Lasers 1990*, G. J. Tallents, Ed., IOP Publishing Ltd., Bristol, England (1990), p. 151.

[39] J. Steingruber, et. al., "Recombination gain in Na-like copper and germanium", in *X-Ray Lasers 1992*, E. E. Fill, Ed., IOP Publishing Ltd., Bristol, England (1992), p. 151.

[40] Z-Z Xu, et. al., "Studies of recombination x-ray laser gain and gain medium uniformity", *Appl. Phys. B*, **57**, (1993), p. 319.

[41] H. Daido, et. al., "Simultaneous amplification of sodium and fluorine Balmer-α lines", *J. Opt. Soc. Am. B*, **11**, (1994), p. 280.

[42] J. Zhang, et. al., "Demonstration of high gain in a recombination XUV laser at 18.2 nm driven by a 20 J, @ ps glass laser", *Phys. Rev. Lett.*, **74**, (1995) p. 1335.

[43] T. N. Lee, et. al., "Soft x-ray lasing in neonlike germanium and copper plasmas", *Phys. Rev. Lett.*, **59**, (1987), p. 1185.

[44] B. J. MacGowan, et. al., "Demonstration of soft x-ray amplification in nickel-like ions", *Phys. Rev. Lett.*, **59**, (1987), p. 2157.

[45] G. D. Enright, et. al., "X-ray gain measurements in a collisionally excited Ge plasma", in *X-Ray Lasers 1990*, G. J. Tallents, Ed., IOP Publishing Ltd., Bristol, England (1990), p. 343.

[46] D. Desenne, et. al., "X-ray amplification in Ne-like silver: gain determination and time-resolved beam divergence measurement", in *X-Ray Lasers 1990*, G. J. Tallents, Ed., IOP Publishing Ltd., Bristol, England (1990), p. 351.

[47] B. J. MacGowan, et. al., "Demonstration of x-ray amplifiers near the carbon K-edge", *Phys. Rev. Lett.*, **65**, (1990), p. 420.

[48] Y. Kato, et. al., "Coherence and double-pass amplification in Ge soft x-ray laser", in *X-Ray Lasers 1992*, E. E. Fill, Ed., IOP Publishing Ltd., Bristol, England (1992), p. 9.

[49] C. L. S. Lewis, et. al., "Collision pumped soft x-ray lasers: progress at RAL", in *X-Ray Lasers 1992*, E. E. Fill, Ed., IOP Publishing Ltd., Bristol, England (1992), p. 23.

[50] J. Nilsen, et. al., "Demonstration of a neon-like rubidium x-ray laser", in *X-Ray Lasers 1992*, E. E. Fill, Ed., IOP Publishing Ltd., Bristol, England (1992), p. 53.

[51] L. B. Da Silva, et. al., "Power measurements of a saturated yttrium x-ray laser", *Opt. Lett.*, **18**, (1993), p. 1174.

[52] B. Rus, et. al., "Observation of intense soft x-ray lasing at the J=0 to J=1 transition in neonlike zinc", *J. Opt. Soc. Am. B*, **11**, (1994), p. 564.

[53] J. Nilsen and J. C. Moreno, "Nearly monochromatic lasing at 182 Å in neonlike selenium", *Phys. Rev. Lett.*, **74**, (1995), p. 3376.

[54] Dr. Y. Li, private communication.

[55] G. Jamelot, et. al., "The 212 Å neon-like zinc laser of LULI", in *Soft X-Ray Lasers and Applications*, J. J. Rocca, P. L. Hagelstein, Editors, Proc. SPIE 2520, (1995) p. 2.

[56] R. Kodama, et. al., "Experimental progress in collisional x-ray laser development at ILE Osaka University", in *Soft X-Ray Lasers and Applications*, J. J. Rocca, P. L. Hagelstein, Editors, Proc. SPIE 2520, (1995) p. 25.

[57] H. Fiedorowicz, et. al., "X-ray laser experiments using laser-irradiated gas puff targets at the ASTERIX IV facility", in *Soft X-Ray Lasers and Applications*, J. J. Rocca, P. L. Hagelstein, Editors, Proc. SPIE 2520, (1995) p. 55.

[58] E. E. Fill, et. al. "Investigation of lasing on the J=1-0 line of neon-like ions using the prepulse technique", in *Soft X-Ray Lasers and Applications*, J. J. Rocca, P. L. Hagelstein, Editors, Proc. SPIE 2520, (1995) p. 134.

[59] G. J. Pert, et. al. "Theoretical studies of recombination laser design", in *X-Ray Lasers 1992*, E. E. Fill, Ed., IOP Publishing Ltd., Bristol, England (1992), p. 105.

[60] P. L. Hagelstein, "Development of the MIT tabletop soft x-ray laser", in *Ultrashort-Wavelength Lasers*, S. Suckewer, Ed., Proc. SPIE 1551, (1992) p. 254.

[61] R. L. Kelly, *Atomic and Ionic Spectrum Lines Below 2000 Angstroms: Hydrogen through Chromium Part I (H-Cr)*, AIP, Inc., New York, New York, 1987.

[62] H. C. Kapteyn, et. al. "Observation of a short-wavelength laser pumped by Auger decay", *Phys. Rev. Lett.*, **57**, (1986) p. 2939.

[63] M. H. Sher, et. al. "Saturation of the Xe III 109 nm laser using traveling-wave laser-produced-plasma excitation", *Opt. Lett.*, **12**, (1987) p. 891.

[64] J. J. Rocca, et. al. "Proposal for soft-x-ray and XUV lasers in capillary discharges", *Opt. Lett.*, **13**, (1988) p. 565.

[65] J. J. Rocca, et. al. "Towards saturation of a discharge pumped soft-x-ray amplifier", in *Soft X-Ray Lasers and Applications*, J. J. Rocca, P. L. Hagelstein, Editors, Proc. SPIE 2520, (1995) p. 201.

[66] J. J. Rocca, et. al., "Fast-discharge excitation of hot capillary plasmas for soft-x-ray amplifiers", *Phys. Rev. E*, **47** (1993) p. 1299.

[67] J. J. Rocca, et. al. "Experiments on soft x-ray laser development in a table-top capillary discharge", in *Ultrashort-Wavelength Lasers*, S. Suckewer, Ed., Proc. SPIE 1551, (1992) p. 275.

[68] N. H. Burnett and P. B. Corkum, "Cold-plasma production for recombination extreme-ultraviolet lasers by optical-field-induced ionization", *J. Opt. Soc. Am. B*, **6**, (1989) p. 1195.

[69] B. E. Lemoff, et. al. "Demonstration of a 10-Hz femtosecond-pulse-driven XUV laser at 41.8 nm in Xe IX", *Phys. Rev. Lett.*, **74**, (1995) p. 1574.

[70] Y. Nagata, et. al. "Soft-x-ray amplification of the Lyman-α transition by optical-field-induced ionization", *Phys. Rev. Lett.*, **71**, (1993) p. 3774.

[71] P. V. Nickles, et. al. "An efficient short pulse XUV-laser on [Ne]-like titanium", in *Soft X-Ray Lasers and Applications*, J. J. Rocca, P. L. Hagelstein, Editors, Proc. SPIE 2520, (1995) p. 373.

[72] C. H. Skinner, et. al. "Development of small-scale soft-x-ray lasers: aspects of data interpretation", *J. Opt. Soc. Am. B*, **7**, (1990) p. 2042.

[73] Y. Kato, et. al. "Explosive-mode short wavelength recombination Balmer-α laser", in *X-Ray Lasers 1990*, G. J. Tallents, Ed., IOP Publishing Ltd., Bristol, England (1990), p. 1.

[74] G. J. Tallents, et. al. "X-ray recombination laser experiments pumped with 12 ps KrF pumped Raman lasers", in *X-Ray Lasers 1992*, E. E. Fill, Ed., IOP Publishing Ltd., Bristol, England (1992), p. 101.

[75] C. Kittel, *Introduction to Solid State Physics, 5th Ed.*, John Wiley & Sons, New York, New York, (1976) p.289.

[76] S. Suckewer and L. Polansky, private communications.

[77] M. H. Muendel, *Short wavelength laser gain studies in plasmas produced by a small Nd:Glass Slab Laser*, MIT Ph. D. Thesis, (1994) p. 95.

[78] J. J. Rocca, et. al., "Efficient generation of highly ionized calcium and titanium plasma columns for collisionally excited soft-x-ray lasers in a fast capillary discharge", *Phys. Rev. E*, **48**, (1993) p. R2378.

[79] V. A. Chirkov, "Refraction in a plasma and laser resonators for vacuum ultraviolet", *Sov. J. Quant. Elec.*, **14**, (1984) p. 1497.

[80] M. Born and E. Wolf, *Principles of Optics*, 4th Ed., Pergamon Press, New York, New York, (1970) p. 122.

[81] G. J. Linford, et. al., "Very long lasers", *Appl. Opt.*, **13**, (1974) p. 379.

[82] L. Allen and G. I. Peters, "Amplified spontaneous emission III. Intensity and saturation", *J. Phys. A: Gen. Phys.*, **4**, (1971) p. 564.

[83] G. I. Peters and L. Allen, "Amplified spontaneous emission IV. Beam divergence and spatial coherence", *J. Phys. A: Gen. Phys.*, **5**, (1972) p. 547.

[84] C. Rolland and P. B. Corkum, "Compression of high-power optical pulses", *J. Opt. Soc. Am. B*, **5**, (1988) p. 641.

[85] H. A. Haus, *Waves and Fields in Optoelectronics*, Prentice-Hall, Inc., Englewood Cliffs, New Jersey (1984) p. 358.

[86] A. E. Siegman, *Lasers*, University Science Books, Mill Valley, California (1986) p. 387.

[87] W. J. Tomlinson, et. al., "Compression of optical pulses chirped by self-phase modulation in fibers", *J. Opt. Soc. Am. B*, **1**, (1984) p. 139.

[88] W. Koechner, *Solid-State Laser Engineering*, Springer-Verlag, New York, New York (1988) p.546.

[89] H. W. Kogelnik, et. al., "Astigmatically compensated cavities for CW dye lasers", *IEEE J. of Quant. Elec.*, **QE-8**, (1972) p. 373.

[90] E. B. Treacy, "Optical pulse compression with diffraction gratings", *IEEE J. of Quant. Elec.*, **QE-5**, (1969) p. 454.

[91] O. E. Martinex, "3000 times grating compressor with positive group velocity dispersion: application to fiber compensation in 1.3-1.6 μm region", *IEEE J. of Quant. Elec.*, (1987) p. 59.

[92] O. E. Martinez, "Grating and prism compression in the case of finite beam size", *J. Opt. Soc. Am. B*, **3**, (1986) p. 929.

[93] S. D. Brorson, "Geometrical limitations in grating pair pulse compression", *Appl. Opt.*, **27**, (1988) p. 23.

[94] Documentation on *Fresnel* is available from P. L. Hagelstein.

[95] Grating specification brochure. Spectragon U. S., Inc., Parsippany, N. J. (1993).

[96] It should be noted that the optical quality of the slab amplifier was observed to be decreasing during these experiments. This was due to degradation of index matching adhesive used at the top of the slab. It was discovered that the glue appeared to be melting and running down the sides of the slab. The slab was disassembled and cleaned, although much of the debris could not be removed with acetone. The quality of the output beam remained satisfactory until the last day of experiments.

[97] T. Kita, et. al., "Mechanically ruled aberration-corrected concave gratings for a flat-field grazing-incidence spectrograph", *Appl. Opt.*, **22**, (1983) p. 512.

[98] B. L. Henke, et. al., "A preliminary report on x-ray photoabsorption coefficients and atomic scattering factors for 92 elements in the 10-10000 eV region", PUB LBL-26259 UC-411, Lawrence Berkeley Laboratory, Berkeley, California (1988) p. 21.

[99] D. J. Donahue, et. al., "Beam-foil measurements of mean lives in B IV and B V below 450 Å", *J. Opt. Soc. Am.*, **68**, (1978) p. 998.

[100] "Detector Assemblies", Data sheet No. 7000, Galileo Electro-optics Corp., Sturbridge, Massachusetts.

[101] J. Goodberlet, et. al., "Moderately ionized, low pump-energy extreme ultraviolet amplifiers", in *Soft X-Ray Lasers and Applications*, J. J. Rocca, P. L. Hagelstein, Eds., Proc. SPIE 2520, (1995) p. 191.

[102] The author gratefully acknowledges the help of his brother, M. Goodberlet, in developing this "method of slopes" analysis.

[103] M. L. Boas, *Mathematical Methods in the Physical Sciences*, John Wiley & Sons, Inc., New York, New York, (1983) p. 734.

[104] G. J. Tallents, et. al., "Improving the efficiency of x-ray lasers", in *Soft X-Ray Lasers and Applications*, J. J. Rocca, P. L. Hagelstein, Editors, Proc. SPIE 2520, (1995) p. 34.

[105] P. G. Burkhalter, "L-series satellite spectra in Ti XII and Fe XVI", *J. Opt. Soc. Am.*, **69**, (1979) p. 1133.

[106] C. Jupen and U. Litzen, "The $2p^5 3s$, 3p and 3d configurations in neon-like Ti XIII and Fe XVII", *Phys. Scr.*, **30**, (1984) p. 112.

[107] E. Trabert and C. Jupen, "Identification of $2s^2 2p^5 3p\ ^1S_0$ decays in the spectra of neon-like ions", *Phys. Scr.*, **36**, (1987) p. 586.

[108] S. Bashkin, et. al., "Beam-foil study of titanium in the EUV using foils of different materials", *Phys. Scr.*, **28**, (1983) p. 193.

[109] A. Morozov, L. Polonsky and S. Suckewer, "Towards compact soft x-ray lasers", in *Soft X-Ray Lasers and Applications*, J. J. Rocca, P. L. Hagelstein, Editors, Proc. SPIE 2520, (1995) p. 180.